# BAND STRUCTURE CALCULATION OF THE TWO-DIMENSIONAL ANGULAR CORRELATION OF POSITRON ANNIHILATION RADIATION IN V AND $VD_{0.72}$

By

ASHOK KUMAR SINGH

DEPARTMENT OF PHYSICS

INDIAN INSTITUTE OF TECHNOLOGY KANPUR

MAY, 1981

BAND STRUCTURE CALCULATION OF THE TWO-DIMENSIONAL ANGULAR CORRELATION OF POSITRON ANNIHILATION RADIATION IN V AND VD$_{0.72}$

A Thesis Submitted
in Partial Fulfilment of the Requirements
for the Degree of

DOCTOR OF PHILOSOPHY

By
ASHOK KUMAR SINGH

to the

DEPARTMENT OF PHYSICS

INDIAN INSTITUTE OF TECHNOLOGY KANPUR

MAY. 1981

Dedicated

to

VIDYARTHI BABA

and

TRIDANDI SWAMI

PHY-1981-D-SIN-BAN
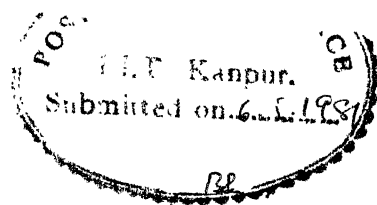
CERTIFICATE

This is to certify that the work presented in this thesis entitled 'Band Structure Calculation of the Two-dimensional Angular Correlation of Positron Annihilation Radiation in V and $VD_{0.72}$' by Ashok Kumar Singh has been done under my supervision and it has not been submitted elsewhere for a degree or diploma.

R. M. Singru
Department of Physics
Indian Institute of Technology
Kanpur, India

May 1981

ii

ACKNOWLEDGEMENTS

CONTENTS

iv

LIST OF TABLES

vi

SYNOPSIS

BAND STRUCTURE CALCULATION OF THE TWO-DIMENSIONAL
ANGULAR CORRELATION OF POSITRON ANNIHILATION
RADIATION IN V AND VD$_{0.72}$

By

ASHOK KUMAR SINGH
Department of Physics
Indian Institute of Technology,
Kanpur 208016, India.

April 1981

In recent years the study of positron annihilation in
solids has become an important tool to study different physical
properties of the solids. In particular the measurement of
the angular correlation of positron annihilation radiation
(ACPAR) has provided us with important data about the Fermi
surface (FS) and the electron momentum distributions in metals
and alloys. Recently different machines have been developed
to measure two-dimensional (2D) ACPAR curves and such measure-
ments in metals like Al, Cu and alloys of Cu like Cu-Zn, Cu-Ni
have shown that 2D-ACPAR technique is a powerful method to
study the FS parameters. The work on Cu, in particular, has
shown that it is essential to perform a band structure calcula-
tion of the two-photon momentum distributions in a transition
metal for computing the 2D-ACPAR curves. By comparing the
theoretical and experimental 2D-ACPAR curves one can obtain
considerable details about the band structure and FS of
transition metals. In the case of a 3$\underline{d}$ transition metal like

vanadium (V) which has a Fermi level lying among the d-bands, the band structure and the FS are sensitive to parameters like crystal potential, exchange effects, self-consistency, electron configuration etc. used in the band structure calculation. One-dimensional ACPAR measurements in the single crystal of V have already shown that the band structure and FS characteristics of V give rise to fine-structure in these curves. It is, therefore, expected that a 2D-ACPAR measurement in V would provide us with a greater wealth of data which can be used to test band structure calculation. Keeping this aim in mind we have calculated the band structure, FS, two-photon momentum distribution and the 2D-ACPAR curves for four sets of single crystal directions in V. The calculated 2D-ACPAR curves show fine structure which is analysed in terms of the band structure and Fermi surface. The results are extended to predict the 2D-ACPAR curves in vanadium deuteride $(VD_{0.72})$ within the framework of rigid band protonic model.

In Chapter 1 a general introduction to the subject of positron annihilation in metals is presented. After describing the general characteristics of the phenomenon of positron annihilation the experimental techniques used to study positron annihilation in metals are described. Since the present work deals with the study by 2D-ACPAR curves, various experimental arrangements used to measure the 2D-ACPAR curves are described in some detail. An outline of the theoretical calculation of positron annihilation in metals is given and the methods used

for comparing theory and experiment are discussed. At the end of Chapter 1 we have briefly discussed the motivation behind the present work.

A review of the theoretical and experimental studies of the band structure of V is given in Chapter 2. The experimental study of the FS and momentum distribution in V made by different workers using the techniques of Fermiology, Compton scattering and positron annihilation is also reviewed.

The method for the band structure calculation used in the present work was Hubbard's fast approximation scheme for transition metals. In Chapter 3 we have outlined various steps involved in this method and have discussed how Hubbard's fast approximation scheme has been modified by Mijnarends for the calculation of the electron wavefunctions and momentum distributions. Different methods used for the calculation of the positron wavefunction in metals are described and the corrections to the momentum distribution due to the many-body effects are briefly discussed. The Chapter concludes with an outline of the calculation of two-photon momentum distribution in metals.

In Chapter 4 we have presented the results of our calculations for the band structure, FS, two-photon momentum distribution and 2D-ACPAR curves in V. Numerical details of the parameters used in our calculation are given. The results are presented in terms of various tables and figures and are compared with the results of other calculations wherever possible. The calculated two-photon momentum distribution and

the 2D-ACPAR curves are analysed in terms of the band structure to show how different sheets of the FS of V can be studied with the 2D-ACPAR techniques. Although we have calculated the 2D-ACPAR curves, $N(p_y, p_z)$, for the four crystal directions A : $p_z = $ [001], $p_x = $ [100], B : $p_z = $ [001], $p_x = $ [110], C : $p_z = [\bar{1}\bar{1}2]$, $p_x = $ [111], D : $p_z = [\bar{1}10]$, $p_x = $ [110] all in the $p_y = $ 0 plane, we have presented pictures of the FS topology in some of the $p_y \neq $ 0 planes parallel to the (100) and (110) planes to point out the importance of the 2D-ACPAR curves for $p_y \neq $ 0. Our band structure (2D-ACPAR) results are compared with those calculated by a simpler modified Wigner-Seitz model to illustrate the point that band structure calculations alone can explain the fine structure in the 2D-ACPAR curves in a transition metal like V.

Recently the electronic properties of metal-hydrogen systems have invoked considerable interest. In particular the hydrides and deuterides of the group V B metals V, Nb and Ta have been studied extensively, both theoretically and experimentally. In Chapter 5 we have extended the results of our calculations for pure V (Chapter 4) to vanadium deuteride ($VD_{0.72}$) using the rigid band protonic model. The results for $VD_{0.72}$ are discussed in terms of the changes brought in the band structure and FS of V by the introduction of deuterium. These results show how the 2D-ACPAR method can be very useful to study the band structure and FS of VD_x.

The results obtained in the present work provide an understanding to the band structure effects in a 2D-ACPAR curves in V. In view of the similarity in the band structure and FS of the isoelectronic metals V, Nb and Ta, the present results can be extended to understand 2D-ACPAR data in Nb and Ta. It is hoped that these results have emphasized the usefulness of the emerging 2D-ACPAR method for the study of transition metals and have provided guidance for designing (i.e. which $\{p_x, p_y, p_z\}$ directions to choose) a 2D-ACPAR experiment with V and VD_x. At present there is no 2D-ACPAR data reported for V and VD_x. The present results can provide a future basis for the comparison between experiment and theory. This work has also provided an opportunity to the author to learn about the interpretation of the 2D-ACPAR data.

Chapter 1

INTRODUCTION

1.1 Introduction

The determination of electron wavefunction is essential in understanding the electronic properties of atoms, molecules and solids. In addition to the other ground state properties of solids, the determination of the charge, spin and momentum distribution of electrons has recently become an interesting subject for experimental and theoretical research [1,2]. In particular the band structure and Fermi surface (FS) of metals is being increasingly investigated through the determination of the electron momentum distribution (EMD) of the metal. Three microprobes photons (Compton scattering) [3], positrons (positron annihilation studies) [4,5] and electrons (electron Compton scattering, (e,2e) scattering) [3,6] can be used to determine the EMD in metals [1,2].

The EMD, $\rho(\vec{p})$, is defined as

$$\rho(\vec{p}) = |\chi(\vec{p})|^2 \qquad (1.1)$$

where $\chi(\vec{p})$ is the electron wavefunction in the momentum space and it can be obtained from the wavefunction, $\psi(\vec{r})$, in the position space through the Dirac transformation

$$\chi(\vec{p}) = \int \psi(\vec{r}) \exp(-i\vec{p}.\vec{r}) \, d\vec{r} \qquad (1.2)$$

For a meaningful comparison between theory and experiment it is necessary to have a band structure calculation of the EMD in metals. Such a comparison can allow us to examine the effects of band structure on the EMD and to test the validity of the results of a particular band structure calculation. Among the different experimental techniques i.e. Compton scattering, positron annihilation and electron scattering, the measurements employing two-dimensional (2D) angular correlation of positron annihilation radiation (ACPAR) are very useful in studying the FS of metals. The present thesis describes the results of our calculations of the momentum distributions in V as studied by 2D-ACPAR methods. The band structure and FS topology for V is one of the most interesting among the 3$\underline{d}$ transition metals. The results discussed in the present thesis provide suggestions for designing a 2D-ACPAR experiment to study the band structure and FS of V. These results are then extended to examine the VD_x system which has assumed considerable importance in the last few years.

The plan of the present Chapter is as follows. The characteristics of positron annihilation process are discussed in Sec. 1.2 while the experimental techniques involved in the study of positron annihilation are described in Sec. 1.3. The theory for the angular correlation of positron annihilation radiation is outlined in Sec. 1.4. In Sec. 1.5 the methods used for comparing theory with experiment are described and in Sec. 1.6 the motivation of the present work is discussed.

1.2 Characteristics of Positron Annihilation

In recent years diverse problems in the physics of condensed matter are being studied by using positron annihilation techniques [4,5]. In these experiments low energy (0-700 keV) positrons from laboratory sources like radioactive ^{22}Na, ^{64}Cu or ^{58}Co are allowed to annihilate in the sample under study and observations are made on the timing or energy or direction characteristics of the annihilation gamma rays. These low energy positrons, upon entering the material medium, slow down to thermal energies losing their energy through ionization and excitation collisions. The time taken for this thermalization of positrons is very short ($\sim 10^{-12}$ s or so) compared to the lifetime for their annihilation ($\tau > 10^{-10}$ s). These features are shown schematically in Fig. 1.1.

A thermalized positron undergoes an annihilation with an electron by emitting a number of photons which will carry an energy equal to the combined rest mass energy $2m_0c^2$ ($\simeq 1.02$ MeV). The sum of the kinetic energies of electron (few eV) and positron (~ 0.02 eV) is very low compared to the above energy (1.02 MeV). The probability for the various modes of the annihilation of the thermalized positron-electron pair is determined by various selection rules, conservation laws and other considerations using the invariance properties of quantum electrodynamics [7]. Figure 1.2 shows the Feynmann diagrams for the most probable annihilation process
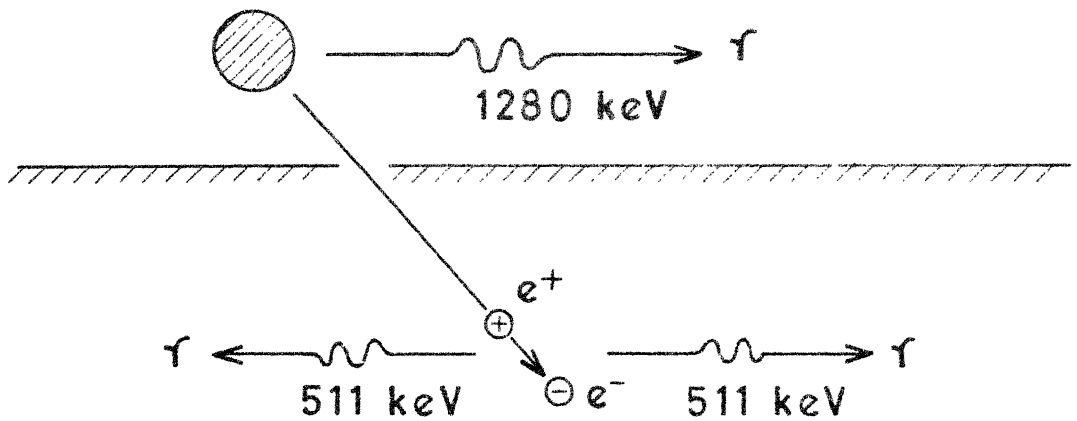
Fig. 1.1: Kinematic description of the annihilation of positrons from Na. The 1280-keV gamma ray is simultaneous with the emission of positron while the 511-keV gamma rays signal its annihilation.
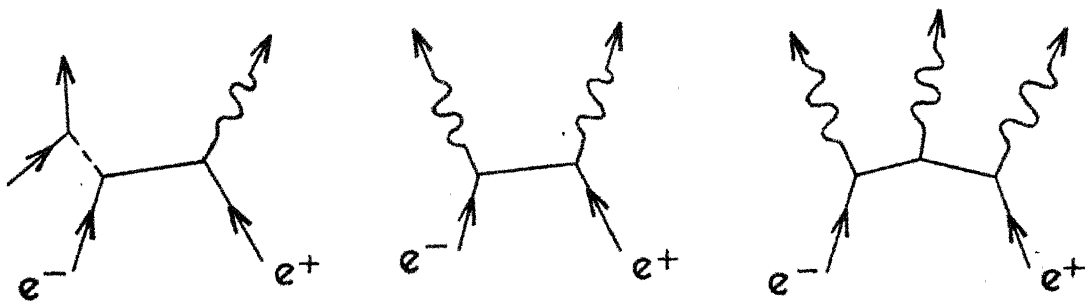
Fig. 1.2: Feynmann diagrams describing one, two and three-photon annihilation modes.

i.e. one, two and three photon emission. The ratio of the cross section for the one, two or three photon annihilation process is given by [4] $\sigma_{(3\gamma)}/\sigma_{(2\gamma)} \simeq \alpha$ and $\sigma_{(1\gamma)}/\sigma_{(2\gamma)} \simeq \alpha^4$ where $\alpha = 1/137$, the fine structure constant. Thus the probability of the two-photon annihilation is much greater than that for one and three photons.

One can write the expression for the cross section for the two-photon annihilation at low velocities, v, of the positron as [4]

$$\sigma_{(2\gamma)} = \pi r_0^2 c/v \qquad (1.3)$$

where $r_0 = e^2/m_0 c^2 =$ classical electron radius. The equation for the probability ($\Gamma_{2\gamma}$) of two-photon annihilation becomes

$$\Gamma_{2\gamma} = \sigma_{(2\gamma)} v n_e = \pi r_0^2 c n_e \qquad (1.4a)$$

where n_e is the electron density at the positron site. The positron lifetime τ ($\tau = 1/\Gamma_{2\gamma}$) being independent of positron velocity can provide the information about the electron density (n_e) at the site of annihilation in the sample to be studied.

Equation (1.3) for the cross section $\sigma_{(2\gamma)}$ must be modified in such a way that it includes the Coulomb interaction between the annihilating positron-electron pair because the above expression is the approximate form of the relativistic expression obtained by Dirac [8]. The actual electron density seen by a positron is not only at positron site but is

also spread in the region in which Coulomb attraction is effective. Taking these considerations and the velocity-dependent electron density into account one can write the two-photon annihilation probability which depends on the positron velocity as given by [9]

$$r_{2\gamma}(v) = \pi r_0^2 \left(\frac{m}{\pi\hbar}\right)^2 \frac{2\pi\alpha/\beta}{1 - \exp(-2\pi\alpha/\beta)} \qquad (1.4b)$$

where $\beta = v/c$.

The above expression for the probability for the two-photon annihilation is no longer valid in real metals because the following two corrections will have to be made: (i) the screening of the charge of positron in the many-electron system and (ii) the Pauli exclusion principle. A more realistic treatment which includes these effects is given by Kahana [10] and it will be referred to later on. Since the scope of the present work is limited to the two-photon annihilation in metals, we shall not discuss the phenomena of positronium formation etc.

In metals the kinetic energy of the electrons is of the order of few eV while the positrons being thermalized (~ 0.02 eV) can be assumed to be at rest. The kinetic energy and the momentum of the annihilating positron-electron pair is, therefore, mainly due to the electron. In the centre-of-mass system the total energy available to the two photons is $2m_0c^2$ (~ 1.02 MeV) and they are emitted in exactly opposite ($\theta = 180°$) direction each having an energy of 511 keV. The

conservation of energy and linear momentum $(\vec{p})$ of the positron-electron pair in the laboratory system produces two measurable effects. Firstly there is a deviation from collinearity in the direction of emission of the two photons and secondly there is Doppler shift in the energy of the annihilation photons. These effects are illustrated in Fig. 1.3 which shows how the deviation θ from collinearity arises from the transverse component $p_{\perp}$ of the momentum $\vec{p}$. The angular deviation θ is related to $p_{\perp}$ by the relation

$$\theta \simeq p_{\perp}/m_0 c \qquad (1.5)$$

and for the typical values of the electron momenta in metals θ is of the order of few milliradians. The longitudinal component $p_{\parallel}$ of $\vec{p}$ causes the energy of the photon to shift from its value $E_\gamma = m_0 c^2$ (i.e. Doppler broadening). It is seen from Fig. 1.3 that this energy shift ΔE is given by

$$\Delta E = c\, p_{\parallel}/2 \qquad (1.6)$$

We thus see that the measurement of the angle θ and/or energies of the annihilation photons can provide useful information about the electron momentum distribution in metals. The details of the experimental methods using the above principles are described in the next section.

1.3 Experimental Techniques

1.3.1 Measurement of positron lifetime spectra and Doppler broadening of annihilation radiation lineshape

We have seen above that the lifetime of positron is an

$P_{||}$

P

$P_\perp$

θ

$P_2 \simeq m_0 c - \frac{1}{2} P_{||}$

$P_1 \simeq m_0 c + \frac{1}{2} P_{||}$
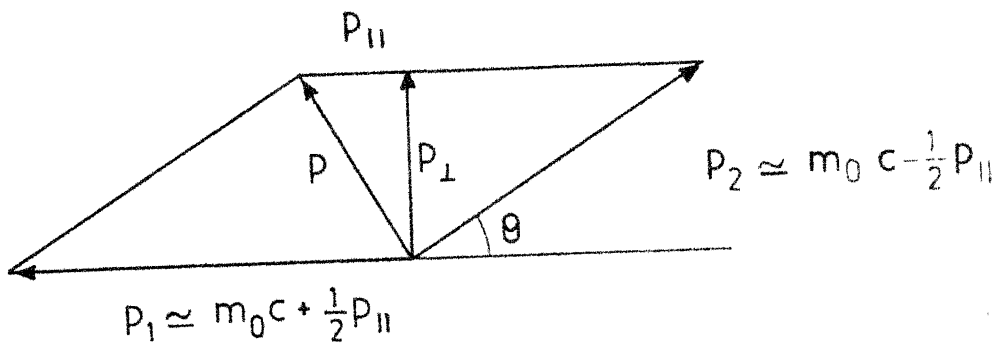
Fig. 1.3: The vector diagram of the conservation of momentum of the annihilation pair $(\vec{p})$ in the two-photon annihilation. The transverse and longitudinal components are denoted by $\perp$ and $||$ respectively.

$L\theta_z$

C_2

P_z

$\vec{P}$

L P_x O L

P_y

C_1

$L\theta_y$

P_z

P_x

P_y
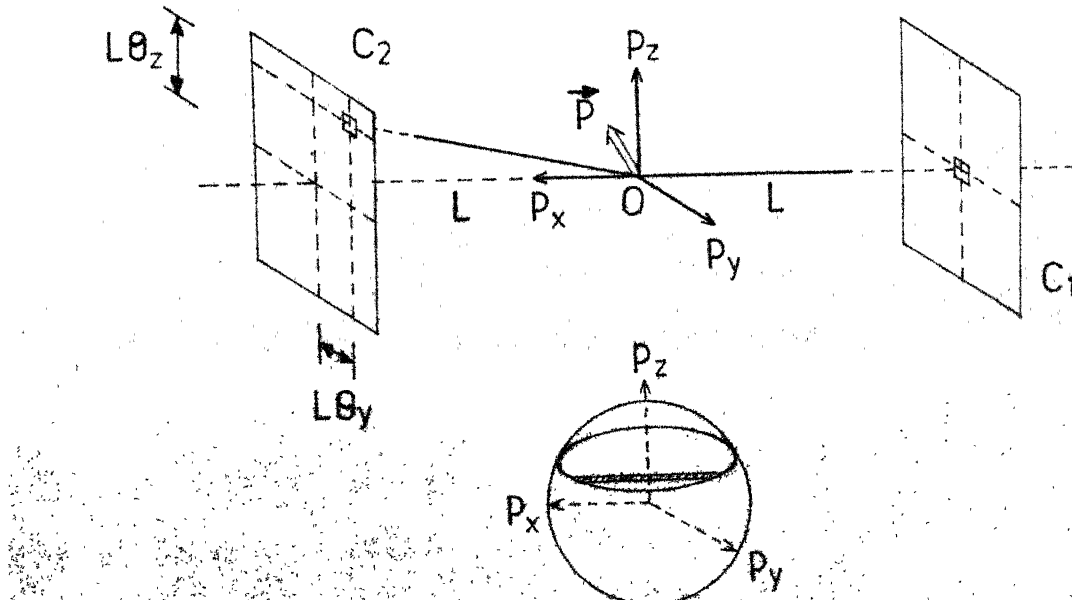
Fig. 1.4: Schematic geometry of the angular correlation of positron annihilation radiation (ACPAR).

important observable which provides interesting information about the sample under study. This is the most frequently used method in positron annihilation studies and it consists of using a ^{22}Na source sandwiched between the samples. The 1280 - keV gamma ray emitted by ^{22}Na is almost simultaneous with the emission of a positron and it signals the 'birth' of positron. The 511 - keV gamma ray accompanying the annihilation of positron signals the 'death' of the positron. The lifetime measurement then consists of using the 1280-keV gamma ray as the 'start' signal and the 511-keV gamma ray as the 'stop' signal in a time-to-amplitude converter system as in a typical nuclear lifetime spectrometer and of recording the time spectrum. Details of the experimental arrangements involved in a lifetime spectrometer are described in the literature [5,11].

Measurement of the Doppler broadening of the annihilation radiation lineshape is made with a high resolution gamma ray energy spectrometer involving a HP Ge or Ge(Li) detector, research amplifier and a data acquisition system (e.g. multichannel analyser), as described elsewhere [2,5,11]. There are also some multiparameter methods which determine more than one parameter and these are described in the literature [5,11]. Since the present work does not deal with the above methods we have not discussed them in detail.

1.3.2 Measurement of the angular correlation of positron annihilation radiation

We have seen earlier that the measurement of the angular correlation of positron annihilation radiation (ACPAR) leads to the determination of the momentum distribution of the annihilating positron-electron pair. The geometry of a typical ACPAR measurement is shown schematically in Fig. 1.4 where the double arrow represents the electron momentum vector $\vec{p}$. It was shown in Sec. 1.2 that the transverse component $p_\perp \equiv (p_y, p_z)$ is responsible for the deviation from collinearity of the two photons. If one of the photons is detected by a detector C_1 (Fig. 1.4) the second time-coincident photon will strike the other detector plane C_2 at a point whose coordinates are $y \simeq \theta_y L$ and $z \simeq \theta_z L$ (since both θ_y and θ_z are of the order of few milliradians) where L is the distance between the annihilation centre O and each of the counter planes. The two angles θ_y and θ_z are related to the momentum components p_y and p_z through the relations $\theta_z = p_z/m_0 c$ and $\theta_y = p_y/m_0 c$. The longitudinal component, p_x, gives rise to a Doppler energy shift ΔE which has a typical value of $\Delta E = 1-3$ keV away from $E_\gamma = m_0 c^2$ or ~ 511 keV. In order to achieve high counting rates the gamma ray detectors in the ACPAR experiment have high detection efficiency but poor ($\sim 10\,\%$ at 511 keV) energy resolution. As a result the Doppler energy shifts ΔE are not resolved and the momentum component p_x is undetermined or is integrated out. There are two main variations in the

geometry of the ACPAR experiment. In the so-called "long-slit (LS)" (or wide slit) geometry the detector on each side has an extended length along the p_y-axis in order to enhance the coincident counting rates. In such a measurement the information about the p_y-component is also integrated out and the LS ACPAR measurement yields the coincidence rate proportional to

$$N(p_z) = \int_{-\infty}^{\infty} \int_{-\infty}^{\infty} \rho(\vec{p}) \, dp_x \, dp_y \tag{1.7}$$

where $\rho(\vec{p})$ is the two-photon momentum density (TPMD) and where we have assumed that the horizontal angle subtended by the detectors is much larger compared to the angular resolution of the detectors along p_z.

By sacrificing the coincident counting rate one may restrict the dimensions of the detectors along the p_y-axis and employ the so-called "point slit (PS)" geometry. In this type of geometry one determines the p_y-component also and the ACPAR measurement yields a two-dimensional distributions

$$N(p_y, p_z) = \int_{-\infty}^{\infty} \rho(\vec{p}) \, dp_x \tag{1.8}$$

Having discussed the principles behind the LS and PS geometries we shall now describe the actual experimental arrangements used.

A schematic arrangement of a typical ACPAR set-up employing the LS geometry is shown in Fig. 1.5(a). Positrons emitted from a radioactive source like ^{22}Na (or ^{64}Cu or ^{58}Co)
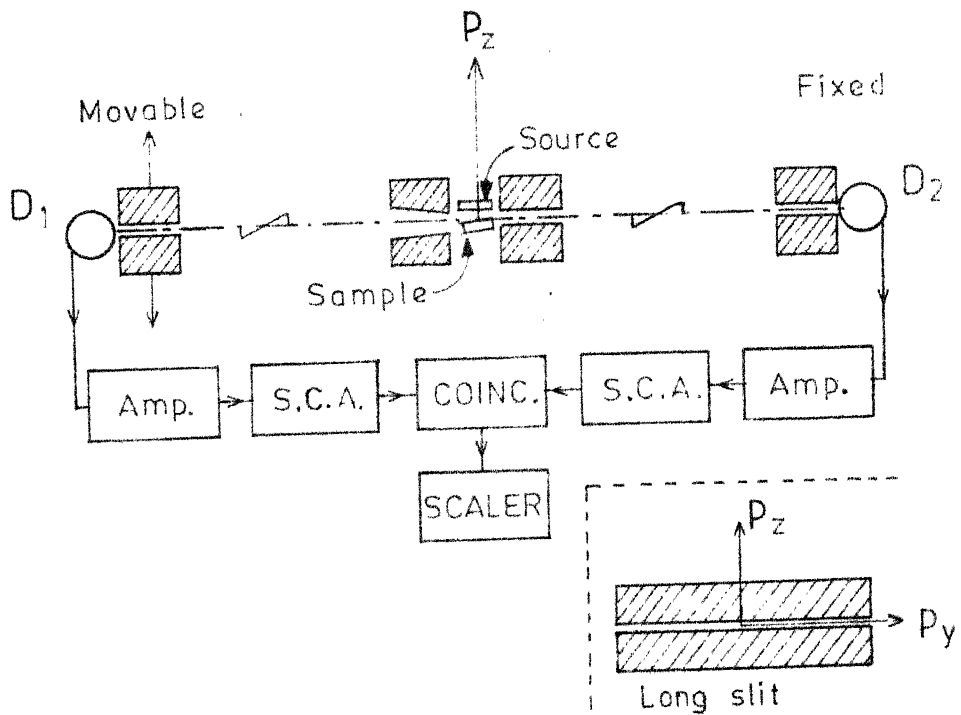
Fig. 1.5(a): Experimental arrangement to measure the ACPAR using the long-slit (shown in the inset) geometry.

13
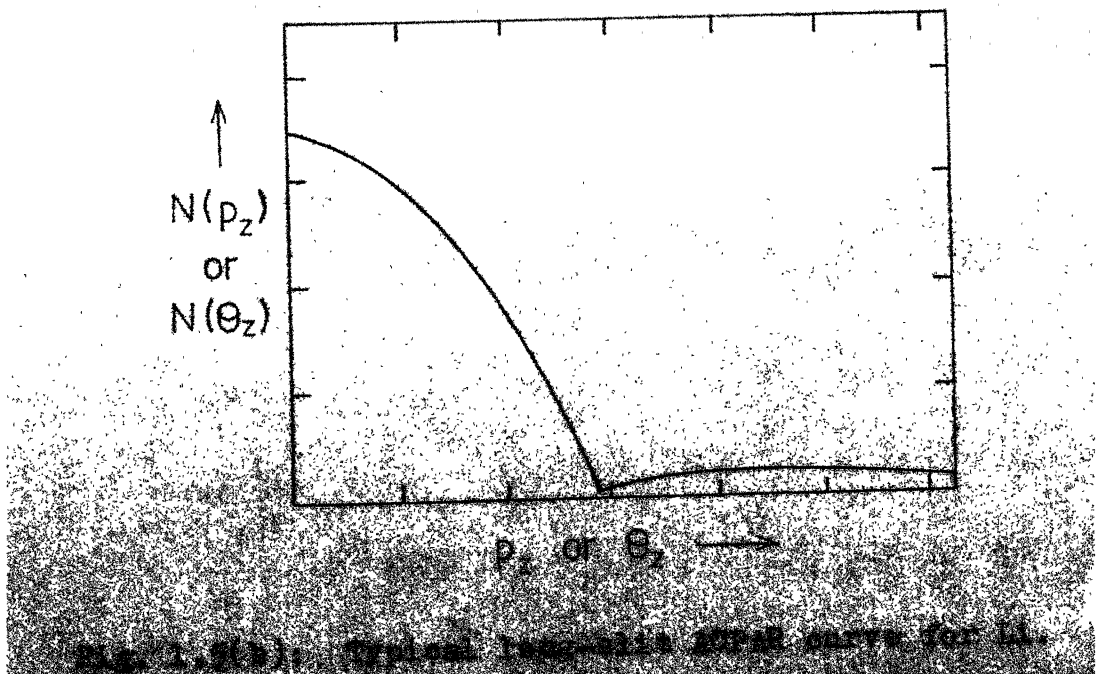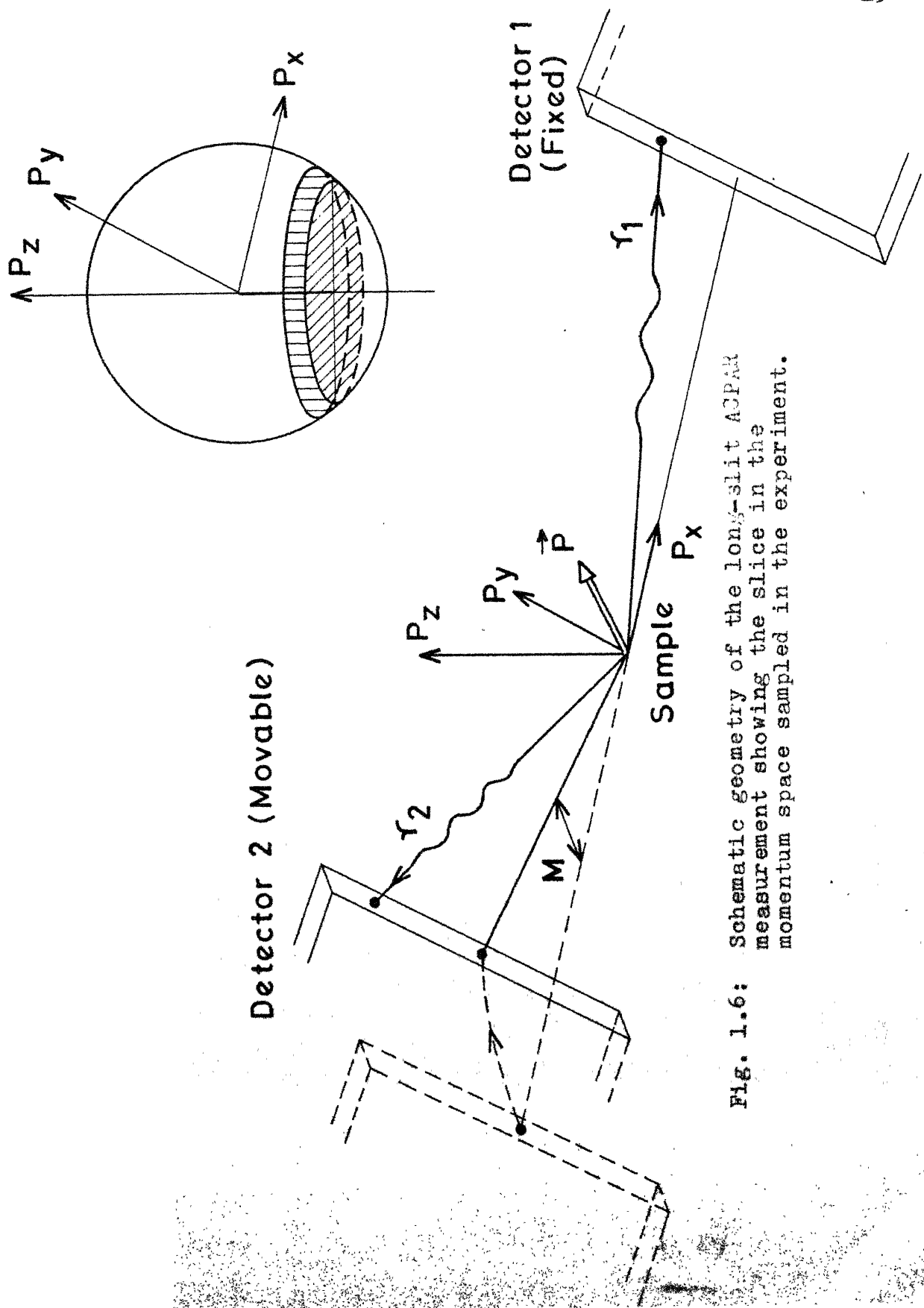
Fig. 1.6: Schematic geometry of the long-slit ACPAR measurement showing the slice in the momentum space sampled in the experiment.

are focussed by an electromagnet onto the sample under study.

The annihilation of positrons in the sample results in two gamma

rays ($E_\gamma = 511$ keV) which follow collimated paths towards the two

gamma ray detectors placed at about 3 meters on each side. The

gamma ray detectors consist of NaI(Tl) scintillators cylindrical

in shape with about 5 cm diameter and about 30-80 cm in length.

The axis of each detector is horizontal and the entrance window

is also horizontal and it subtends an angle of about 0.5 mrad

at the sample. One of the detectors is fixed while the other

is movable along the arc of the vertical circle centered at the

sample. The measurement consists of recording the coincidence

counting rate $N(\theta_z = p_z/m_0 c)$ as a function of θ_z. It is seen from

eq. (1.7) and Fig. 1.6 that the LS-ACPAR measurement counts the

number of electrons enclosed in a slice (parallel to the $p_x p_y$

plane) in the momentum space when this slice is moved parallel

to itself. In case of a free electron gas (i.e. Fermi sphere)

the LS-ACPAR curve $N(\theta_z = p_z/m_0 c)$ should be described by an

inverted parabola. Actual measurements in simple metals (e.g.

Li whose LS-ACPAR curve is shown in Fig. 1.5(b)) indeed show

that the ACPAR curve is an inverted parabola superimposed on a

broad Gaussian-like distribution. The parabolic part is attri-

buted to the nearly free (or conduction) electrons while the

Gaussian part arises out of the annihilation with inner core

electrons. A sharp break at the Fermi momentum $p = p_F$ is also

seen. The nature of the LS-ACPAR curve in a transition metal

is more complicated in that it is anisotropic and has a
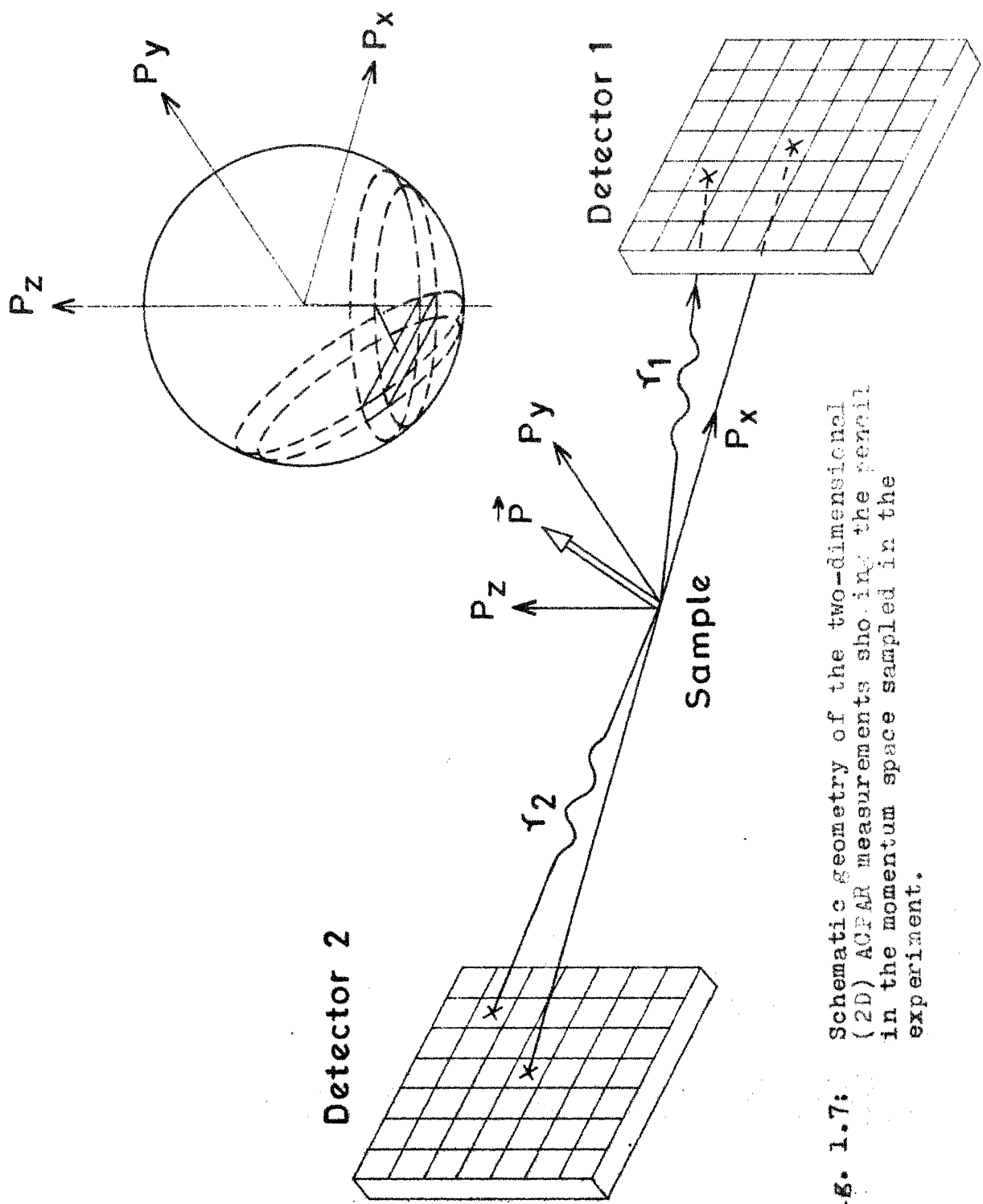
Fig. 1.7: Schematic geometry of the two-dimensional (2D) ACPAR measurements showing the momentum space sampled in the experiment.

substantial contribution from high momentum components.

The measurement of two-dimensional ACPAR curves, described by eq. (1.8), can be made by using different types of experimental arrangements. In view of the interesting information obtainable from the 2D-ACPAR measurements, much effort has been put in developing machines to measure the 2D-ACPAR curves [12,13]. Some of the machines developed so far are multiple NaI(Tl) detector system, multiwire proportional chamber system, NaI Anger camera system and multiple solid state detector system. We shall now briefly describe each of these arrangements.

A) Multiple NaI(Tl) detector system

Basically this is point-slit (PS) system whose detection efficiency is increased by using a two-dimensional array of NaI(Tl) detectors on each side of the source and specimen assembly (Fig. 1.7). Such a machine was first built by Berko and coworkers at the Brandeis University, U.S.A. and it employed 22 NaI(Tl) detectors subtending an angle of 0.5 mrad x 2.2 mrad at the sample. A newer version of this machine has recently been built at the Brandeis University and it consists of two sets of 32 NaI(Tl) detectors on each side, with the plane of detectors being 10 meters away. Each of the detector is a NaI(Tl) scintillator having a length of 5 cm and diameter of 3.8 cm coupled to RCA 6199 photomultiplier tube. Collimation of the gamma rays is made through rectangular lead point slits subtending an angle 0.5 x 1.5 mrad^2 at the sample. The number
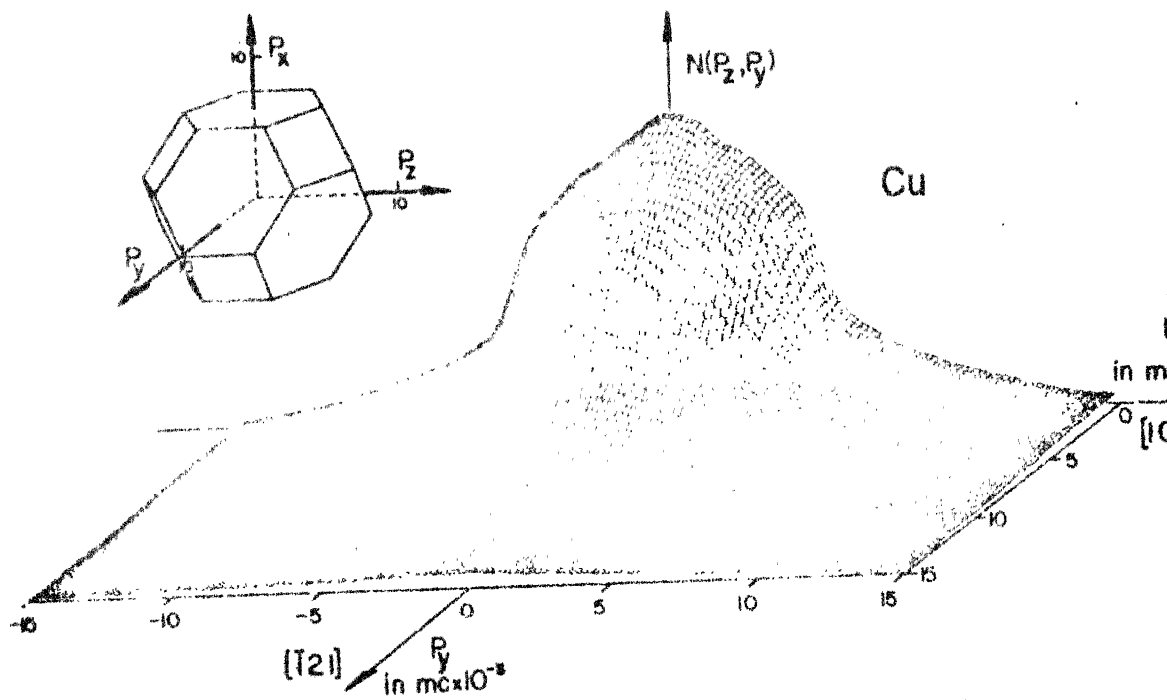
Fig. 1.8: The results of 2D-ACPAR measurements for Cu reported by Berko [12] for the crystal directions $p_z = [101]$, $p_y = [\bar{1}21]$.

of (p_y, p_z) pairs obtained by 32 x 32 cross coincidences is 109 and more intermediate points can be obtained by moving the counter assembly. Collection of data is done in steps of 0.2 mrad along the p_z direction in the range p_z = - 40 to + 40 mrad and in steps of 0.3 mrad along the p_y direction in the range p_y = 0 to 20 mrad. The source of positrons is the radioactive isotope ^{58}Co and with a 500 mCi of such a source the measured counting rate for Cu sample is 0.2 counts/sec per counter pair at $p_y = p_z = 0$ (with a total coincidence rate of 50 counts/sec). The counting period required to collect a full 2D-ACPAR curve with a 0.4 % accuracy is of the order of 10-14 days. The results of such 2D-ACPAR measurements for Cu reported by Berko [12] for the crystal directions p_z = [101], p_y = [$\bar{1}$21] are shown in Fig. 1.8 and they bring out the effects of the Fermi surface of Cu.

B) Multiwire proportional chamber system

The design of this system is, in principle, similar to the apparatus built by Howell and Osmon [14] who measured coincidence counting rate between a spark chamber and a point-slit NaI(Tl) detector to determine the 2D-ACPAR curve. The usefulness of the spark chamber machine was limited by the poor ($\sim$2 % detection efficiency. During the last few years the group at CERN, Geneva and the University of Geneva, Geneva, Switzerland have developed a 2D-ACPAR machine consisting of multiwire proportional chambers (MWPC) having high density converters to

increase the efficiency [12]. In this machine the annihilation
photon entering the chamber is detected through the photo-
electron formed by it after interaction with the high-Z
converter. The chamber has a sensitive area of 10 x 10 cm^2 and
the detection efficiency for the 511-keV gamma ray is about 12 %.
The two MWPC detector systems are placed 10 meters apart and the
data are recorded by a CAMAC system coupled to a PDP 11/40
computer system. The total coincidence counting rate is 10
coinc/sec while the effective angular resolution is 0.75 x 0.68
$mrad^2$ when a 30 mCi radioactive source of ^{22}Na and a copper
sample (10 x 1 mm^2) was used. The 2D-ACPAR curve for Cu
obtained with this MWPC system is similar [12] to that shown in
Fig. 1.8.

C) NaI Anger camera system

The position sensitive or Anger camera was developed
many years ago [15] and has been used for medical imaging for
many years. In principle the Anger camera consists of a large
NaI crystal optically coupled to several photomultiplier tubes
and the localization of the gamma ray detection point (or
position) is made by analysing these signals. A 2D-ACPAR
machine using a NaI Anger camera has been built by West and
coworkers at the University of East Anglia, U.K. [12]. The
Anger cameras used in this machine consist of two cylindrical
NaI scintillators 50.8 cm in diameter and coupled optically to
a closely packed array of 37 photomultiplier tubes each having

a diameter of 7.8 cm. The source and sample assembly is at the centre of two 'cameras' which are operated in coincidence. The distance between the two cameras can be changed from 2 to 20 meters. A typical total coincidence counting rate of the order of 120 coinc/sec (using a 20 mCi ^{22}Na source and an aluminium sample in the range -22 to +22 mrad) and an overall angular resolution of about 0.6 x 0.6 mrad^2 is reported.

D) Multiple solid state detector system

It was pointed out by Triftshäuser in 1971 that a 2D-ACPAR machine can be constructed by using a position sensitive multiple Ge-detector system. Such a 2D-ACPAR machine has been constructed at the Kernforschungsanlage, Jülich, Federal Republic of Germany [12]. This instrument consists of five point-slit CsI detectors on one side and a high purity germanium (Ge) position sensitive detector on the other side with a coincidence between the CsI detectors and the elements of the Ge detector. The dimensions of the Ge detector are 90 mm x 60 mm x 10 mm with a checkerboard type of design [12]. In a similar design, the research group of the Institute of Physical and Chemical Research Saitama, Japan has developed a 2D-ACPAR machine using large area planer Si(Li) detectors [12]. The data by these two types of 2D-ACPAR machine have not yet been reported in detail.

In the above we have described, in brief, the significant features of various experimental arrangements employed to measure the 2D-ACPAR curves $N(p_y, p_z)$. In the next section we

shall outline how the $N(p_y, p_z)$ curves can be calculated theoretically.

Before we conclude this section we wish to point out some distinct advantages offered by the 2D-ACPAR technique. In a pure metal the study of Fermi surfaces can be carried out by other conventional methods such as the de Haas-van Alphen effect, the magnetoresistance effect etc. with a precision higher than that offered by positron annihilation techniques. However these conventional methods cannot be used for the study of nondilute disordered allcys and high temperature phases of ordered materials because of the short mean free path of electrons under these conditions. Although there are other methods like Compton scattering, X-ray diffuse scattering, inelastic neutron scattering, Faraday effect etc. available for studying samples with solute concentration ≥ 1 %, the superior momentum resolution and the possibility to measure 2D-ACPAR curves make positron annihilation a powerful tool for studying nondilute alloys. Many such interesting studies have been reported recently [5,12].

The positron method has a serious drawback in that the sample under study should be free from defects. This restriction arises from the fact that a defect present in a metal can 'trap' the positron changing the TPMD significantly [5]. In our discussions throughout the present thesis we have limited ourselves to pure metals without any defects.

1.4 Theory of Angular Correlation of Positron Annihilation Radiation : Independent Particle Model

It was seen in the previous section that theoretical determination of both one-dimensional ACPAR curve, $N(p_z)$ by eq. (1.7) and the two-dimensional ACPAR curve, $N(p_y, p_z)$ by eq. (1.8) require calculation of the two-photon momentum density (TPMD) $\rho(\vec{p})$. Such calculations of the TPMD, $\rho(\vec{p})$, are done within the framework of the independent particle model using a standard band structure method [4,5]. The TPMD, $\rho(\vec{p})$, is the probability that the photon pair carries away a total momentum $\vec{p}$ and in the independent particle model one can write $\rho(\vec{p})$ in a metal as

$$\rho(\vec{p}) = \text{Const} \sum_{j,\vec{k},i}^{occ} f(\vec{k},j) \, |A_j(\vec{k},\vec{p})|^2 \, \delta(\vec{p}-\vec{k}-\vec{K}_i) \qquad (1.9)$$

where $f(\vec{k},j)$ is the occupation number such that $f(\vec{k},j) = 1$ for an occupied state and $f(\vec{k},j) = 0$ for an unoccupied state of the electron at $T = 0$ K, the overlap matrix element $A_j(\vec{k},\vec{p})$ is written as

$$A_j(\vec{k},\vec{p}) = \int_{Cell} \exp(-i\vec{p}.\vec{r}) \, \psi_{\vec{k},j}(\vec{r}) \, \psi_+(\vec{r}) \, d\vec{r} \qquad (1.10)$$

where $\psi_{\vec{k},j}(\vec{r})$ is the electron wavefunction for wavevector $\vec{k}$ and band index j and $\psi_+(\vec{r})$ is the positron wavefunction for the state $\vec{k}_+ = 0$ in its lowest energy state and $\vec{K}_i$'s are the reciprocal lattice vectors.

It was pointed out by Berko and Plaskett [16] that
because the crystal momentum $\vec{k}$ differs from the real momentum
$\vec{p}$ by $\vec{K}_i$, an electron with a wave vector $\vec{k}$ will contribute to
the TPMD not only at $\vec{p} = \vec{k}$ but also at $\vec{p} = \vec{k} + \vec{K}_i$ (Fig. 1.9)
with amplitudes $A_j(\vec{k},\vec{p})$ through eq. (1.9). The contribution
at $\vec{p} = \vec{k}$ (with $\vec{K}_i = 0$) are termed 'normal' contributions while
the contributions at the high momenta $\vec{p} = \vec{k} + \vec{K}_i$ (with $\vec{K}_i \neq 0$)
are termed as Umklapp contributions or the high momentum
components (HMC). The summation in (1.9) is carried over the
occupied states and as a result the TPMD, $\rho(\vec{p})$, is expected
to show discontinuity not only at $\vec{p} = \vec{k}_F$ (where $\vec{k}_F$ is the
Fermi momentum) in the first zone but also at the higher
momenta $\vec{p} = \vec{k}_F + \vec{K}_i$. Besides these discontinuties which
arise out of the Fermi surface, the general shape of the
TPMD, $\rho(\vec{p})$, is determined by the electron wavefunction
$\psi_{\vec{k},j}(\vec{r})$ via eq. (1.10). In the case of a transition metal
like V which has partially occupied $3\underline{d}$ bands, the TPMD $\rho(\vec{p})$
becomes anisotropic because of this dependence on $\psi_{\vec{k},j}(\vec{r})$.
There is also a symmetry selection rule [17] which allows only
bands of certain symmetry to contribute to the TPMD and this
aspect will be discussed in detail in Chapter 4.

In order to illustrate the important features of the
TPMD, $\rho(\vec{p})$, in real metals we take the example of one-
dimensional nearly-free-electron (NFE) and tight binding (TB)
model for metals. Three cases corresponding to different
locations of the FS with respect to the Brillouin zone (BZ)
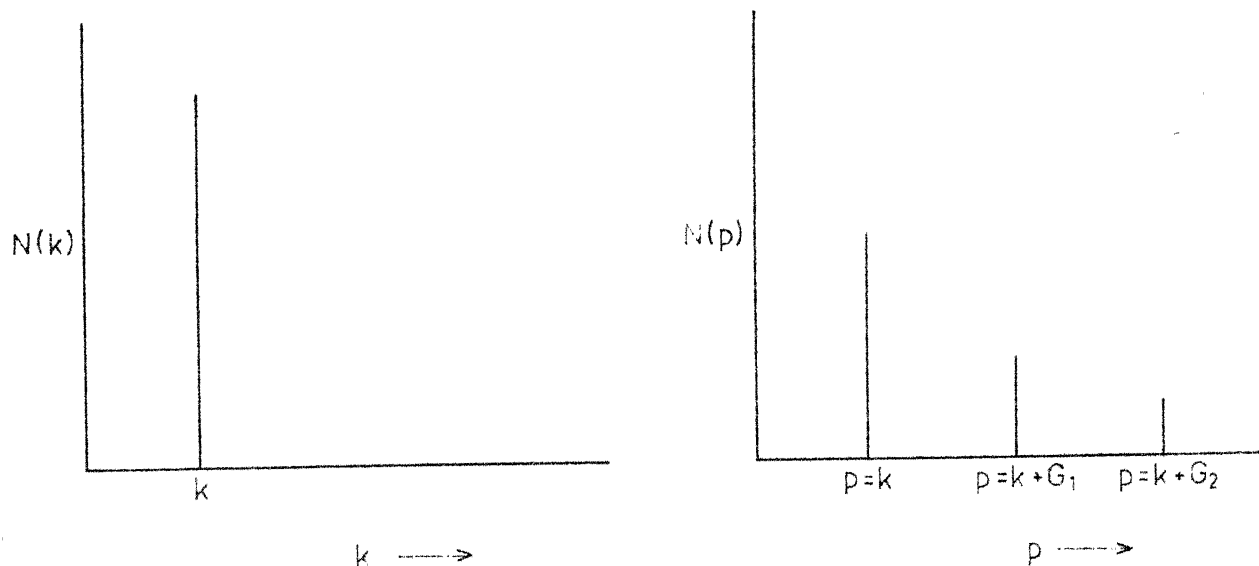
Fig. 1.9: One-dimensional electron momentum distribution in the k- and p-space following Berko and Plaskett [16].
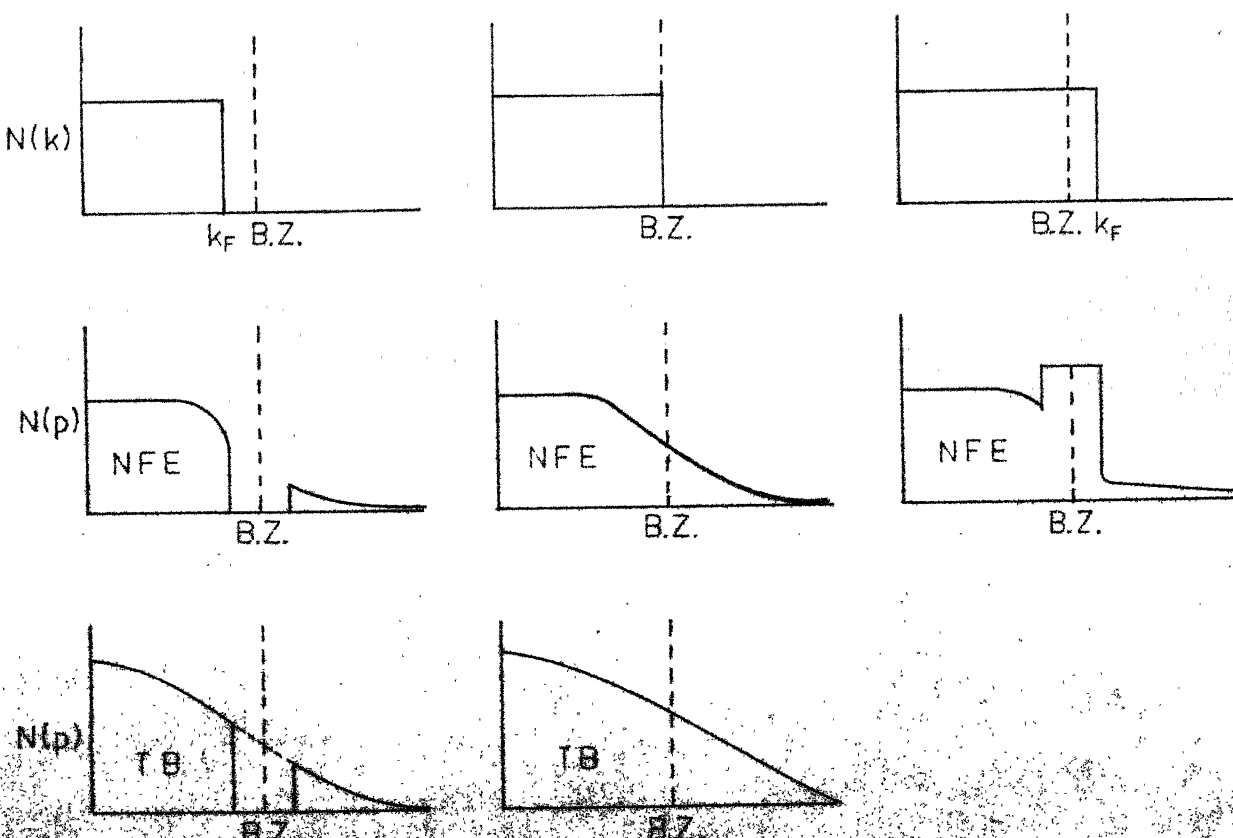
Fig. 1.10: One-dimensional electron momentum distribution in k-space and p-space in the nearly-free-electron (NFE) and tight-binding (TB) model for three different locations of the fermi surface (see text)[16].

boundary are shown in Fig. 1.10. In the case (a) the FS is
within the first BZ while in the case (c) the FS is in the
second BZ (using the extended zone scheme). For the case (b)
it is assumed that the FS coincides with the BZ boundary. The
schematic trends in Fig. 1.10 show how the FS breaks appear,
for the case (a) in the $\vec{p}$-distributions at higher momenta. Case
(b) illustrates how the $\vec{p}$-distribution becomes continuous as
soon as the $\vec{k}$-distributions touch the BZ. In the case (c) one
notices that the FS discontinuity is more sharp in the second
BZ than in the first BZ.

Coming back to eqs. (1.9) and (1.10) we see that the
calculation of the TPMD, $\rho(\vec{p})$, should be preceded by a band
structure calculation of the metal so that the FS as well as
the electron wavefunctions $\psi_{\vec{k},j}(\vec{r})$ are determined. This
stage of computation involves the standard problem of band
structure calculation and it is discussed later in the thesis.
Next problem is the determination of the positron wavefunction
in the metal and this is treated in Sec. 3.4. Having calcula-
ted the electron and positron wavefunctions one can determine
the TPMD by the help of eqs. (1.9) and (1.10). Finally the
calculation of the ACPAR curves can be performed with the help
of eqs. (1.7) and (1.8). In particular the calculation of the
2D-ACPAR curves $N(p_y, p_z)$ require determination of theoretical
TPMD, $\rho(\vec{p})$, at several $\vec{p}$-points before one can evaluate

$$N(p_y, p_z) = \int_{-\infty}^{\infty} \rho(\vec{p}) \, dp_x \qquad (1.8)$$

through a line integration.

It should be pointed out that the positron-electron many body effects affect the positron lifetimes very seriously but the ACPAR curves only marginally. These corrections will be discussed in Sec. 3.5. In the next section we shall outline how one can compare the theoretical and experimental results for the ACPAR measurements.

1.5 Comparison Between Theory and Experiment: Reconstruction of Momentum Distributions.

In the last two sections we have seen how the ACPAR curves can be measured experimentally and how they can be calculated theoretically. There are two main approaches for comparing the experiment with theory. In the first approach one calculates the theoretical TPMD, $\rho(\vec{p})$, by using a band structure method and then uses eqs. (1.7) or (1.8) to obtain the ACPAR curves. For an accurate comparison one will have to apply correction for the finite angular resolution of the apparatus as well as for the finite length of the long slit in the LS-ACPAR apparatus [5]. Such a calculation of the ACPAR curve from the TPMD, $\rho(\vec{p})$, is rather straightforward for the 2D-ACPAR curves because it involves a line integral (1.8) which can be computed by determining $\rho(\vec{p})$ on a rectangular momentum grid in the $(p_x \ p_z)$ plane $p_y = $ const. This procedure, followed by us in the present work, will be illustrated in Chapter 4. As for the 1D-ACPAR curves are concerned the surface integral involved in (1.7) can be calculated either

by a direct integration in the momentum space [18] or by the help of Fourier-Hankel transforms [19,20].

In the second approach one attempts to reconstruct the TPMD from ACPAR curves measured for several single crystal directions and compares the reconstructed TPMD with the theoretical results for $\rho(\vec{p})$. We shall now briefly describe the methods used for the reconstruction of the momentum distributions.

The method most commonly used for the LS-ACPAR curves is due to Mijnarends [20] and is based on the Fourier-Hankel transforms. In this method the momentum density $\rho(\vec{p})$ is expanded as

$$\rho(\vec{p}) = \sum_{\ell \, \nu} \rho_{\ell\nu}(p) \, F_{\ell\nu}(\Omega_{\vec{p}}) \qquad (1.11)$$

where $\Omega_{\vec{p}}$ describes the orientation of $\vec{p}$ while $F_{\ell\nu}(\Omega_{\vec{p}})$ are the lattice harmonics which form an orthonormal set of invariant linear combinations of spherical harmonics of order ℓ. The label ν is used to distinguish different harmonics of the same order and symmetry. Only the harmonics having $\ell = 0,4,6,8,10,$ 12 (twice), 14 --- will contribute for cubic lattices like V (bcc). Two orthogonal co-ordinate systems R_c (fixed to the crystal) and R_a (fixed to the apparatus) are used. The lattice harmonics are defined in the system $R_c \equiv (\xi, \eta, \zeta)$ while the z-axis is selected in the system $R_a \equiv (x, y, z)$. By a suitable rotation through the Euler angles (α, β, γ) the systems R_c and R_a can be made to coincide.

The lattice harmonics $F_{\ell\nu}$ ($\Omega_{\vec{p}}$) can be further expanded in terms of the spherical harmonics $Y_{\ell m}(\Omega_{\vec{p}})$ by the following relation

$$F_{\ell\nu}(\Omega_{\vec{p}}) = \sum_m a_{\ell m\nu} Y_{\ell m}(\Omega_{\vec{p}}) \tag{1.12}$$

Following Mijnarends the LS-ACPAR curve $N_{\beta\alpha}(p_z)$ is expanded as

$$N_{\beta\alpha}(p_z) = 2\pi \sum_{\ell\nu} F_{\ell\nu}(\beta,\alpha) g_{\ell\nu}(p_z) \tag{1.13}$$

where the angles (β,α) denote a particular orientation of the single crystal specimen and

$$g_{\ell\nu}(p_z) = \int_{p_z}^{\infty} \rho_{\ell\nu}(p) P_\ell(p_z/p) \, p\,dp \tag{1.14}$$

where P_ℓ are the Legendre polynomials.

Equations (1.11) to (1.14) constitute the scheme for the reconstruction of $\rho(\vec{p})$ which proceeds as follows. A number of LS-ACPAR curves, $N(p_z)$, are measured for different single crystal orientations (α,β). The expansion (1.13) is truncated after a finite number of terms, m, such that $m \leq n$ where n is the number of orientations (α,β) for which measurements are made. By fitting experimental data, $N(p_z)$, in eq. (1.13), one solves for $g_{\ell\nu}(p_z)$ and then obtains $\rho_{\ell\nu}(p)$ from the Fourier-Hankel transform

$$\rho_{\ell\nu}(p) = -\frac{1}{p} \int_0^p g_{\ell\nu}''(z) P_\ell(z/p) \, dz \tag{1.15}$$

$$= -\frac{1}{p} \left[\frac{dg_{\ell\nu}(p)}{dp} - \frac{\ell(\ell+1)}{2p} g_{\ell\nu}(p) \right.$$

$$\left. + \frac{1}{p^2} \int_0^p g_{\ell\nu}(z) \, P_\ell'(\frac{z}{p}) \, dz \right] \tag{1.16}$$

The TPMD, $\rho(\vec{p})$, is then synthesized from the $\rho_{\ell\nu}(p)$ using (1.11). This method has been used for the reconstruction of the EMD in several metals [3,5]. One problem inherent in this method is the arbitrary choice of m while truncating (1.13).

The problem which is more closely related to the subject of the present thesis is the reconstruction of the TPMD, $\rho(\vec{p})$, from the 2D-ACPAR curves, $N(p_y, p_z)$, measured experimentally for a set of $\{p_x, p_y, p_z\}$ directions. There are no reported measurements on the 2D-ACPAR curves for V in the literature. Nevertheless, the theoretical TPMD curves, $\rho(\vec{p})$, calculated by us and presented in Chapter 4 can provide a theoretical basis to compare the reconstructed TPMD once experimental data become available.

There are several methods suggested for reconstructing TPMD from the 2D-ACPAR curves [21-23]. Majumdar [21] was the first to suggest a method which is based on Mellin transforms and which was aimed directly on the problem under consideration.

Let us consider, for simplicity, the measurements in the ''fixed configuration'' such that the axes of cubic crystal coincide with the axes of measuring system. In the co-ordinates

(R_m) of the measuring apparatus we can then write $\rho(\vec{p})$ as

$$\rho(\vec{p}) = \sum_{\ell\nu m} \ell_{\ell m}^{\nu} \; P_{\ell}^{-m} \; (\cos\theta) \; \cos m\,\varnothing \; \rho_{\ell\nu}(p); \quad (m \geq 0)$$

$$\cdots \quad (1.17)$$

One can write eq. (1.8) in the polar co-ordinates $(R, \varnothing)$ as

$$N(p_y, p_z) \equiv S(R, \varnothing) = \sum_{m} g_m(R) \; \cos m\,\varnothing \qquad (1.18)$$

where $g_m(R)$ is the Fourier cosine transform of the point-slit geometry data given by

$$g_m(R) = \sum_{\ell\nu} \ell_{\ell m}^{\nu} \; f_{\ell\nu}^{m}(R) \qquad (1.19)$$

with

$$f_{\ell m}^{\nu}(R) = \int_{R}^{\infty} P_{\ell}^{-m} \left[(1 - R^2 p^{-2})^{\frac{1}{2}} \right] \rho_{\ell\nu}(p) \; (1 - R^2 p^{-2})^{-\frac{1}{2}} \, dp$$

$$\cdots \quad (1.20)$$

To find out $\rho_{\ell\nu}(p)$ one has to solve eq. (1.19) for $f_{\ell\nu}^{m}$ and then eq. (1.20) for $\rho_{\ell\nu}(p)$. Majumdar suggested constructing the Mellin transform (Re s > 1)

$$\hat{f}_{\ell\nu}^{m}(s) = \int_{0}^{\infty} R^{s-2} \; f_{\ell\nu}^{m}(R) \, dR \qquad (1.21)$$

for writing the solution of eq. (1.20) as

$$\rho_{\ell\nu}(p) = \frac{1}{2\pi i} \int_{\sigma-i\infty}^{\sigma+i\infty} \frac{ds}{p^s} \; \frac{2^{1+m} \; \Gamma(1+m) \; \Gamma(\frac{1}{2}(s+m))}{\pi^{\frac{1}{2}} \; \Gamma(\frac{1}{2}(s+m+1))} \; x$$

$$\frac{\hat{f}_{\ell\nu}^{m}(s)}{{}_3F_2(\frac{1}{2}(\ell+m+1), -\frac{1}{2}(\ell-m), \frac{1}{2}(s+m+1); 1+m, \frac{1}{2}(s+m); 1)} \qquad (1.22)$$

where $\sigma > 1$.

In eq. (1.19) $f_{\ell\nu}^m$'s are again underdetermined as before but it is easy to find out the maximum number of ℓ-values to be used because the m-values in using eq. (1.18) with the experimental data are known. It may be noted here that any information about the m-values cannot be obtained using the LS-ACPAR data. Above procedure has been discussed in detail by Majumdar [21]. His method is more systematic and gives a unique criterion for deciding where to truncate the expansion (1.17).

Cormack [22] has suggested a method to find a real function in a finite region of a plane if the line integrals along all the straight lines intersecting the region are given. The solution given is applicable to three problems of interest in radiology and radiotherapy (i) the determination of a variable X-ray absorption coefficient in two dimensions; (ii) the determination of the positron annihilations when there is an inhomogeneous distribution of positron emitter in the matter ; and (iii) the determination of variable density of matter with constant chemical composition using energy loss of charged particles in matter. In particular these methods can be used for the reconstruction of the TPMD from 2D-ACPAR measurements.

Recently Pecora and Ehrlich [23] have reported a method to reconstruct the momentum distribution from point-slit geometry data, particularly the crossed slit geometry. They

have used the following expression

$$N_\alpha (p_z) = \int_{-\infty}^{\infty} \rho(p_x, \; p_y = 0, \; p_z) \; dp_x \tag{1.23}$$

for the experimental data in a plane with the z-axis in the co-ordinate system of experimental arrangement making an angle α with the reference direction in the plane. They have expanded the $\rho(\vec{p})$ in a Fourier series in polar co-ordinates in the plane using the relation

$$\rho(\vec{p}) = \sum_{m=-\infty}^{\infty} \rho_m(p) \; e^{im\emptyset} \tag{1.24}$$

where $p \equiv |\vec{p}|$ and $\emptyset$ is the angle of $\vec{p}$ with respect to the reference direction. The $\rho(\vec{p})$ must be real and this results in the following condition

$$Re \, [\rho_m(p)] \equiv \rho_m^r(p) = \rho_{-m}^r(p)$$

and

$$Im \, [\rho_m(p)] = \rho_m^i(p) = -\rho_{-m}^i(p)$$

It is therefore required to solve for the coefficients $\rho_m(p)$ only for $m \geq 0$. To find out $N_{\alpha_j}(p_z)$ one uses eq. (1.24) with $\emptyset = \alpha_j + \theta$ where α_j is the angle between the z-axis and the reference direction while θ is the angle between $\vec{p}$ and the z-axis. One can write

$$\rho(\vec{p}) = \sum_{-\infty}^{\infty} e^{im\alpha_j} \; \rho_m(p) \; e^{im\theta} \tag{1.25}$$

and

$$N_{\alpha_j}(p_z) = \sum_{-\infty}^{\infty} e^{im\alpha_j} \int_{-\infty}^{\infty} \rho_m(p) \; \cos m\theta \; dp_x \tag{1.26}$$

The eq. (1.26) can be rewritten as

$$N_{\alpha_j}(p_z) = \sum_{m=-\infty}^{\infty} g_m(p_z) \, e^{im\alpha_j} \tag{1.27}$$

with

$$g_m(p_z) = 2 \int_{p_z}^{\infty} \frac{p\,dp}{(p^2-p_z^2)^{\frac{1}{2}}} \, \rho_m(p) \, T_m(p_z/p) \tag{1.28}$$

where the Chebychev polynomial of the first kind, T_m, is defined by

$$T_m(x) = \cos[m \cos^{-1} x]$$

Now one has to solve eq. (1.27) for $g_m(p_z)$ and then eq. (1.28) for $\rho_m(p)$. The details about solving these equations are given by Pecora and Ehrlich [23]. They have tested this method for the hypothetical free electron gas and analysed the effect of errors in the data on the reconstructed, $\rho(\vec{p})$. They have also applied this method to real data for Cu and tried to find out the information about various quantities like p_F. They found their results to be in remarkably good agreement with the theoretically predicted and reconstructed $\rho(\vec{p})$ for Cu in the (100) plane. They were able to show that the data for a minimum number of crystal orientations can provide rich information about, $\rho(\vec{p})$. This method appears to be promising and future applications of this method for the reconstruction of the TPMD from experimental data should provide considerable interest.

1.6 Motivation Behind the Present Work

In the previous sections we have pointed out that the
2D-ACPAR method is well-suited for testing the band structure
and Fermi surface of metals and alloys _via_ the two-photon
momentum distributions. Earlier work on the 2D-ACPAR results
for Al [24] and Cu [25,26] have shown that for a successful
interpretation of the experimental data it is essential to
perform theoretical calculations made by band structure
methods. Such calculations are particularly important for
those transition metals for which the 3d band is partially
occupied and for which the _d_ wavefunctions play a major role
in building the TPMD through eq. (1.10). One such metal is
V belonging to the group V B metals (i.e. V, Nb and Ta). The
band structure and FS of these three metals V, Nb and Ta are
similar and they depend on the crystal potential, exchange
character, self-consistency, electron configuration and the
band structure method used in the calculations. The calculated
as well the measured 1D-ACPAR curves in V have already shown
a highly anisotropic nature which could be understood in
terms of the band structure and Fermi surface of V.

We therefore thought it interesting to calculate the
TPMD and the 2D-ACPAR curves in V using a band structure
method based on Hubbard's approximate scheme. The choice of
the crystal potential for metallic V for these calculations
was based on the following considerations. Under the
auspices of the International Union of Crystallography a

Special Commission on Electron Charge, Spin and Momentum
Density was formed in 1972. In 1975 this Commission piloted
a special project to determine the accuracy of the theoretical
Compton profiles and X-ray scattering factors for metallic
V. Our research group took part in this International
project and has calculated the electron momentum distribution
(for Compton scattering) and the Compton profiles [27] using
Hubbard's fast approximate scheme. These calculations used
the standard lattice potential for metallic V specially
constructed by Mijnarends [28] for this project. We have,
therefore, used the same crystal potential for V and have
extended the previous work on this project by calculating
the two-photon momentum distribution (for positron annihila-
tion) and the 2D-ACPAR curves in V.

The aim of the present work is to examine the effects
of band structure on the TPMD and the 2D-ACPAR curves in V.
At present there is lot of interest in the electronic struc-
ture of transition metal hydrides. The hydrides and deuterides
of vanadium have been studied both theoretically and experi-
mentally [29]. We have, therefore, extended our results for
V to $VD_{0.72}$ using the rigid band protonic model and have
calculated the 2D-ACPAR curves in $VD_{0.72}$. The results of
the present work can give a better idea about which FS
sheets can be investigated in a particular choice of
$\{p_x, p_y, p_z\}$ direction in a 2D-ACPAR experiment with V and
VD_x.

At present there is no available experimental data on the 2D-ACPAR measurements in V or VD_x. We hope that the results presented in Chapters 4 and 5 can provide a theoretical basis to understand future experimental results.

REFERENCES

1. W.A. Reed, Acta Cryst. A32, 676 (1976).

2. R.M. Singru, Phys. Status Sol. (a) 30, 11 (1975).

3. B. Williams, ed. Compton Scattering, McGraw-Hill London (1977).

4. R.N. West, Adv. Phys. 22, 263 (1973).

5. P. Hautojärvi, ed. Positrons in Solids, Springer-Verlag, Berlin-Heidelberg (1979).

6. I.E. McCarthy and E. Weigold, Phys. Report 27C, 275 (1976).

7. A.I. Akhiezer and V.B. Berestetskii, Quantum Electrodynamics, Interscience Publishers, New York (1965).

8. P.A.M. Dirac, Proc. Camb. Phil. Soc. Math. Phys. Sci. 26, 361 (1930).

9. V.B. Berestetskii, E.M. Lifshitz and L.P. Pitaevskii, Relativistic Quantum Theory, Pergamon Press, Oxford (1971), p. 330.

10. S. Kahana, Phys. Rev. 117, 123 (1960); Phys. Rev. 129, 1622 (1963).

11. J.A. Merrigan, J.H. Green and S.J. Tao in Physical Methods of Chemistry, eds. A Weissberger and B.W. Rossiter, Vol. 3, Part III D, Wiley, New York (1972), p. 501.

12. R. Hasiguti and K. Fujiwara, eds. , Positron Annihilation, Proceedings of the Fifth International Conference on Positron Annihilation, April 8-11, 1979, Lake Yamanaka, Japan; The Japan Institute of Metals, Japan (1979).

13. R.M. Singru in Positron Annihilation, Proceedings of the National Symposium on Positron Annihilation, Delhi, India April 2-4, 1979, eds. P.C. Jain and R.M. Singru, South Asian Publishers, New Delhi (1980), p. 163.

14. M.R. Howells and P.E. Osmon, J. Phys. F2, 277 (1972); J. Phys. E4, 929 (1971).

15. H.O. Anger, Rev. Sci. Instrum. $\underline{29}$, 27 (1958).

16. S. Berko and J.S. Plaskett, Phys. Rev. $\underline{112}$, 1877 (1958).

17. R. Harthoorn and P.E. Mijnarends, J. Phys. F$\underline{8}$, 1147 (1978).

18. S. Wakoh and J. Yamashita, J. Phys. Soc. Jpn. $\underline{35}$, 1406 (1973).

19. A. Seth and D.E. Ellis, Phys. Rev. A$\underline{13}$, 1083 (1976).

20. P.E. Mijnarends, Phys. Rev. $\underline{160}$, 512 (1967).

21. C.K. Majumdar, Phys. Rev. B$\underline{4}$, 2111 (1971); C.K. Majumdar in Positron Annihilation, Proceedings of the National Symposium on Positron Annihilation, Delhi, India, April 2-4, 1979, eds. P.C. Jain and R.M. Singru, South Asian Publishers, New Delhi (1980), p. 89.

22. A.M. Cormack, J. Appl. Phys. $\underline{34}$, 2722 (1963); J. Appl. Phys. $\underline{35}$, 2908 (1964).

23. L. Pecora and A.C. Ehrlich, Phys. Rev. B$\underline{19}$, 719 (1979).

24. J. Mader, S. Berko, H. Krakauer and A. Bansil, Phys. Rev. Letts. $\underline{37}$, 1232 (1976).

25. P.E. Mijnarends and R.M. Singru, Phys. Rev. B$\underline{19}$, 6038 (1979).

26. S. Wakoh, S. Berko, M. Haghhooie and J.J. Mader, J. Phys. F$\underline{9}$, L231 (1979).

27. Krishna Gandhi K.R. Ph.D. thesis, Indian Institute of Technology, Kanpur India (Unpublished) 1978.

28. P.E. Mijnarends ''Construction of a Muffin-Tin Potential for Metallic Vanadium'' Report RCN-76-010, Reactor Centrum Nederland, Petten (N.H.) The Netherlands (Unpublished) 1976.

29. G. Alefeld and J. Völke, eds. Hydrogen in Metals I and II, Springer-Verlag, Berlin (1978).

Chapter 2

REVIEW OF THE THEORETICAL AND EXPERIMENTAL STUDIES
OF THE BAND STRUCTURE OF VANADIUM

2.1 Introduction

The study of Fermi surface (FS) of metals and alloys
plays an important part in the investigation of their elec-
tronic properties. Determination of the FS topology is
particularly interesting in transition metals having
partially occupied d bands. In the past there has been
considerable interest in the experimental as well as theore-
tical study of the band structure and Fermi surface of the
vanadium group of metals (i.e. the V B group isoelectronic
metals, V, Nb and Ta). The outermost d-shell (e.g. 3d for
V) is partially occupied in all these three metals and the
Fermi level, therefore, lies amongst the d bands thus
resulting in a complicated topology of the FS. These
interesting features of the FS topology can be determined
by a comparison between theory and experiment. In case of
the transition metals, the calculated band structure, Fermi
surface and the electron wavefunctions are particularly
sensitive to the band structure method, crystal potential,
outer electron configuration, exchange parameter etc. used
in solving the Hartree-Fock-Slater equations (in the
independent particle model)

$$H \; \psi(\vec{r}) \; = \; [- \; \nabla^2 \; + \; V_c(\vec{r}) + V_x(\vec{r})] \; \psi(\vec{r}) \qquad (2.1)$$

where $V_c(\vec{r})$ is the non-exchange potential experienced by the electron in the Coulomb field of all ions and all other electrons while $V_x(\vec{r})$ is the exchange potential which arises because the electrons have spin, are indistinguishable and obey the Pauli exclusion principle. In eq. (2.1) we have used the atomic units : $\hbar = 1$, $m = 1$, $e = 1$ while the energies are expressed in Rydbergs.

A detailed description of how eq. (2.1) can be solved by different band structure methods is given in several excellent reviews [1-5] and will not be attempted here. In the next section we shall briefly outline the different theoretical calculations of the band structure of metallic vanadium and summarise the experimental results for the FS topology of V. In Sec. 2.3 we shall summarise the experimental results on the electron momentum distributions in V as investigated by the methods of positron annihilation and Compton scattering.

2.2 Theoretical Calculations of the Band Structure of V

The first band structure calculation of V was reported by Mattheiss [6] who used a non-self-consistent (NSC) augmented-plane-wave (APW) method and showed that the band structure of V was affected significantly by the change in the relative population of the $(3\underline{d})$ and $(4\underline{s})$ shells. In a subsequent work Mattheiss [7] predicted the FS topology for V, Nb and Ta. His results showed that

the FS of vanadium group of metals consists of two hole
sheets. The first one, arising out of the second band, forms
a closed surface centered on the point Γ and is octahedral in
shape. The second sheet, contributed by the third band,
consists of two geometries : (i) jungle-gym (or JG) struc-
ture of hole arms along the <100> directions and (ii) large
ellipsoids around the points N. The FS topology deduced by
Mattheiss [7] from the band structure of Fe, however, showed
a neck along ΓN due to the third band.

A band structure calculation by Snow and Waber [8]
using a NSC APW method with full ($\alpha = 1$) Slater exchange
favoured an outer electron configuration $(3\underline{d})^4$ $(4\underline{s})^1$ for V
when a comparison with experiment was made.

A NSC APW calculation of the band structure of V was
made by Anderson et al. [9] who assumed a $(3\underline{d})^3$ $(4\underline{s})^2$
configuration and used two different values of the exchange
parameters $\alpha = 1$ and $\alpha = 2/3$. These authors observed that
the $\underline{d}$-bandwidth decreased with increase in α. When their
theoretical results were compared with the experimental data
obtained by photoemission [10] and de Haas-van Alphen effect
[11] studies the $\alpha = 1$ type of exchange was preferred. The
band structure of V was also calculated by Christensen for
the $(3\underline{d})^4$ $(4\underline{s})^1$ configuration and these results agreed with
those of Mattheiss [6]. Yasui et al. [12] made a self-
consistent (SC) calculation on V using a modified tight
binding method for the $\underline{d}$ electrons and an OPW method for

the $\underline{s}$ electrons. A comprehensive calculation of the band structure of V was made by Papaconstantopoulos et al. [13] using a SC APW method and a $(3\underline{d})^3$ $(4\underline{s})^2$ configuration. These authors reported their calculations for two values of the lattice constant a_0 : (i) normal lattice constant a_0 with $\alpha = 1$ and $\alpha = 2/3$ and (ii) reduced lattice constant $a = 0.95\,a_0$ with $\alpha = 2/3$. When the different theoretical calculations were compared to the experimental data obtained by photoemission [10] and de Haas van Alphen [11] methods the SC calculation using $\alpha = 2/3$ gave a good agreement. These authors also found that the band structure and FS topology of V showed significant changes on changing the lattice parameter from a_0 to $0.95\ a_0$.

Hattox et al. [14] have reported a SC APW band structure calculation of V employing a statistical exchange X_α [3] muffin-tin approximation. These authors have calculated cohesive energy, pressure and magnetization for several values of the lattice parameter.

A detailed study of the band structure and FS of V has been carried out by Wakoh and Yamashita [15] using a SC KKR method. In order to match the experimental results on the dimensions and shape of FS these authors used a phenomenological state-dependent potential having different energy dependence for the $d\epsilon$ and $d\gamma^2$ states. Their calculations gave a good description of the data for FS topology and X-ray form factors. Using this state-dependent potential

these authors also calculated directional Compton profiles
[16] and positron angular correlation curves [17] and we
shall discuss these results later on.

The band structure calculation of the group V B metals
V, Nb and Ta using SC APW method is reported by Boyer et al.
[18] who found that the band structure of V is very
sensitive to the exchange approximation used.

Recently the band structure of V, Nb and Ta has been
calculated by Alward et al. [19] using empirical pseudopoten-
tial method. These authors compared the theoretical reflecti-
vity data, density of states and Fermi surface topology with
experimental results and found a general agreement.

There are three band structure calculations of the
electron momentum distributions (EMD) in V. Besides the
work of Wakoh and Yamashita [16,17] mentioned earlier,
Laurent et al. [20] have used a self-consistent LCGO method
to calculate the Compton profile of V and other paramagnetic
3d metals. A calculation by Kanhere and Singru [21] gives
the systematics of the EMD in 3d metals including V.

Recently Wakoh and Kubo [22] have calculated the
X-ray form factors by the APW method. They have estimated
the charge asphericity in V by using the ratios of the
integrated intensities of X-ray scattering for reflection
pairs. They find that the state-dependent potential constru-
cted by them for V (and which was fitted to the FS data)
gives a closer agreement with the X-ray form factor data

than the state-independent potential [23].

It is clear from above that several authors have calculated band structure and other electronic properties of V. Although we have not discussed each of these calculations in detail, we shall refer to their important conclusions in the next section as well as in Chapters 4 and 5. However, the results of the different band structure calculations reveal the following significant factors which determine the band structure of V : (i) The relative population of the (3$\underline{d}$) and (4$\underline{s}$) electrons assumed in the calculation, (ii) the exchange parameter, α, used, (iii) whether the calculation was performed in a non-self-consistent or self-consistent manner and (iv) the band structure method used.

2.3 Review of Experimental Studies of the Fermi Surface of Vanadium

The progress in the experimental study of the Fermi surface of vanadium is limited due to the difficulty in obtaining pure vanadium samples. The literature, therefore, contains somewhat fewer number of reports on experimental study as compared to the theoretical calculations.

The earliest report on the experimental study was by Alekseevskii and Egorov [24] who carried out magnetoresistance measurements on V and observed an anisotropy in the FS of V. Later on Phillips [11] used the technique of impulsive fields to study the FS of V in the {100} plane. This was followed by an extensive work by Parker and
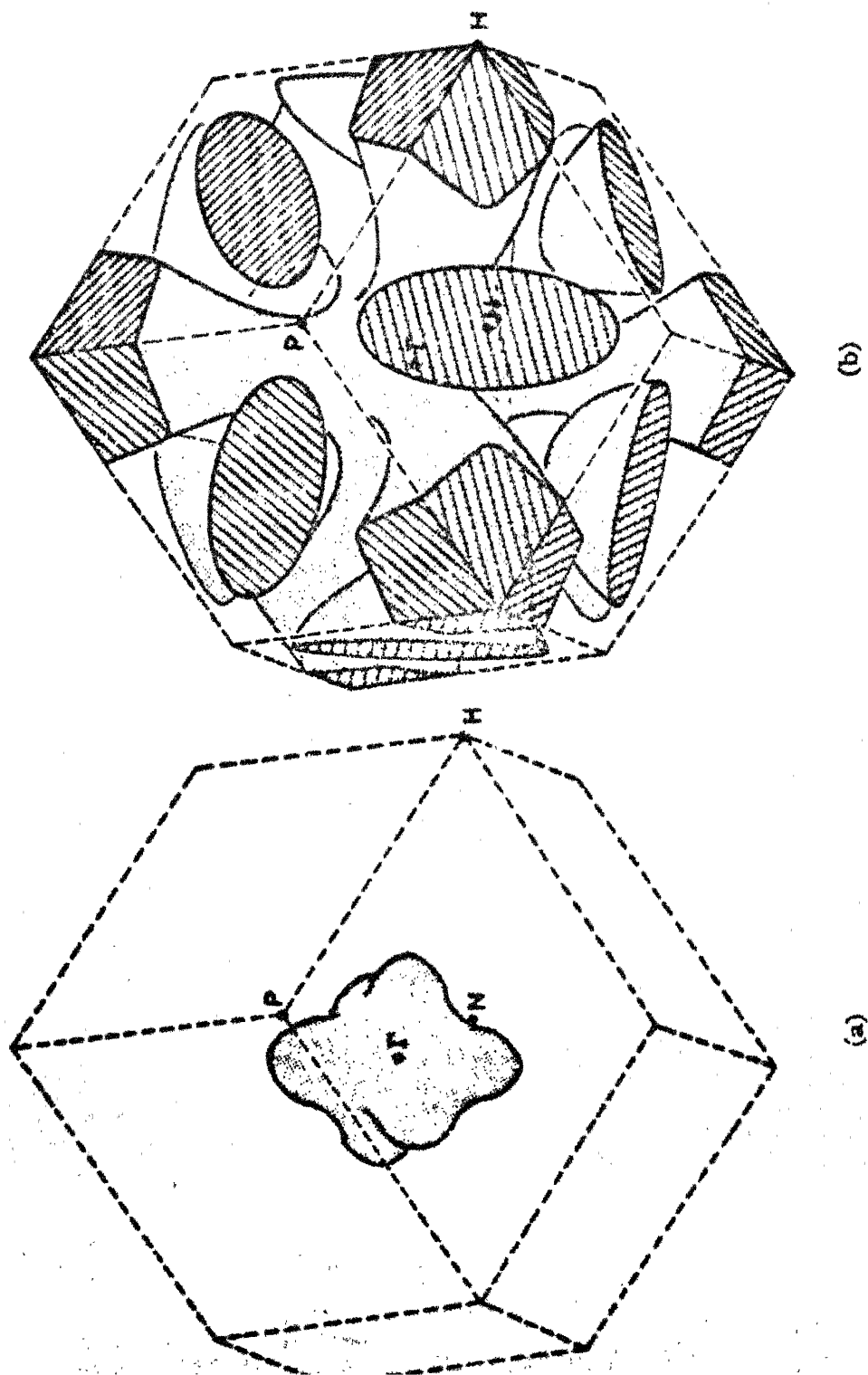
Fig. 2.1: General features of the Fermi surface of vanadium (a) second band octahedral hole surface (b) third band hole surface (~centered ellipsoids and jungle-gym arms).

(a)

(b)
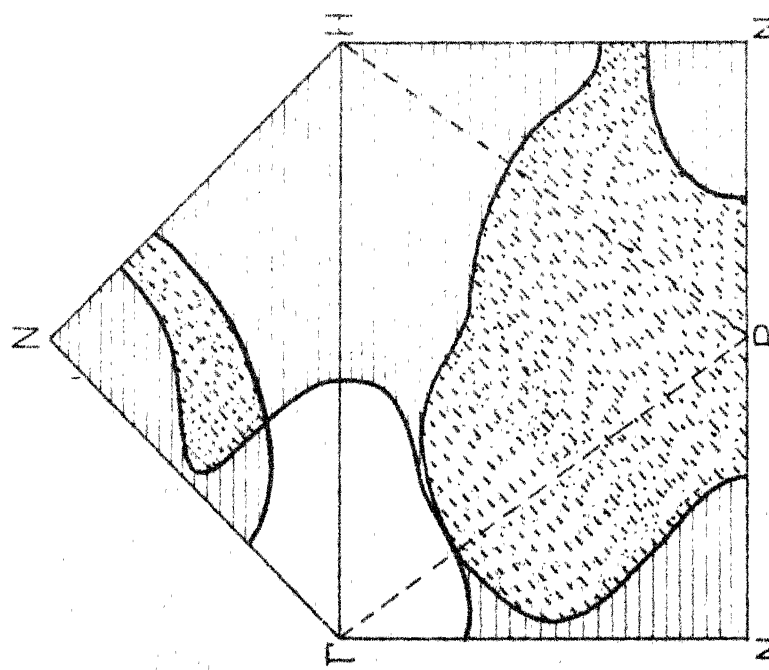
(a)
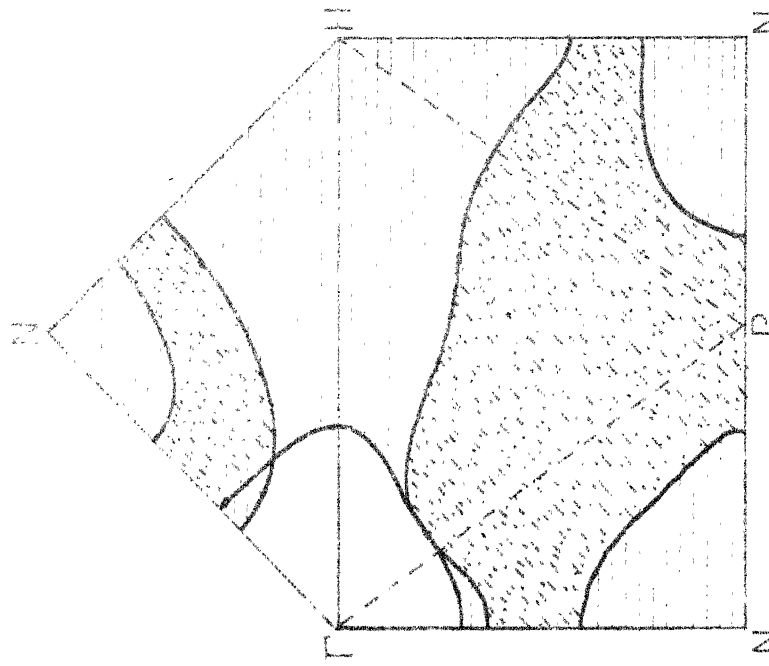
(b)

Fig. 2.2: Fermi surface of the vanadium group of metals predicted by Mattheiss [7] from (a) calculations on iron by _____ and (b) calculations for tungsten.

Halloran [25] who used the magnetothermal oscillation technique to study the FS of V in the {100} and {110} planes. These authors also compared their measurements with other experimental and theoretical results.

General features of the FS topology for V, as supported by different studies, are as shown in Fig. 2.1. We have also shown in Fig. 2.2 the cross section of the FS of V in the central planes {100} and {110} as calculated by Mattheiss based on (a) energy bands of tungsten and (b) energy bands of iron.

The Γ-centered octahedral hole surface arising out of the second band is shown in Fig. 2.1 (a). The hole surface arising out of the third band is rather complicated and consists of multiply connected hole tubes along the <100> direction (commonly known as the jungle-gym-arms) as well as large distorted half-ellipsoids centered at N (Fig. 2.1(b). The estimate of the dimensions of these N-centered half-ellipsoids is obtained from the measurements of Parker and Halloran [25] who reported the values of the semiaxes along N-P, N-Γ and N-H as 4.632, 4.405 and 3.649 nm^{-1} respectively. Although the measured areas of these half-ellipsoids [24,25] show a good agreement among themselves they appear to be higher than the theoretical values calculated by the APW method [13]. The experimental ratio of the semiaxes N-Γ/N-P, N-Γ/N-H for V as reported by Parker and Halloran [25] are 0.946 and 1.21 respectively. In a similar way the

measured values of the effective mass (m^{*}/m) determined from the de Haas-van Alphen experiments [25] are found to be higher than those calculated theoretically [13,18].

There is a major point of controversy about the FS topology of V. According to the model FS of V obtained by Mattheiss [7] by using the energy bands of Fe, the N-centered ellipsoids are connected to the jungle-gym arms by narrow necks extending along the Γ-N direction. Although the experimental data by Parker and Halloran [24] admit the possibility of such necks, these authors were not able to confirm their existence. In terms of the band structure of V, the existence of such necks would require that the third band along the Σ direction in V should not cross the Fermi level but should lie above it. Theoretical calculation of the band structure of V by different methods [13,15,18,20] report that the third band along the Σ direction dips below the Fermi level by **few** mRy. In view of this small 'dipping' it is difficult to categorically confirm or deny the existence of these necks because the location of the energy bands near the FS is usually known within few milliRydbergs only. Alward et al. [19], for example, put an upper limit on the external diameter of these necks as $\frac{1}{25}(2\pi/a)$ if they exist. In Chapter 4 we shall discuss in detail the effect of these necks on the 2D-angular correlation of positron annihilation radiation.

2.4 Survey of the Compton Scattering and Positron Annihilation in V

There have been several experimental and theoretical studies of Compton scattering in vanadium. Weiss and DeMarco [26] used the e_g/t_{2g} population ratio, obtained from the x-diffraction paired reflections from V, to calculate the directional Compton profiles of V. These authors found a 8 % directional anisotropy in the Compton profiles J_{100} (q = 0) and J_{111} (q = 0). However the experimental anisotropy measured by other workers [27-29] was found to be small.

A detailed band structure calculation of the directional Compton profiles of V was carried out by Wakoh and Yamashita [16] using the KKR method and a state-dependent potential [15]. Their theoretical results showed a fair agreement with the experimental profiles measured by Terasaki et al. [28]. In a subsequent work Wakoh et al. [30] repeated their calculations using an APW method and obtained results which were qualitatively same as before. Recently Itoh et al. [31] have measured the directional Compton profiles for V and $VD_{0.68}$ single crystals. Their measured data for V agree well with the theoretical calculations of Wakoh et al. [30].

The angular correlation of positron annihilation radiation (ACPAR) in V has been measured by Shiotani et al. [32] and by Hasegawa et al. [33] using the long-slit

geometry. Experimental data from both these measurements showed a satisfactory agreement with the theoretical calculations of Wakoh et al. [17].

A prominent feature about the experimentally observed directional Compton profiles [27-29] as well as the directional ACPAR curves [32,33] from V is the existence of fine structure which can be understood in terms of the FS topology [17,30]. For example the Compton profiles as well as the ACPAR curves along the [100] direction show a dip or concavity at low momenta near p = 0. This structure has been ascribed to the closed hole pockets at point N and the multiply connected jungle-gym arms of the third band FS. Measurements made on $VD_{0.68}$ indicate that introduction of deuterium fill up the hole bands of V and the Compton profiles [31] and the ACPAR curves [33] for $VD_{0.68}$ show a disappearance of the fine structure (dip or concavity) in the [100] direction.

These results clearly indicate that the electron momentum distribution in V is sensitive to the FS topology and that these effects can be probed by measuring the Compton profiles and ACPAR curves for single crystal specimens. It was pointed out that the 2D-ACPAR measurements can examine such effects in greater detail and can provide a wealth of information about the FS topology. In the present work we have, therefore, attempted to understand the effects of band structure and FS topology on the 2D-ACPAR curves in V and VD_x.

REFERENCES

1. J.M. Ziman, Solid State Physics, ed. H. Ehrenreich,
    F. Seitz and D. Turnbull, Vol. 26, Academic Press,
    New York (1976), p.1.

2. G.C. Fletcher, The Electron Band Theory of Solids,
    North-Holland Publishing Co., Amsterdam (1971).

3. J. Callaway, Quantum Theory of the Solid State,
    Part A and B, Academic Press, New York (1974).

4. C.M. Quinn, An Introduction to Quantum Chemistry of
    Solids, Clarendon Press, Oxford (1973).

5. L. Pincherle, Electronic Energy Bands in Solids, McDonald,
    London (1971).

6. L.F. Mattheiss, Phys. Rev. 134, A970 (1964).

7. L.F. Mattheiss, Phys. Rev. 139, A1893 (1965).

8. E.C. Snow and J.T. Waber, Acta Metall. 17, 623 (1969).

9. J.R. Anderson, J.W. McCaffrey and D.A. Papaconstantopoulos,
    Solid St. Commun. 7, 1439 (1969).

10. D.W. Eastman, Solid St. Commun. 7, 16 (1969).

11. R.A. Phillips, Phys. Lett. A36, 361 (1971).

12. M. Yasui, E. Hayashi and M. Shimizu, J. Phys. Soc.
    Jpn. 29, 1446 (1970).

13. D.A. Papaconstantopoulos, J.R. Anderson and J.W. McCaffrey,
    Phys. Rev. B5, 1214 (1972).

14. T.M. Hattox, J.B. Conklin, J.C. Slater and S.B. Trickey,
    J. Phys. Chem. Solids 34, 1627 (1973).

15. S. Wakoh and J. Yamashita, J. Phys. Soc. Jpn. 35, 1394
    (1973).

16. S. Wakoh and J. Yamashita, J. Phys. Soc. Jpn. 35, 1406
    (1973).

17. S. Wakoh, Y. Kubo and J. Yamashita, J. Phys. Soc. Jpn.
    38, 416 (1975).

18. L.L. Boyer, D.A. Papaconstantopoulos and B.M. Klein, Phys. Rev. B15, 3685 (1977).

19. J.F. Alward, C.Y. Fong and C. Guha Sridhar, Phys. Rev. B18, 5438 (1978).

20. D. Laurent, C.S. Wang and J. Callaway, Phys. Rev. B17, 455 (1978).

21. D.G. Kanhere and R.M. Singru, J. Phys. F7, 2603 (1977).

22. S. Wakoh and Y. Kubo, J. Phys. F10, 2707 (1980).

23. P.E. Mijnarends, Construction of a Muffin-tin Potential for Metallic Vanadium, Report RCN-76-010, Reactor Centrum Nederland, Petten (N.H.) The Netherlands (Unpublished) (1976).

24. N.E. Alekseevskii and V.S. Egorov, Jh. Eksp. Teor. Fiz. Pis'ma Red 1, 141 (1965) [JETP Letters 1, 141 (1965)].

25. R.D. Parker and M.H. Halloran, Phys. Rev. B9, 4130 (1974).

26. R.J. Weiss and J.J. DeMarco, Phys. Rev. 140A, 1223 (1965).

27. W.C. Phillips, Phys. Rev. B7, 1047 (1973).

28. O. Terasaki, T. Fukamachi, S. Hosoya and D. Watanabe, Phys. Lett. 43A, 123 (1973).

29. T. Paakkari, S. Manninen, O. Inkinen and E. Liukkonen, Phys. Rev. B6, 351 (1972).

30. S. Wakoh, Y. Kubo and J. Yamashita, J. Phys. Soc. Jpn. 40, 1043 (1976).

31. F. Itoh, T. Honda, H. Asano, M. Hirabayashi and K. Suzuki, J. Phys. Soc. Jpn. 49, 202 (1980).

32. N. Shiotani, T. Okada, T. Mizoguchi and H. Sekizawa, J. Phys. Soc. Jpn. 38, 423 (1975).

33. M. Hasegawa, S. Koike, M. Hirabayashi, H. Asano and T. Suzuki, J. Phys. Soc. Jpn. 46, 481 (1979).

The occupation number $f(\vec{k}, j)$ is identical to the Fermi-Dirac distribution and is zero for the empty state and is unity for the occupied state (at T = 0 K) of the electron. It may be pointed out that the positron wavefunction is calculated for the state $\vec{k}_+ = 0$ in its lowest energy band since it is thermalized before annihilation.

The electron wavefunction can be obtained by solving the Schrödinger equation[*]

$$[- \nabla^2 + V(\vec{r}) - E(\vec{k})] \ \psi_{\vec{k}}(\vec{r}) \ = \ 0 \tag{3.3}$$

in the independent particle approximation using the standard methods. Although many such methods for solving the band structure problem are available [2-6], previous calculations of the 2D-ACPAR in metals have used the OPW method for Al [7], the APW method for Cu [8] and the Hubbard-Mijnarends approximate method for Cu [9] and Fe [10]. In practice the calculation of the 2D-ACPAR curve $N(p_y, p_z)$ along a particular set of $\{p_y, p_z\}$ direction requires computation of the TPMD, $\rho(\vec{p})$, at about 500 $\vec{p}$-points in a plane.

This makes the computing time and computer memory a serious consideration. The method due to Hubbard and Mijnarends [11,12] provides a fast but approximate scheme for such calculations and it has provided satisfactory description of the ACPAR data in transition metals [9,13,14].

---

[*]We shall follow the **mixed** system of atomic units in which $\hbar = 1$, $m = 1$, $e = 1$, while the energies are expressed in Rydbergs.

These considerations along with the fact that these computer programs were available in our group guided us to use the Hubbard-Mijnarends fast approximate scheme to calculate the TPMD in V. In the next section we shall outline the essential steps involved in this method. The detailed discussion of this method is given by Hubbard [11], Hubbard and Mijnarends [1,12] and Harthoorn [15].

3.2 The Fast Approximate Method due to Hubbard for the Calculation of Electron Band Structure

It was pointed out earlier that the electron band structure, wavefunction and the momentum distribution in a crystalline solid can be obtained by solving Schrödinger equation (3.3). A number of methods have been developed to achieve this [2-6]. The problem assumes a special character when we are interested in the electronic structure of transition metals. The electron band structure of transition metals can be described as hybrids of nearly-free-electron (NFE) like bands with narrow d-bands of tight binding nature. A convenient approximate scheme using this approach and based on the Korringa [16] and Kohn and Rostoker [17] and Ziman [6,18] method for the calculation of the band structure is given by Hubbard [11]. In the Korringa-Kohn-Rostoker (or KKR) method which is based on the Green's function method, the crystal potential is usually assumed to be of the muffin-tin type i.e. spherically symmetric inside the inscribed sphere of the cell and constant within the

interstitial region. The band structure is determined using energy-dependent phase shifts which arise from the scattering of the electrons from muffin-tin potential.

In the KKR formulation by Ziman [18] the secular determinantal equation is given by the equation

$$\sum_{n'} [(k_n^2 - \varepsilon) \delta_{nn'} + \Gamma_{nn'}] B_{n'} = 0 \qquad (3.4)$$

where $k_n = |\vec{k}_n| = |\vec{k} + \vec{K}_n|$, $\vec{K}_n$ being the reciprocal lattice vectors and ε is the Bloch energy eigenvalue for the electron in a state $\vec{k}$. For the case where the potential term Γ is small, eq. (3.4) can be solved using only a relatively small number of plane waves. Lloyd [19] introduced the concept of $\Gamma_{nn'}$, the matrix elements of the small pseudopotential which has the same scattering properties as the original lattice potential. He also introduced a pseudo-wavefunction $\psi_{ps}(\vec{r})$ which can be expanded in terms of the coefficients B_n in the following manner

$$\psi_{ps}(\vec{r}) = (1/\tau)^{1/2} \sum_{n} B_n \exp(i \vec{K}_n \cdot \vec{r}) \qquad (3.5a)$$

throughout the atomic polyhedron and

$$\psi_{ps}(\vec{r}) = \psi_{\vec{k}}(\vec{r}) \qquad (3.5b)$$

in the region between the boundaries of the atomic polyhedron (volume τ) and its inscribed sphere.

Following Slater [20], the matrix elements $\Gamma_{nn'}$ of the pseudopotential can be expressed as

$$\Gamma_{nn'} = (4\pi/\tau) \sum_{\ell} (2\ell+1) r_\ell^2 \gamma_\ell(r_\ell) j_\ell(k_n r_\ell) j_\ell(k_{n'} r_\ell) P_\ell(\cos\theta_{nn'})$$

$$\ldots\ldots (3.6)$$

where

$$\gamma_\ell(r_\ell) = -\frac{\tan\eta_\ell}{k\, r_\ell^2\, j_\ell(k\, r_\ell)\, \{j_\ell(k\, r_\ell) - (\tan\eta_\ell)\, n_\ell(k\, r_\ell)\}} \qquad (3.7)$$

In the above $k = \sqrt{\varepsilon}$, η_ℓ is the phase shift of the $\underline{\ell\text{th}}$ partial wave scattering from the atomic potential, $\theta_{nn'}$ is the angle between $\vec{k}_n$ and $\vec{k}_{n'}$ while r_ℓ can be chosen arbitrarily within the interval $r = 0$, $r = r_i$ = the radius of the inscribed sphere of the atomic polyhedron. Other functions in (3.6) and (3.7) are as follows : $P_\ell(\cos\theta)$ the Legendre polynomial, j_ℓ and n_ℓ the spherical Bessel and Neumann functions respectively.

The quantity γ_ℓ and therefore $\Gamma_{nn'}$ will be small except the case when $j_\ell(k\, r_\ell)$ or $[j_\ell(k\, r_\ell) - (\tan\eta_\ell)\, n_\ell(k\, r_\ell)]$ is close to zero for some value of ℓ. To avoid this situation Pendry and Capart [21] suggested that r_ℓ can be chosen at the zero of $n_\ell(k r_\ell)$ provided that there is a zero in the interval $(0, r_i)$, otherwise $r_\ell = r_i$. The case when r_ℓ is different from r_i will arise only when $\ell = 0$.

It has been shown by Hubbard [11,22] that in the case of transition metals a d-resonance occurs when η_2 passes through $\pi/2$, rising rapidly from 0 to π within a narrow energy range at low energies and hence there is no way for r_2 to prevent the appearance of a corresponding singularity in

the denominator of γ_2. Following the rule by Pendry and Capart, γ_2 will be small except near the resonance in tan η_2. Assuming that only one resonance occurs for $\ell = \lambda$ (λ being equal to 2 for transition metals) at $k^2 = \varepsilon_0$ one can write [11]

$$\gamma_\ell = \gamma_\ell' - \frac{\delta_{\ell\lambda} W}{\varepsilon_0 - k^2} \tag{3.8}$$

where W is the width of resonance and γ_ℓ' is the residue which is always small.

Ziman's determinantal equation can now be written as

$$\begin{pmatrix} K + V - \varepsilon I & h \\ h^* & (\varepsilon_0 - \varepsilon) I \end{pmatrix} \begin{pmatrix} B \\ a \end{pmatrix} = 0 \tag{3.9}$$

where the matrix elements of the various submatrices are written as

$$K_{nn'} = k_n^2 \delta_{nn'} \tag{3.10a}$$

$$V_{nn'} = \frac{4\pi}{\tau} \sum_\ell (2\ell+1) r_\ell^2 \gamma_\ell' j_\ell(k_n r_\ell) j_\ell(k_{n'} r_\ell) P_\ell(\cos \theta_{nn'})$$
$$\cdots\cdots \tag{3.10b}$$

$$h_{nm} = -4\pi r_\lambda \left(\frac{W}{\tau}\right)^{1/2} j_\lambda(k_n r_\lambda) Y_{\lambda m}(\hat{k}_n) \tag{3.10c}$$

and

$$a_m = \frac{4\pi r_\lambda}{\varepsilon_0 - \varepsilon} \left(\frac{W}{\tau}\right)^{1/2} \sum_n j_\lambda(k_n r_\lambda) Y_{\lambda m}^*(\hat{k}_n) B_n \tag{3.10d}$$

with $m = -\lambda, -\lambda+1, \ldots\ldots, \lambda$

The column matrix a and B in the eq. (3.9) describe the resonant and non-resonant part of wavefunctions respectively

Following the procedure of Heine [23] Hubbard was able
to reduce eq. (3.9) to an equation of lower order. In this
procedure various vectors $\vec{k}_n$ are divided into two sets: (i) a
'preferred' set P and (ii) a 'remainder' set R. The vectors
in the set 'P' are chosen so that for the vectors in set 'R'
not included in set 'P' the quantity $(\varepsilon - k_n^2)$ never becomes
small in the energy range of interest. As a result only a
few of the smallest reciprocal lattice vectors will be
included in the set 'P'.

This partitioning of the $\vec{k}_n$ results in further simpli-
fication of the problem. The matrix elements of V_{PR} and
V_{RP} are also small because γ'_ℓ is small. Using the approxi-
mation $V_{PR} = V_{RP} = 0$ and neglecting V_{RR} in comparison
with $(k_n^{2(R)} - \varepsilon)$ we can rewrite eq. (3.9) in two parts as
follows

$$\begin{pmatrix} K_P + V_{PP} - \varepsilon I & h_P \\ h_P^* & A - \varepsilon I \end{pmatrix} \begin{pmatrix} B_P \\ a \end{pmatrix} = 0 \tag{3.11a}$$

and

$$(K_R - \varepsilon I) B_R + h_R a = 0 \tag{3.11b}$$

where the matrix elements of the square matrix A are given
by

$$A_{mm'} = \varepsilon_0 \delta_{mm'} - \frac{(4\pi)^2}{\tau} r_\lambda^2 W \sum_n^{(R)} \frac{j_\lambda^2 (k_n r_\lambda)}{k_n^2 - \varepsilon} Y_{\lambda m} (\hat{k}_n) Y_{\lambda m'}^* (\hat{k}_n)$$

$$\ldots \ldots (3.12)$$

with the sum $\sum_n^{(R)}$ being carried out over all vectors of the remainder set 'R'. Hubbard [11] has given the following prescription to calculate the above sum $\sum_n^{(R)}$. One writes

$$\Sigma^{(R)} = \Sigma^{(S)} + \frac{\delta_{mm'}}{r_\lambda \tau_k} \left[\frac{1 - \cos(2k_o r_\lambda)}{2k_o r_\lambda} + \frac{1}{2}\pi - Si(2k_o r_\lambda) \right]$$

$$\ldots\ldots (3.13)$$

Where $\Sigma^{(S)}$ is a summation similar to the second term in eq. (3.12) over a set 'S' of the vectors $\vec{k}_n$ in the first few shells of the reciprocal lattice excluding those belonging to the set 'P', Si(x) denotes the sine integral $\int_o^x (\sin t)dt/t$, τ_k is the volume of the unit cell in the reciprocal space and $N = (4\pi k_o^3/3\tau_k) =$ total number of reciprocal lattice vectors included in the set 'P' and the sum $\Sigma^{(S)}$. The determinantal equation (3.11a) is similar to the form of equation used in the model pseudo-potential scheme [23,24]. The physical significance of the various submatrices in eq. (3.11a) is as follows. The submatrix V describes the nearly-free-electron (NFE) part of the s-p conduction band while the submatrix A (5x5 in size) describes the d-bands. The off-diagonal matrices h and h^* contain the hybridization between these bands. The energy dependence of the submatrices A and V required further suitable approximation to remove the energy dependence of the matrix M in

$$\left[M(\varepsilon) - \varepsilon I \right] \left[\begin{array}{c} B_P \\ \alpha \end{array} \right] = 0 \qquad (3.14)$$

which is an equivalent form of (3.11a). The whole aim is

to reduce the problem to that of diagonalization. In Hubbard's scheme this is achieved by setting

$$\left[M(\varepsilon) - \varepsilon I \right] \simeq M_1 - \varepsilon M_2 \tag{3.15}$$

such that M_1 and M_2 are energy (ε) independent and by substituting

$$\hat{X} = \begin{pmatrix} \mathcal{B}_P \\ \mathcal{A} \end{pmatrix} \quad \text{and} \quad \mathcal{Y} = M_2^{\frac{1}{2}} \hat{X}$$

to obtain

$$\left[M_2^{-1/2} M_1 M_2^{-1/2} - \varepsilon I \right] \mathcal{Y} = 0 \tag{3.16}$$

as an equivalent form of (3.11a).

It can now be shown, by comparing eq. (3.11a) and eq. (3.16) that the actual problem to determine the band structure has now been reduced to secular form which can be solved by standard methods of matrix algebra.

In the above only a bare outline of Hubbard's method is given. A detailed description of the method is given elsewhere [11,12,15].

3.3 Calculation of Electron Wavefunctions : Hubbard-Mijnarends Method

In the preceding section we have given a brief description of the fast approximation scheme due to Hubbard for the calculation of band structure of transition metals. This scheme does not contain any adjustable parameter and is known to provide an overall accuracy of 0.005 - 0.01 Ry

[25] when compared with other methods like the APW method etc. In 1972, Hubbard and Mijnarends [12] extended this scheme to calculate the electronic wavefunctions in a form suitable for the calculation of matrix elements such as those in eq. (3.2). Using the concepts developed earlier these authors showed that the eigenvectors of eq. (3.4) contain the Fourier coefficients of a plane wave expansion of a pseudo-wavefunction.

When a muffin-tin type of crystal potential is used, the electron wavefunction $\psi_{\vec{k}}(\vec{r})$ can be expanded in two different forms in the two regions. The pseudo-wavefunction is different from the true wavefunction in the region inside the inscribed sphere. In this region the true wavefunction can be expanded in terms of spherical harmonics $Y_L(\hat{r})$ with L as the quantum number $L \equiv (\ell, m)$ together with those solutions $R_\ell(r)$ of the radial Schrödinger equation which are regular at the origin. The electron wavefunction $\psi_{\vec{k}}(\vec{r})$ within the inscribed sphere is given by

$$\psi_{\vec{k}}(\vec{r}) = \frac{4\pi}{(\tau)^{1/2}} \sum_L i^\ell \frac{R_\ell(r)}{R_\ell(r_i)} X_L Y_L(\hat{r}) \qquad (3.17)$$

In the interstitial region, the true electron wavefunction coincides with the pseudo-wavefunction and it can be expanded in terms of plane waves with B_n as coefficients

$$\psi_{\vec{k}}(\vec{r}) = (1/\tau)^{1/2} \sum_n B_n \exp[i(\vec{k}+\vec{K}_n)\cdot\vec{r}] \qquad (3.18)$$

The coefficients X_L in eq. (3.17) can be determined by requiring continuity of $\psi_{\vec{k}}(\vec{r})$ at $r = r_i$ to obtain

$$X_L = \sum_n B_n j_\ell (k_n r_i) Y_L^* (\hat{k}) \qquad (3.19)$$

The next job is to normalize the wavefunction to unity in the atomic cell. Rigorous treatment shows that the wavefunction $\psi_{\vec{k}}(\vec{r})$ will be correctly normalised if the eigenvectors $\mathcal{Y}$ in the secular equation (3.16) are correctly normalized.

Although it is necessary to use all the ℓ-values upto infinity to achieve a perfect matching at $r = r_i$, in practice one limits ℓ to ℓ_{max}, usually say $\ell_{max} = 3$. This leads to a slight discontinuity at $r = r_i$.

3.4 Calculation of Positron Wavefunction

In the independent particle model the crystal potential seen by the positron in a metal is same as that for the electrons except for the different sign. The facts that positron is thermalized before its annihilation and that the average number of positrons in the sample at any given time (with the positron beam intensities commonly used in an experiment) is of the order of one further simplify the problem to that of determining the positron wavefunction in the lowest energy state $\vec{k}_+ = 0$.

Early calculations [26] of the positron wavefunction used the Wigner–Seitz approximation of a spherical cell.

In this method the positron wavefunction $\psi_+(r) = R_+(r)/r$ is obtained by numerically integrating the radial equation

$$\frac{d^2 R_+(r)}{dr^2} + 2(E+V(r)) R_+(r) = 0 \tag{3.20}$$

and by choosing the eigenvalue to satisfy the boundary condition $d\psi_+(r)/dr = 0$ at $r = r_{WS}$, the radius of the Wigner-Seitz cell.

In view of the periodicity of lattice which is present in the positron wavefunction, it can be expanded in a Fourier series in terms of the reciprocal lattice vector [27]

$$\psi_+(\vec{r}) = (1/\tau)^{1/2} \sum_{\vec{K}} B_{\vec{K}}^+ e^{i\vec{K}\cdot\vec{r}} \tag{3.21}$$

The Fourier coefficients $V_{\vec{K}-\vec{K}'}$ of the periodic potential $V(\vec{r})$ may be found from the relation

$$V_{\vec{K}-\vec{K}'} = \frac{1}{\tau} \int V(\vec{r}) e^{i(\vec{K}-\vec{K}')\cdot\vec{r}} d\vec{r} \tag{3.22}$$

Now by substituting (3.21), (3.22) into the Schrödinger equation for positron, one obtains the secular equation as

$$\sum_{\vec{K}} \{(K^2-E) \delta_{\vec{K},\vec{K}'} + V_{\vec{K},\vec{K}'}\} B_{\vec{K}}^+ = 0 \tag{3.23}$$

This equation is easily solvable after symmetrization.

The Fourier coefficients are adjusted following Gould et al. [27] so that $\psi_+(\vec{r} = 0) = 0$ subject to the normalization condition

$$\sum_{\vec{K}} |B_{\vec{K}}^+|^2 = 1 \tag{3.24}$$

The computational details for the calculation of positron wavefunction in the case of bcc metallic vanadium is given in Chapter 4. The positron wavefunction along the three crystal directions, i.e. <100>, <110>, and <111> can be calculated using the Fourier coefficients. The calculation of positron wavefunction along the three symmetry directions offer the advantage of calculating the spherically averaged wavefunction R_+/r, by using the expression due to Houston [28].

$$\frac{R_+(r)}{r} = \frac{1}{35} \{10 \ \psi_{100}(\vec{r}) + 16 \ \psi_{110}(\vec{r}) + 9 \ \psi_{111}(\vec{r})\}$$

$$\ldots\ldots (3.25)$$

This spherically averaged positron wavefunction was used in the calculation of the two-photon momentum distribution.

3.5 Many-body Effects

In the above discussion we have ignored the positron-electron ($e^+ - e^-$) and electron-electron ($e^- - e^-$) correlation effects and have considered the positron annihilation in the independent particle model. In reality there is a pile-up of electron cloud at the positron due to the Coulomb attraction thus raising the electron density at the positron site and enhancing the annihilation rate. Although these effects are significant for the positron lifetimes, they can be ignored for the angular correlations [1]. Nevertheless the enhancement of the TPMD arising out of the $e^+ - e^-$ interaction

can be included in the following manner suggested by Kahana [29]. One calculates the TPMD $\rho(\vec{p})$ on the basis of an independent particle model (IPM) and multiplies it by an enhancement factor $\varepsilon(p)$ so that

$$\rho(\vec{p})_{\text{enh.}} = \varepsilon(p) \; \rho(\vec{p}) \tag{3.26a}$$

where

$$\varepsilon(p) = a + b \, \gamma^2 + c \, \gamma^4$$

and

$$\gamma = p/p_F \leq 1 \tag{3.26b}$$

and the constants a, b and c depend on the electron density [29]. Recently Mijnarends and Singru [9] have proposed an energy-dependent form of 'Kahana enhancement' which provides an excellent agreement between the theory and experiment for Cu.

In the present work we have limited ourselves to the calculation of the TPMD $\rho(\vec{p})$ in the independent particle model only. Any correction to $\rho(\vec{p})$ for the enhancement can be made by a suitable formula later on when a comparison between theory and experiment is desired.

3.6 Calculation of the Two-photon Momentum Distribution

As discussed in Sec. 3.1 it is necessary to evaluate the overlap integral $A_j(\vec{k},\vec{p})$ given by eq. (3.2). To do so the atomic cell is split up in two regions : (i) the inscribed sphere and (ii) the interstitial region, i.e. the remaining part of the Wigner-Seitz cell. For the integration in the

inscribed sphere, the equation (3.17) is substituted for electron wavefunction and spherically averaged positron wavefunction given by eq. (3.25) is used, while the product term $\exp(-i\vec{p}.\vec{r})$ is expanded in partial waves. The integration outside the inscribed sphere is performed using the electron wavefunction and positron wavefunction expanded in plane waves according to (3.18) and (3.21) respectively. The integration of this double series over the full Wigner-Seitz cell then yields a double sum of δ-function. The integral of the plane wave expansion over the inscribed sphere must be subtracted from the last integral performed over both the regions. The final expression is

$$A_j(\vec{k},\vec{p}) = \sum_{n,n'} B_n B_{n'}^+ \left[\delta(\vec{k}_n + \vec{K}_{n'}, -\vec{p}) - \frac{4\pi r_i^2}{\tau} \frac{j_\ell(|\vec{k}_n + \vec{K}_{n'} - \vec{p}|r_i)}{|\vec{k}_n + \vec{K}_{n'} - \vec{p}|} \right]$$

$$+ \frac{4\pi^2}{(\tau)^{1/2}} \sum_L \frac{X_{L,j}}{R_{Lj}(r_i)} Y_L(\vec{p}) \int_0^{r_i} j_\ell(pr) R_{Lj}(r) R_+(r) \, r \, dr$$

$$\ldots\ldots (3.27)$$

which formed the basis of our calculation. Some other computational details of our calculation are given in the next Chapter.

REFERENCES

1. P.E. Mijnarends in _Positrons in Solids_, ed. P. Hautojärvi, Springer-Verlag, Berlin (1979), p. 25.

2. G.C. Fletcher, _The Electron Band Theory of Solids_, North-Holland Publishing Co. Amsterdam – London,(1971).

3. J. Callaway, _Quantum Theory of the Solid State_, Part A and B, Academic Press, New York (1974).

4. C.M. Quinn, _An Introduction to the Quantum Chemistry of Solids_, Clarendon Press, Oxford (1973).

5. L. Pincherle, _Electronic Energy Bands in Solids_, MacDonald, London (1971).

6. J.M. Ziman, _Solid State Physics_, ed. H. Ehrenreich, F. Seitz and D. Turnbull, Vol. 26, Academic Press, New York (1976), p. 1.

7. J. Mader, S. Berko, H. Krakauer and A. Bansil, Phys. Rev. Lett. _37_, 1232 (1976).

8. S. Wakoh, S. Berko, M. Haghhooie and J.J. Mader, J. Phys. _F9_, L231 (1979).

9. P.E. Mijnarends and R.M. Singru, Phys. Rev. _B19_, 6038 (1979).

10. P.E. Mijnarends,Abstract B-11, Fourth International Conference on Positron Annihilation, Helsingør, Denmark, August 23-26 (1976).

11. J. Hubbard, J. Phys. C_2_, 1222 (1969).

12. J. Hubbard and P.E. Mijnarends, J. Phys. C_5_, 2323 (1972).

13. P.E. Mijnarends, Physica _63_, 235 (1973); Physica _63_, 248 (1973).

14. R.M. Singru and P.E. Mijnarends, Phys. Rev. B_9_, 2372 (1974).

15. R. Harthoorn, Ph.D. Thesis, University of Amsterdam, The Netherlands (Unpublished) (1977).

16. J. Korringa, Physica _13_, 392 (1947).

17.   W. Kohn and N. Rostoker, Phys. Rev. $\underline{94}$, 1111 (1954).

18.   J.M. Ziman, Proc. Phys. Soc. $\underline{86}$, 337 (1965).

19.   P. Lloyd, Proc. Phys. Soc. $\underline{86}$, 825 (1965).

20.   J.C. Slater, Phys. Rev. $\underline{145}$, 599 (1966).

21.   J.B. Pendry and G. Capart, J. Phys. C$\underline{2}$, 841 (1969).

22.   N.W. Dalton, J. Phys. C$\underline{3}$, 1912 (1972); J. Hubbard and
      N.W. Dalton, J. Phys. C$\underline{1}$, 1637 (1968); J. Hubbard, Proc.
      Phys. Soc. $\underline{92}$, 921 (1967).

23.   V. Heine, Phys. Rev. $\underline{153}$, 673 (1967).

24.   L. Hodges, H. Ehrenreich and N.D. Lang, Phys. Rev. $\underline{152}$,
      505 (1966); D.G. Pettifors, J. Phys. C$\underline{5}$, 97 (1972).

25.   G.C. Fletcher and B.A. Wadel, Int. J. of Quantum
      Chemistry Symp. $\underline{7}$, 619 (1973).

26.   S. Berko and J.S. Plaskett, Phys. Rev. $\underline{112}$, 1877 (1958).

27.   A.G. Gould, R.N. West and B.G. Hogg, Can. J. Phys. $\underline{50}$,
      2294 (1972).

28.   D.D. Betts, A.B. Bhatia and M. Klyman, Phys. Rev. $\underline{104}$,
      37 (1956).

29.   S. Kahana, Phys. Rev. $\underline{117}$, 123 (1960); Phys. Rev. $\underline{129}$,
      1622 (1963).

TWO-PHOTON MOMENTUM DISTRIBUTIONS AND 2D-ACPAR CURVES
IN V: RESULTS[*] AND DISCUSSION

4.1 Introduction

In the present Chapter the results of our calculations
for the electron band structure, Fermi surface (FS), positron
wavefunction, two-photon momentum distribution (TPMD) and
two-dimensional angular correlation of positron annihilation
radiation (2D-ACPAR) in vanadium will be presented and
discussed. As explained in the previous chapter the starting
point of our calculation is the choice of the muffin-tin
crystal potential for vanadium. We have used the crystal
potential prepared by Mijnarends [1] for the Special Project
sponsored by the Special Commission on Electron Charge, Spin
and Momentum Density of the International Union of Crystallo-
graphy. This muffin-tin potential was constructed with the
help of neutral-free-atom charge densities for the $3\underline{d}^3\ 4\underline{s}^2$
configuration obtained from a relativistic calculation. The
Gaspar-Kohn-Sham exchange potential with $\alpha = 2/3$ was used
while the charge densities of atoms upto the 13th nearest
neighbours were superimposed with the help of the Löwdin

---

[*]The preliminary results of this work were reported at the
Fifth International Conference on Positron Annihilation,
Lake Yamanaka, Japan, April 8-11, 1979. The earlier work
had used constant positron wavefunction. The present work,
however, uses a realistic positron wavefunction in V.

Table 4.1. Numerical constants used for the crystal
potential for metallic vanadium.

Parameter	Value
Lattice constant[*]	$a = 5.74509$ a.u.
Radius[*]of the inscribed sphere	$r_i = 2.48770$ a.u.
Constant potential[*] between the muffin-tin spheres	$V_o = -1.7106$ Ry
Fermi energy with respect to the zero of the muffin-tin potential	$E_F = 0.746$ Ry
Mean d-band energy (the energy at which tan η, goes through resonance)	$\varepsilon_d = 0.839$ Ry
Width of the resonance	$W = 0.211$ Ry

[*]Taken from Mijnarends [1].

Table 4.2.   The normalised muffin-tin potential [1]
(r V(r)/2Z) at some selected values of r.

Sl. No.	r in a.u.	r V(r)/2Z
1	0.00000	1.00000
2	0.00194	0.99333
3	0.00389	0.98659
4	0.00778	0.97297
5	0.01167	0.95940
6	0.01945	0.93283
7	0.02724	0.90743
8	0.04280	0.86063
9	0.05837	0.81859
10	0.08950	0.74545
11	0.12063	0.68374
12	0.18289	0.58433
13	0.24516	0.50756
14	0.36968	0.39711
15	0.49421	0.31822
16	0.74326	0.21103
17	0.99231	0.14012
18	1.49042	0.06129
19	1.98853	0.02303
20	2.98474	0.00132

alpha expansion. The potential was not made self-consistent. The parameters used in our calculation are given in Table 4.1 while the numerical values of the normalized potential are given in Table 4.2.

4.2 Band Structure and Bandwidths

Using Hubbard's approximation scheme described in the previous chapter energy band-values $E(\vec{k})$ for 91 $\vec{k}$-points in the 1/48th part of the Brillouin zone (BZ) (Figs. 4.1 and 4.2) were calculated. Kaga [2] has pointed out the effect of the number (N_p) of plane waves (the so-called 'preferred' set used to describe the nearly-free-electron part of the pseudopotential in Sec. 3.2) on the accuracy of Hubbard's fast approximation method [3]. Previous work [4] has shown that the effect of increasing N_p from 7 to 19 was to shift the energies by about 0.005-0.03 Ry, the maximum shift occurring for the point N_1. We therefore used $N_p = 19$ in the present calculations and these 19 'preferred' vectors are listed in Table 4.3. Terms upto $\ell = 3$ were included for describing the electron wavefunction inside the muffin-tin sphere. The band structure obtained by us along the important symmetry directions in V is shown in Fig. 4.3 while the mean d-band energy and the width of d-resonance is given in Table 4.1. The density of states histogram, is shown in Fig. 4.4 and the value of Fermi energy (E_F) obtained by us for V was $E_F = 0.746$ Ry. The electron energy eigenvalues at some
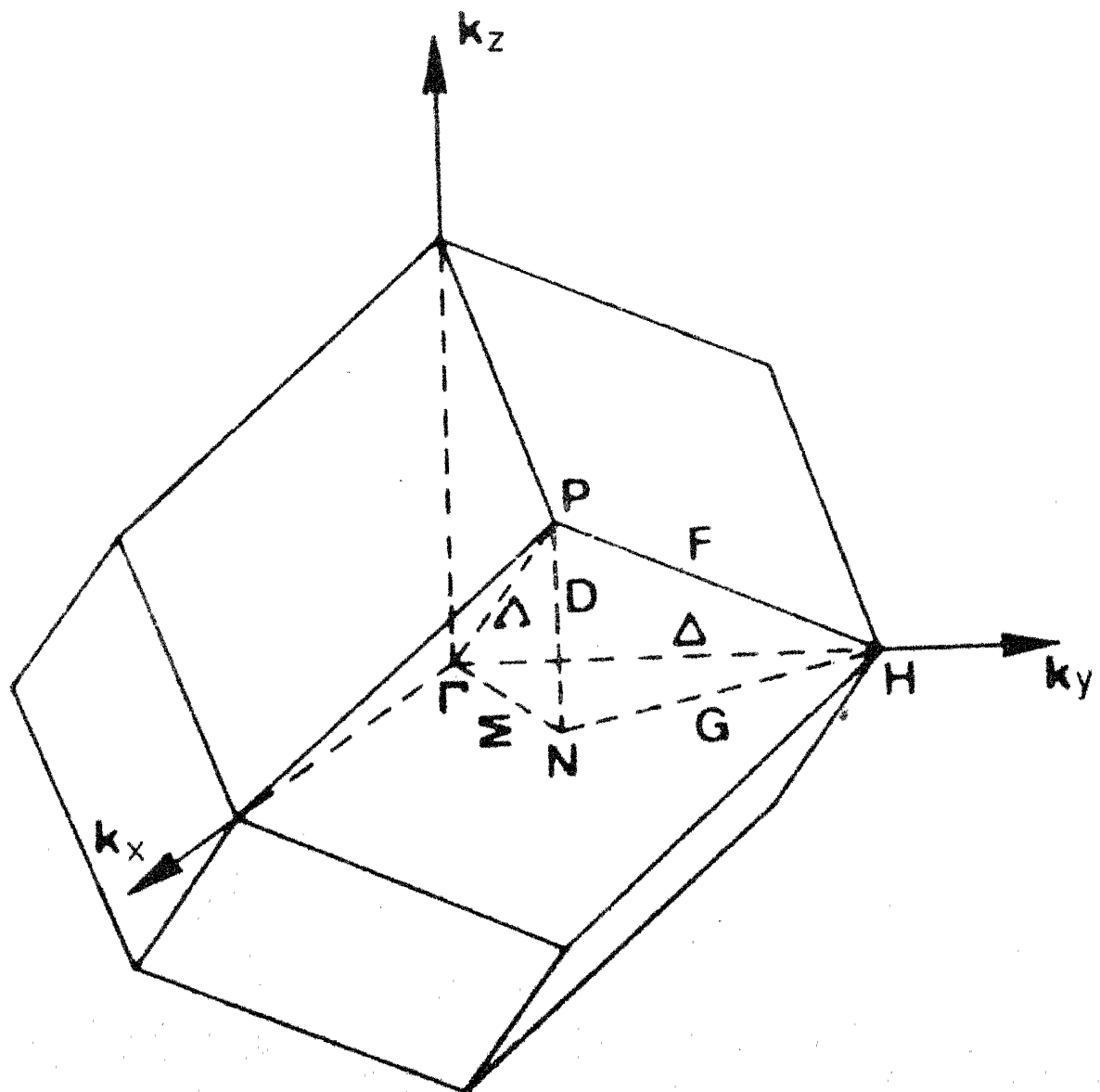
Fig. 4.1: The 1/48th part of the Brillouin zone (BZ) for vanadium.

(0,10,0)

G

Δ

Σ

N
(5,5,0)

Γ (0,0,0)

F (1,9,1)

D
(5,5,1)

Λ (1,1,1)

F (2,8,2)

D
(5,5,

Λ (2,2,2)

F (3,7,3)

D
(5,5,3)

Λ (3,3,3)

F (4,6,4)

D
(5,5,4)

Λ (4,4,4)

P
(5,5,5)
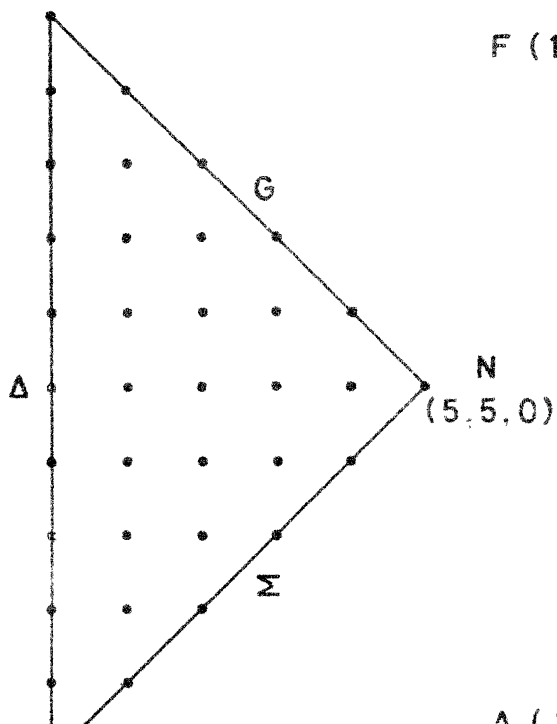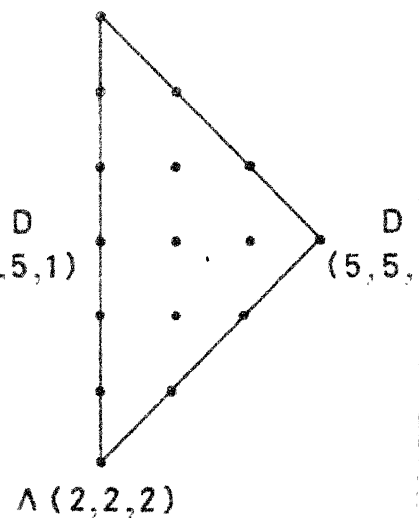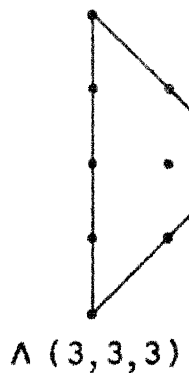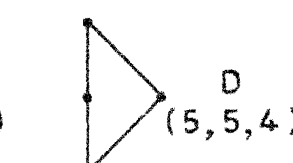
Fig. 4.2:   The 91 $\vec{k}$-points in the 1/4:tn BZ of V for which
E($\vec{k}$) values were calculated.

Table 4.3. The set of 19 preferred vectors $\vec{K_i}$ (in units of $2\pi/a$) used in our calculation.

1	(0, 0, 0)
2	(0, -1, 1)
3	(0, -1, -1)
4	(0, -2, 0)
5	(1, -1, 0)
6	(-1, -1, 0)
7	(-1, 0, -1)
8	(-1, 1, 0)
9	(1, 0, 1)
10	(1, 0, -1)
11	(-1, 0, 1)
12	(1, 1, 0)
13	(0, 1, 1)
14	(0, 1, -1)
15	(2, 0, 0)
16	(-2, 0, 0)
17	(0, 2, 0)
18	(0, 0, 2)
19	(0, 0, -2)
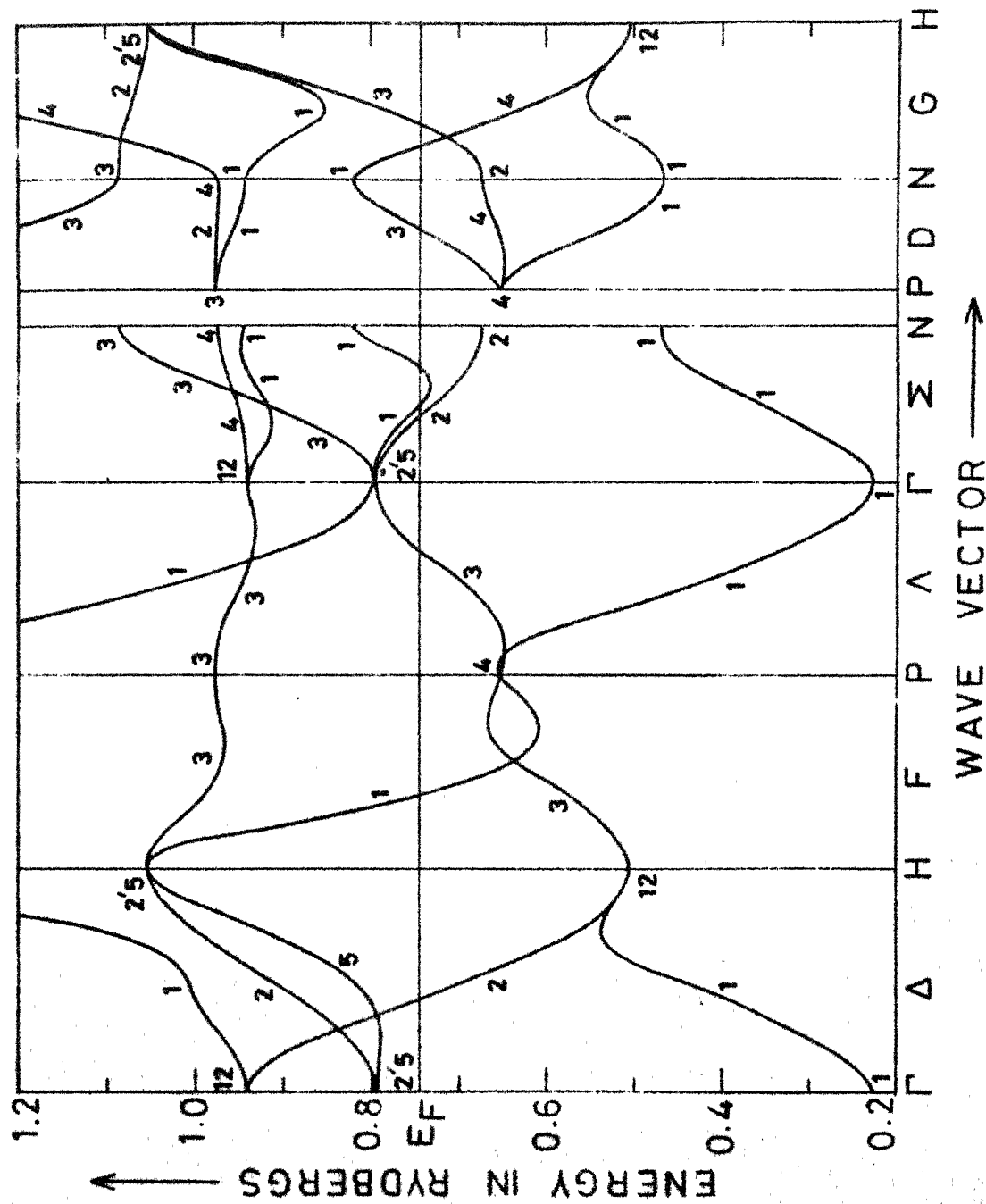
Fig. 4.3: Band structure of V along some important symmetry directions.
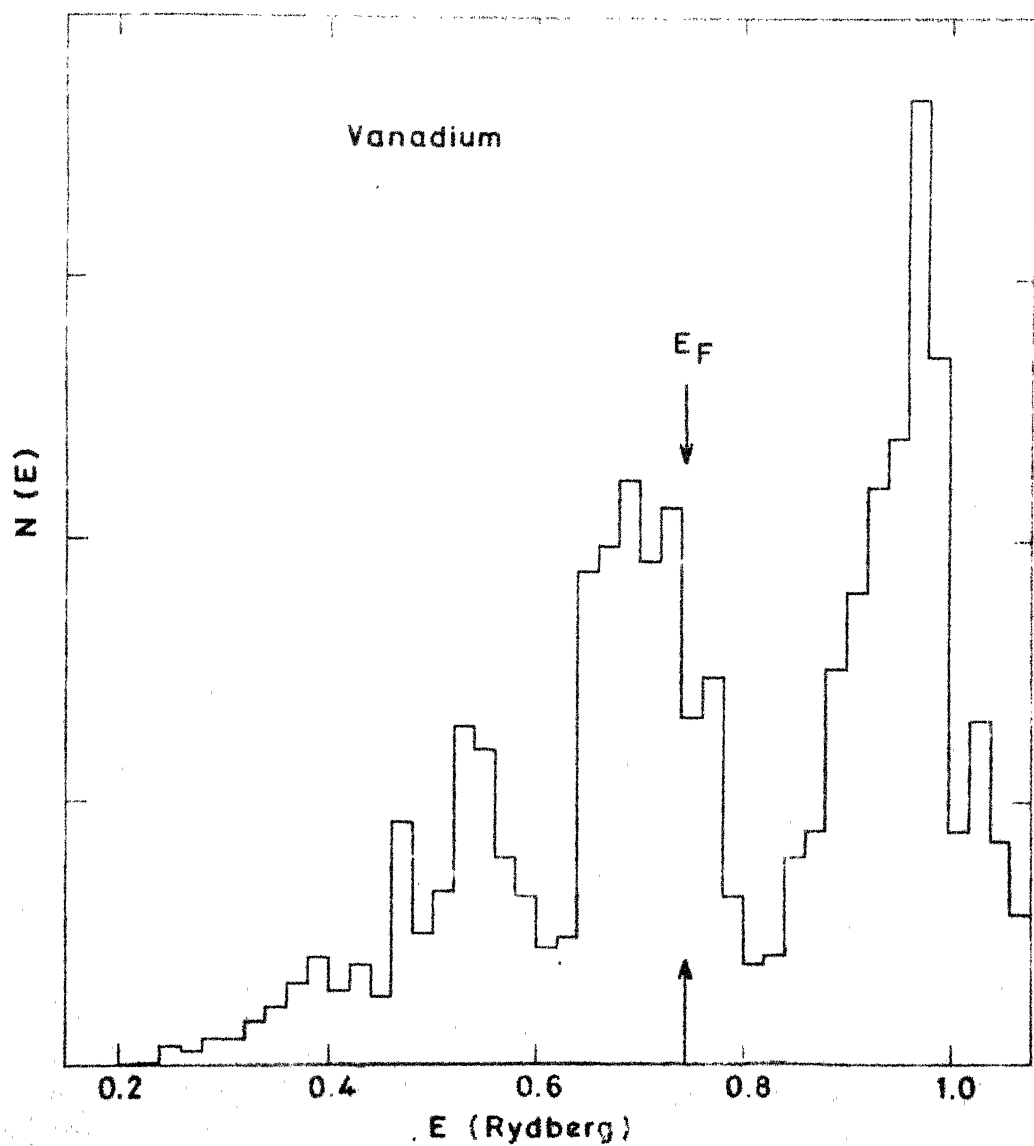
Fig. 4.4: Density of states histogram for V. The Fermi energy E_F was 0.746 Ry.

Table 4.4. Electron eigenenergies of vanadium at some symmetry
points determined by the present calculation.

I.R.	$\vec{k}\,(\frac{2\pi}{a})$			band 1	band 2	band 3	band 4	band 5	band 6
Γ	0	0	0	0.227	0.795	0.795	0.795	0.941	0.941
Δ	0	$\frac{1}{2}$	0	0.447	0.694	0.822	0.822	0.915	1.008
H	0	1	0	0.505	0.505	1.054	1.054	1.054	1.474
G	$\frac{3}{10}$	$\frac{7}{10}$	0	0.540	0.650	0.766	0.856	1.075	1.182
N	$\frac{1}{2}$	$\frac{1}{2}$	0	0.467	0.671	0.823	0.944	0.973	1.086
Σ	$\frac{3}{10}$	$\frac{3}{10}$	0	0.385	0.710	0.732	0.928	0.956	0.965
D	$\frac{1}{2}$	$\frac{1}{2}$	$\frac{3}{10}$	0.578	0.649	0.710	0.966	0.976	1.285
P	$\frac{1}{2}$	$\frac{1}{2}$	$\frac{1}{2}$	0.652	0.652	0.652	0.976	0.976	1.282
Λ	$\frac{3}{10}$	$\frac{3}{10}$	$\frac{3}{10}$	0.475	0.672	0.672	0.955	0.955	1.092
F	$\frac{3}{10}$	$\frac{3}{10}$	$\frac{3}{10}$	0.625	0.647	0.647	0.966	0.966	1.360

Table 4.5. Comparison of energy bandwidths (in Rydberg) for V.

Method used and reference	APW SC α=1 Ref.[5]	APW SC α=2/3 [6]	APW NSC State Dependent [6]	APW [7]	APW α=1 [8]	MOPW SC α=0.725 [9]	APW SC α=0.715 [10]	(EMP) [11]	Present Work
bandwidth									
s-d separation									
$\Gamma_{25'} - \Gamma_1$	0.543	0.506	0.521	0.530	0.479	0.454	0.490	0.512	0.568
$H_{25'} - \Gamma_1$	0.791	–	–	0.750	–	–	–	–	0.827
d-bandwidth									
$H_{25'} - H_{12}$	0.535	0.486	0.437	0.49	–	–	–	–	0.549
$\Gamma_{12} - \Gamma_{25'}$	0.140	0.126	0.157	0.13	–	–	–	–	0.146
s-p bandwidth									
$N_1 - \Gamma_1$	0.583	0.584	0.580	–	0.514	0.594	0.587	0.563	0.595
$H_{15} - \Gamma_1$	1.22	–	–	1.21	–	–	–	–	1.247
occupied d width $E_F - H_{12}$	0.241	0.220	0.191	0.242	0.213	0.158	0.220	0.144	0.241 (0.22)*
occupied s-d width $E_F - \Gamma_1$	0.497	0.470	0.490	0.510	0.417	0.440	0.463	0.485	0.519 (0.47)*

*Results of experimental work [12,13].

important $\vec{k}$-points and some important bandwidths are given in Tables 4.4 and 4.5 respectively and the bandwidths are compared with the results of other calculations [5-11] and experiments [12,13].

The bandwidths and band structure obtained by us show a satisfactory agreement with the results of Papaconstantopoulos et al. [5], the minor disagreement could be due to the difference in the potential, method of band structure used and the self-consistent character of the other calculation. In particular the second lowest Σ_1 band, which is interesting from the point of view of possible necks along the ΓN direction (Sec. 2.3), dips below the Fermi level $E = E_F$ by about 12 mRy as compared to 18 mRy as found elsewhere [14]. The agreement between our results for the bandwidths and those by Wakoh and Yamashita [6], however, is not so good although the band structure results look similar.

4.3 Results for the Fermi Surface

Using our band structure results and the value of $E_F = 0.746$ Ry (Fig. 4.3) the Fermi surface (FS) of V was obtained as usual. The central cross sections of the FS in the (100) and (110) planes of V are shown in Fig. 4.5. Some other cross sections of the FS will be presented later in this Chapter when we shall discuss the 2D-ACPAR curves in the $p_y \neq 0$ planes.
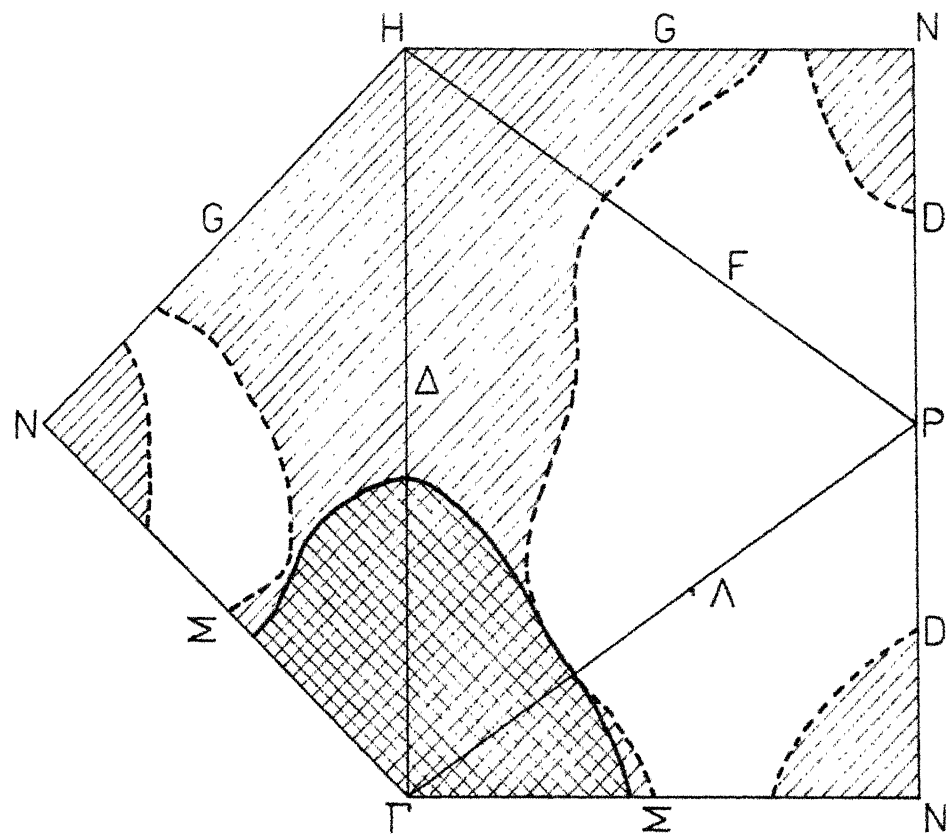
Fig. 4.5: The cross section of the Fermi surface of vanadium by the (100) and (110) planes. The hatched area ▨▨▨ denotes the second band and ▨▨▨ denotes the third band unoccupied FS.

These results display the following familiar features
of the FS of V : (i) Second band hole surface centered at Γ ,
(ii) Third band distorted ellipsoidal surface centered at N
(hereinafter called as NCE), and (iii) third band multiply
connected ''jungle-gym'' arms along <100> directions (here-
inafter called as JGA). A rough estimate of the size and the
shape of the NCE is given by the ratio of the semiaxes along
NP, NΓ and NH directions. Our results show that NΓ/NP = 0.88
and   NΓ/NH = 1.16 as compared to the crude estimates
NΓ/NP = 0.95 and NΓ/NH = 1.21 obtained experimentally by
Parker and Halloran [15] using magnetothermal oscillation
technique. The FS topology (Fig. 4.5) obtained by us agrees
well with the results of Papaconstantopoulos et al. [5], who
also find, in agreement with us, that there are no narrow
necks connecting the NCE to the JGA along the ΓN direction.

4.4 Positron Wavefunction in V

The positron wavefunction was calculated by expanding
[16] it in terms of the Fourier series (Sec. 3.4)

$$\psi_+(\vec{r}) = \frac{1}{\sqrt{\tau}} \sum_{K} B_{\vec{K}}^+ e^{i\vec{K}.\vec{r}} \tag{4.1}$$

where $\vec{K}$'s are the reciprocal lattice vectors. In the present
calculation we used 8 shells of the reciprocal lattice vectors
besides the vector (0,0,0). The positron wavefunction was
thus expanded in terms of 141 plane waves. The same muffin-
tin potential as in Table 4.2 but with a changed sign was

v : Positron wavefunction

⟨100⟩

⟨110⟩

⟨111⟩

0.15

0.10

0.05

0

1.0 2.0 3.0 4.0

r ⟶ (a.u.)
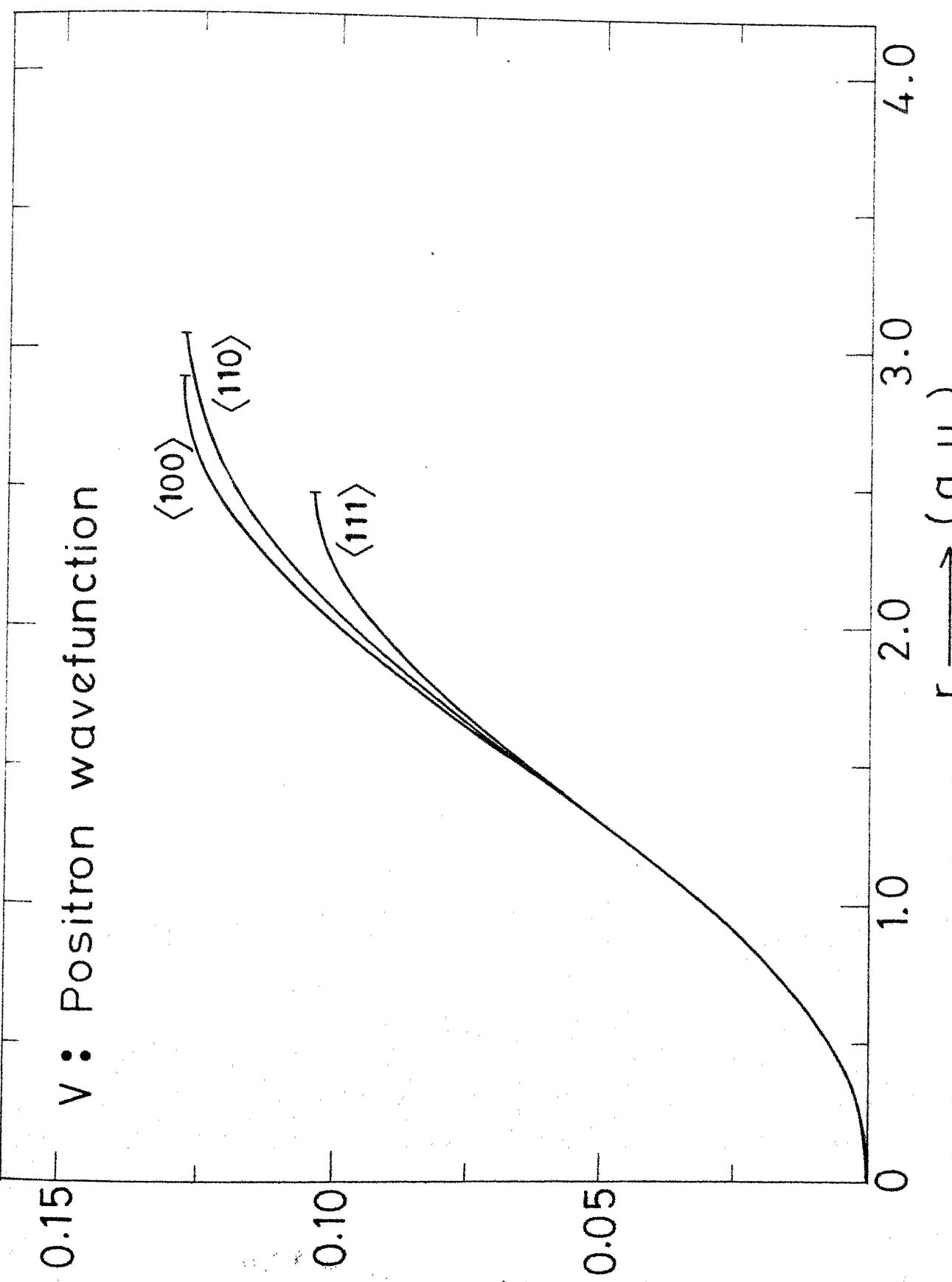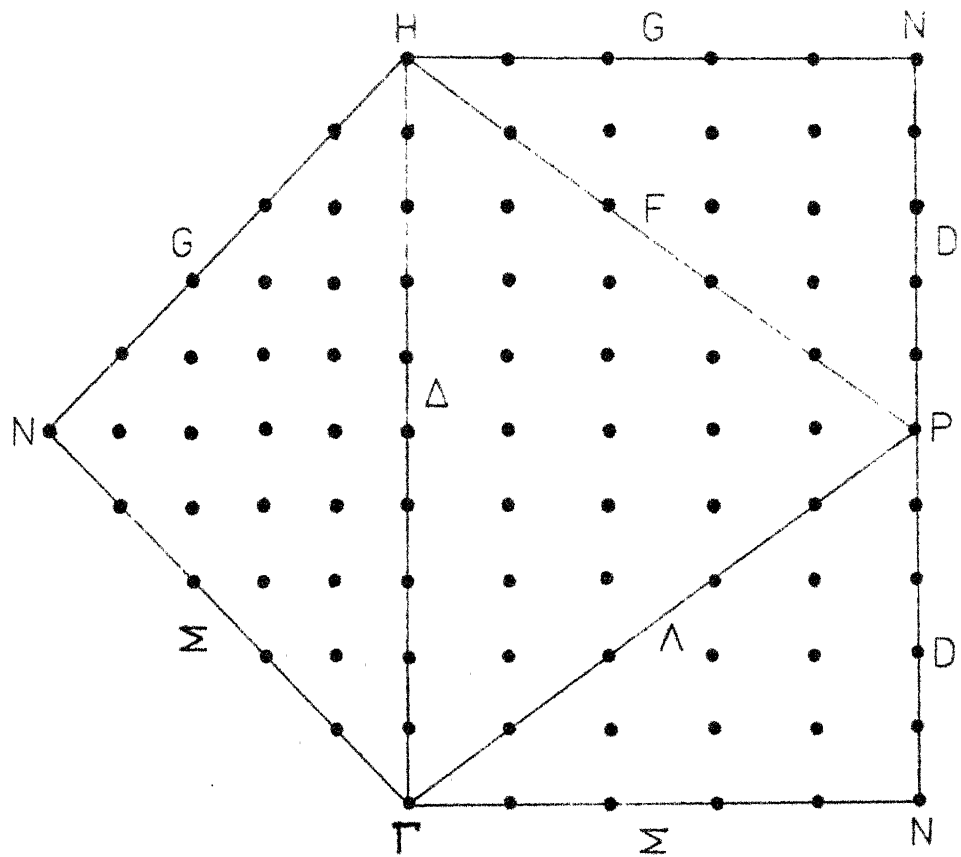
Fig. 4.7: The rectangular grid of the $\vec{k}$-points used in calculating the TPMD, $\mathcal{S}_{b}(\vec{p})$, at the $p(=\vec{k}+\vec{K}_i)$ points in the (100) and (110) planes.

used to calculate the coefficients $B_{\vec{K}}^{\pm}$ following the procedure explained in Sec. 3.4. The lowest energy eigenvalue of the positron (at lowest Γ_1 point, $\vec{k}_+ = 0$) was found to be 0.506 Ry with respect to the zero of the muffin-tin potential. The positron wavefunction, $\psi_+(\vec{r})$ along the three crystal directions <100>, <110> and <111> are shown in Fig. 4.6. In the actual calculation of the TPMD, $\rho(\vec{p})$, (eq. 3.27) we used $R_+(r)/r$, the spherical average of the positron wavefunction calculated inside the inscribed sphere with the help of the following expansion [17]

$$R_+(r)/r = \frac{1}{35} [10 \ \psi_{100}(\vec{r}) + 16 \ \psi_{110}(\vec{r}) + 9 \ \psi_{111}(\vec{r})]$$

$$\ldots \ (4.2)$$

4.5 Two-photon Momentum Distribution

The two-photon momentum distributions[*], $\rho_b(\vec{p})$, due to the band electrons in V was calculated at about 1200 $\vec{p}$-points in the (010) and ($\bar{1}$10) planes using equations (3.1), (3.2) and (3.27) and a set of 141 $\vec{K}$ vectors. The mesh of the $\vec{k}$-points used in these computations is shown in Fig. 4.7. The results for the TPMD, $\rho_b(\vec{p})$, for the three symmetry directions <100>, <110> and <111> are shown in Figs. 4.8 to 4.10. These figures also show the partial contribution to the TPMD, $\rho_b(\vec{p})$, due to individual bands while the

---

[*]Hereinafter we shall denote the TPMD due to the band electrons by the symbol $\rho_b(\vec{p})$.

p in a.u.

$E(\vec{K})$

Σ_4 Σ_1 (B) Σ_1

Σ_3 Σ_2

Σ_1

(A)

1.0 0.8 E_F 0.6 0.4 0.2

Γ Σ N

V: $\langle 110 \rangle$

(A)

(B)

N

$\rho_b(\vec{p})$ in arbitrary units

p in mrad

0.8 0.6 0.4 0.2 0.0

0 5 10 15 20

1.0 2.0
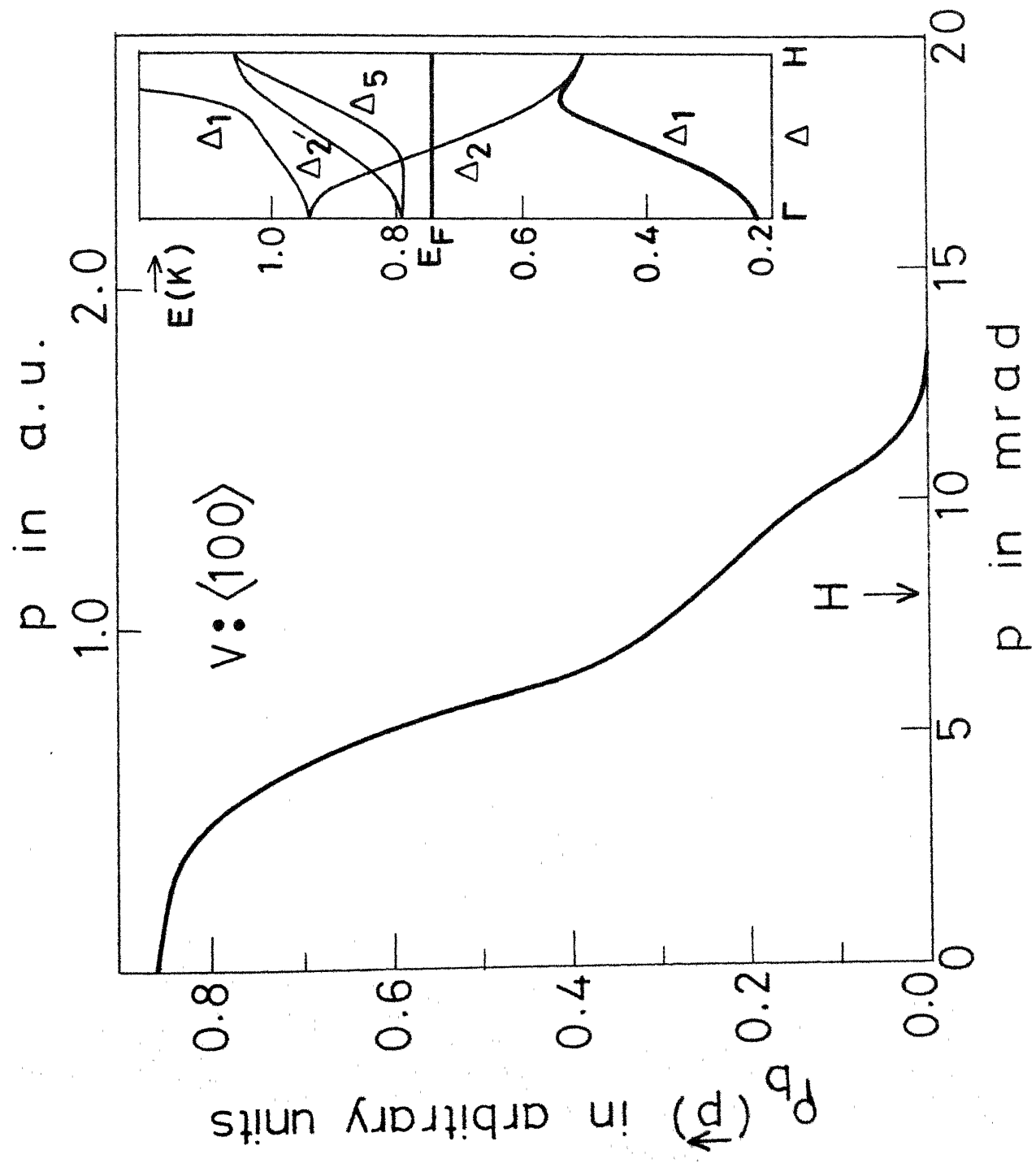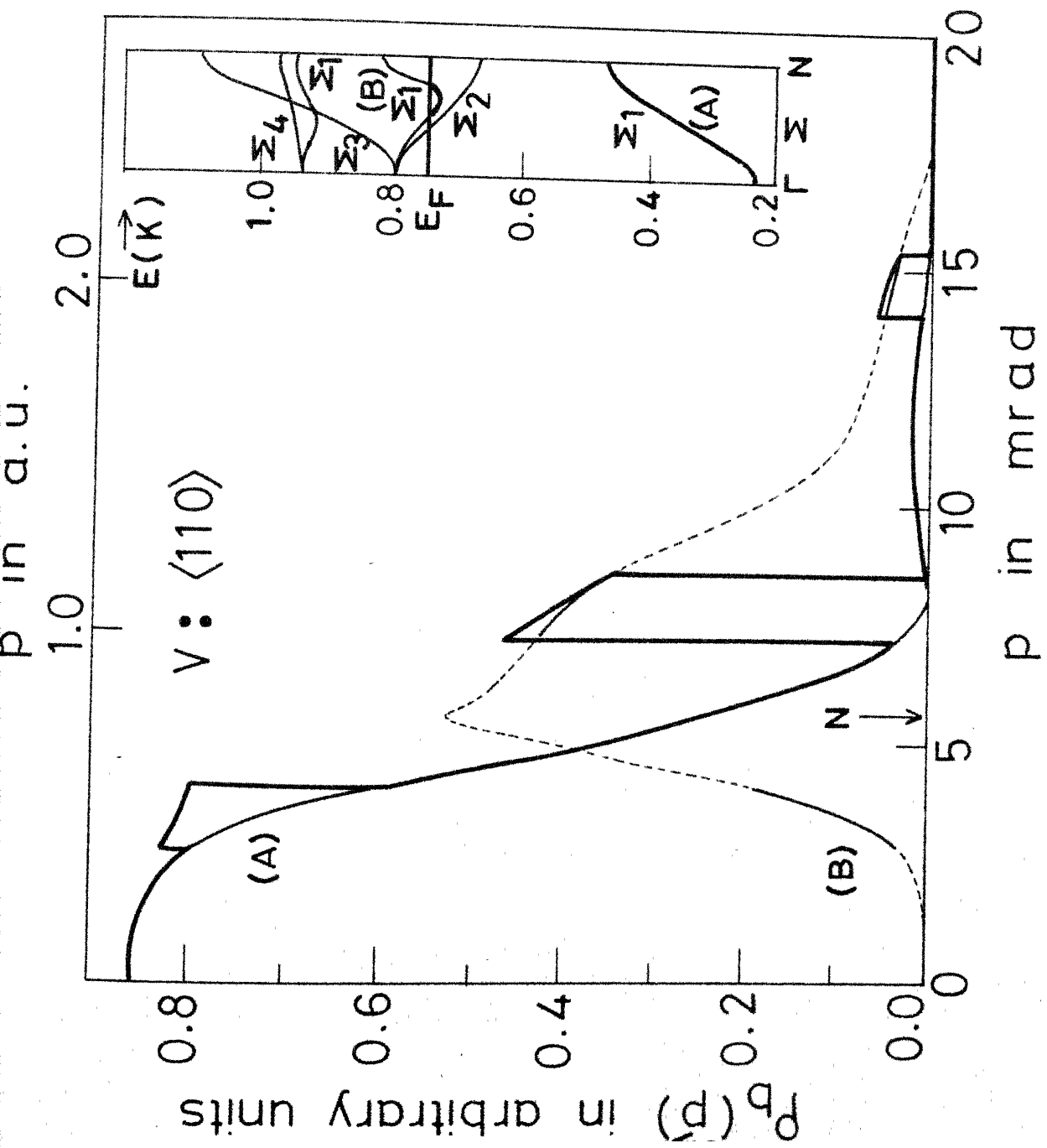
Fig. 4.9: The TMMD, $\rho_b(\vec{p})$, along the $\langle 110 \rangle$ direction in V. The relevant band structure is shown in top inset.

relevant band structure is shown in the inset. The dotted curves show the value of the overlap integral above the Fermi energy although they (being unoccupied) do not contribute to the TPMD.

As pointed out earlier in Sec. 3.1, the total TPMD, $\rho_b(\vec{p})$, due to the band electrons is built up from the contributions from the jth band through the summation

$$\rho_b(\vec{p}) = \sum_{j=1}^{occ} \rho_{b,j}(\vec{p}) \qquad (4.3)$$

where $\rho_{b,j}(\vec{p})$ is the partial TPMD due to the jth band electrons and the summation is carried over the occupied bands. At a given point $\vec{p} = \vec{k} + \vec{K}_i$ the value of $\rho_{b,j}(\vec{p})$ is determined by $|A_j(\vec{k},\vec{p})|^2$ whose value, in turn, is determined by $\psi_{\vec{k},j}(\vec{r})$ and $\psi_+(\vec{r})$ (Sec. 1.4) as well as by the so-called symmetry selection rule. A group-theoretical treatment of the symmetry properties of the TPMD by Mijnarends [18] and Harthoorn and Mijnarends [19] has shown that the contribution to the TPMD from an individual band may possess nodes on the lines or planes of symmetry. This can be understood from the following expression

$$A_j(\vec{k},\vec{p}) = \int_{cell} e^{-i\vec{p}\cdot\vec{r}} \, \psi_{\vec{k},j}(\vec{r}) \, \psi_+(\vec{r}) \, d\vec{r} \qquad (4.4)$$

The behaviour of $A_j(\vec{k},\vec{p})$ under the operations R of $\mathcal{G}_0(\vec{k})$, the group of $\vec{k}$, determines the symmetry properties of $A(\vec{k},\vec{p})$. The basis function for the irreducible representation

Γ^j of $\mathcal{U}_0$ is the wavefunction $\psi_{\vec{k},j}(\vec{r})$ and the term $\exp(-i\vec{p}.\vec{r})$ should contain a part which will transform according to the same representation if the integral in eq. (4.4) has to be non-vanishing. This criterion is facilitated by the definition of a projection operator

$$\mathcal{P}^j = (\ell_j/h) \sum_R \chi^j(R)^* P_R \qquad (4.5)$$

where ℓ_j is the dimension of Γ^j, h denotes the order of $\mathcal{U}_0(\vec{k})$, $\chi^j(R)$ describes the character of the operator R for this representation and P_R is the operator corresponding to R. When the projection operator, $\mathcal{P}^j$, is operated on a function $\varnothing_{\vec{p}}$, the part belonging to Γ^j will be projected out of $\varnothing_{\vec{p}}$. In case $\mathcal{P}^j \exp(-i\vec{p}.\vec{r}) = 0$, the exponential term does not contain such a part and we shall have $A_j(\vec{k},\vec{p}) = 0$ for this $\vec{p}$. For the value of $A_j(\vec{k},\vec{p})$ to be non-vanishing we should have $\mathcal{P}^j \exp(-i\vec{p}.\vec{r}) \neq 0$. This symmetry selection rule, therefore, plays an important role while determining the contribution of a particular band to the TPMD, particularly for a transition metal like V whose Fermi energy crosses the d bands. These effects are discussed by Harthoorn and Mijnarends [19] in some detail and we reproduce in Table 4.6 some of their results because these are relevant for discussing the behaviour of TPMD for V. It may be pointed out that the positron wavefunction does not affect the symmetry selection rule because the positron wavefunction is assumed

Table 4.6. Observable energy bands which give non-zero
contribution to the TPMD, $\rho_b(\vec{p})$, at momenta $\vec{p}$
for the bcc lattice [19].

$\vec{p}$			Observable energy bands
p_x	p_y	p_z	
0	0	0	Γ_1
0	0	ξ	Γ_1, Γ_{12}, Γ_{15}, Δ_1, H_1, H_{12}, H_{15}
0	ξ	ξ	Γ_1, Γ_{12}, Γ_{15}, Γ_{25}, $\Gamma_{2'5}$, Σ_1, H_1, H_{12}, H_{15}, H_{25}, $H_{2'5}$, N_1, $N_{1'}$
ξ	ξ	ξ	Γ_1, Γ_{15}, $\Gamma_{2'}$, $\Gamma_{2'5}$, Λ_1, H_1, H_{15}, $H_{2'}$, H_2, $H_{2'5}$, P_1, P_4, F_1
0	ξ	η	Γ_1, Γ_2, Γ_{12}, Γ_{15}, Γ_{25}, $\Gamma_{1'5}$, $\Gamma_{2'5}$, Δ_1, Δ_2, Δ_5, Σ_1, Σ_4, H_1, H_2, H_{12}, H_{15}, H_{25}, $H_{1'5}$, $H_{2'5}$, N_1, N_4, $N_{1'}$, $N_{4'}$, G_1, G_4, $(\Gamma HN)_+$
ξ	η	η	Γ_1, Γ_{12}, Γ_{15}, Γ_{25}, $\Gamma_{2'}$, $\Gamma_{1'2'}$, $\Gamma_{1'5'}$, $\Gamma_{2'5}$, Δ_1, Δ_5, $\Delta_{2'}$, Σ_1, Σ_3, Λ_1, Λ_3, H_1, H_{12}, H_{15}, H_{25}, $H_{2'}$, $H_{1'2'}$, $H_{1'5}$, $H_{2'5}$, N_1, $N_2^{\text{*}}$, N_3^{+}, $N_{1'}^{+}$, $N_3^{\text{*}}$, $N_{4'}$, P_1, P_3, P_4, P_5, F_1, F_3, D_1, D_3^{+}, $D_4^{\text{*}}$, $(\Gamma HP)_+$, $(\Gamma NP)_+$
ξ	η	ζ	All energy bands

ξ, η, ζ all $\neq 0$

$^{\text{*}}$Observable when two components of $(a/2\pi)K$ are odd.
†Observable when all components of $(a/2\pi)K$ are even.

To summarise, therefore, the partial contribution $\rho_{b,j}(\vec{p})$ by a jth band to the TPMD is determined by the following factors:

(i) The relation $\vec{p} = \vec{k} + \vec{K}_i$,

(ii) Occupied or unoccupied nature of the jth band at $\vec{k}$,

(iii) The electron wavefunction $\psi_{\vec{k},j}(\vec{r})$ and the positron wavefunction $\psi_+(\vec{r})$,

(iv) Whether the particular symmetry of the jth electron band allows it to contribute to $A_j(\vec{k},\vec{p})$ or not.

These considerations have to be kept in mind while analysing the results of the TPMD in terms of the electron band structure and FS. In particular it has to be remembered that a FS discontinuity in the TPMD cannot always be observed in the first BZ (where it can be strong) because of the symmetry selection rule. In the higher zones the selection rule may allow observation of these continuities but with much weaker amplitude.

The TPMD curve, $\rho_b(\vec{p})$, in V along the <100> direction (Fig. 4.8) shows a smooth momentum dependence without any sharp discontinuity. This behaviour arises out of the fact that only the Δ_1 bands are allowed to contribute along the <100> direction to the TPMD by the symmetry selection rule (Table 4.6). Out of the two Δ_1 bands (Fig. 4.8) only the lowest Δ_1 band remains occupied throughout (i.e. from Γ to H along Δ) and hence there are no FS discontinuities in the TPMD which is smooth. The boundaries of the FS sheet along

the <100> directions (i.e. the Γ-centered octahedral hole surface) arise out of the crossing of the Δ_2 band with the Fermi level and since Δ_2 band does not contribute to $\rho_b(\vec{p})$, this FS sheet is not able to produce a break (or discontinuity) in the $\rho_b(\vec{p})$ curve of Fig. 4.8.

The TPMD, $\rho_b(\vec{p})$, along the <110> direction on the other hand shows sharp discontinuities (Fig. 4.9) arising out of the boundaries of the third band FS sheets (i.e. JGA and NCE described in Sec.4.3). Only the Σ_1 bands are allowed to contribute to the $\rho_b(\vec{p})$ along the <110> direction and as a result the lowest two Σ_1 bands contribute to $\rho_b(\vec{p})$. Out of these two Σ_1 bands the lower (or the bottom-most) band is occupied throughout (i.e. from Γ to N along Σ) while the higher (or third from the bottom) band remains occupied in a small central region midway between Γ and N where it dips below the Fermi level. These features are reflected in the $\rho_b(\vec{p})$ curve (Fig. 4.9) which shows a spike-like structure around $p \sim 3.5$ mrad. These FS discontinuities at $p = 2.74$ and 4.10 mrad are repeated in the higher Brillouin zones giving rise to the so-called 'Umklapp' images(or the so-called high momentum components) at $p = 7.18$ and 8.54 mrad and $p = 14.03$ and 15.39 mrad respectively. Once again the boundary of the Γ-centered octahedral hole surface is not able to cause a discontinuity in the $\rho_b(\vec{p})$ curve along the <110> direction because this boundary is caused by the Σ_2, band which is not allowed to contribute to $\rho_b(\vec{p})$. The width of the spike-

like structure in the $\rho_b(\vec{p})$ curve (Fig. 4.9) is determined

by the dimensions of the FS sheets JGA and NCE along the <110>

direction while its height is determined by the character of

the Σ_1 band below the Fermi level.

The TPMD, $\rho_b(\vec{p})$, along the <111> direction is shown

in Fig. 4.10 and it shows a discontinuity around p ∿11.10

mrad. While going along the <111> direction one follows the

route $\Gamma - \Lambda - P - F - H - F - P - \Lambda - \Gamma$ etc. Between Γ and P only the Λ_1

band is allowed to contribute (Table 4.6) and the lowest Λ_1

band is occupied throughout while the higher Λ_1 band is

unoccupied throughout. As a result the $\rho_b(\vec{p})$ curve shows

no discontinuities from Γ to P along Λ. On the other hand,

along the F direction (i.e. from P to H) only F_1 band is

allowed to contribute and this F_1 band (Fig. 4.10) crosses

the Fermi level midway between P and H. This crossing marks

the boundary of the JGA between P and H and it gives rise to

the discontinuities in the $\rho_b(\vec{p})$ curve (Fig. 4.10) at p ∿11.10

mrad and again at p ∿16.55 mrad. It may be pointed out that

the boundary of the JGA between Γ and P does not show up in

the $\rho_b(\vec{p})$ curve because it is caused by the Λ_3 band which

is not allowed to contribute to $\rho_b(\vec{p})$.

The three curves for the TPMD (Figs. 4.8-4.10) show

features similar to the results for the EMD (for the Compton

scattering) calculated by Gandhi [20]. Although the FS

discontinuities occur at the same points, the high momentum

components in the TPMD are smaller than those in the EMD
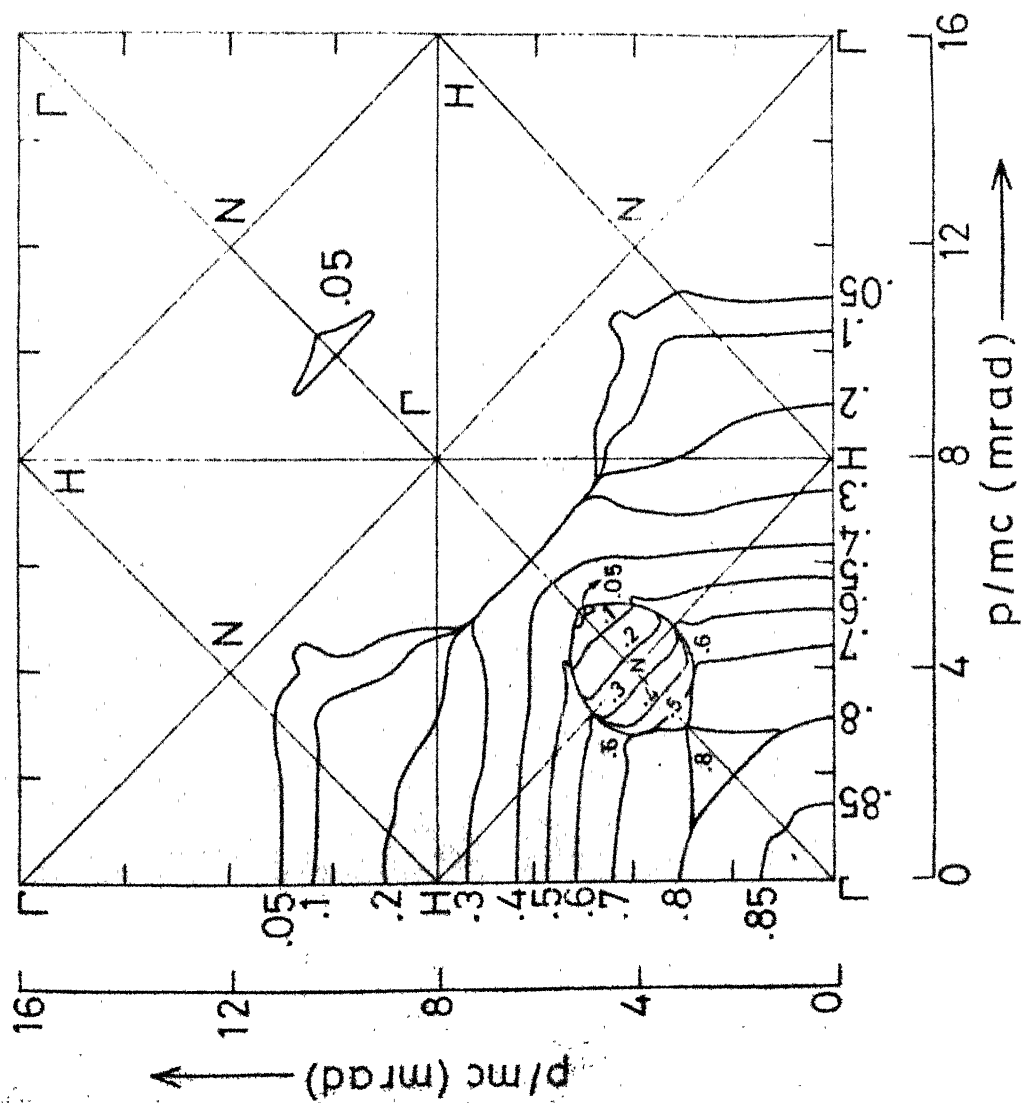
Fig. 4.11: The isodenses of the TPMD, $\rho_b(\vec{p})$, due to the band electrons in the (010) plane of V.
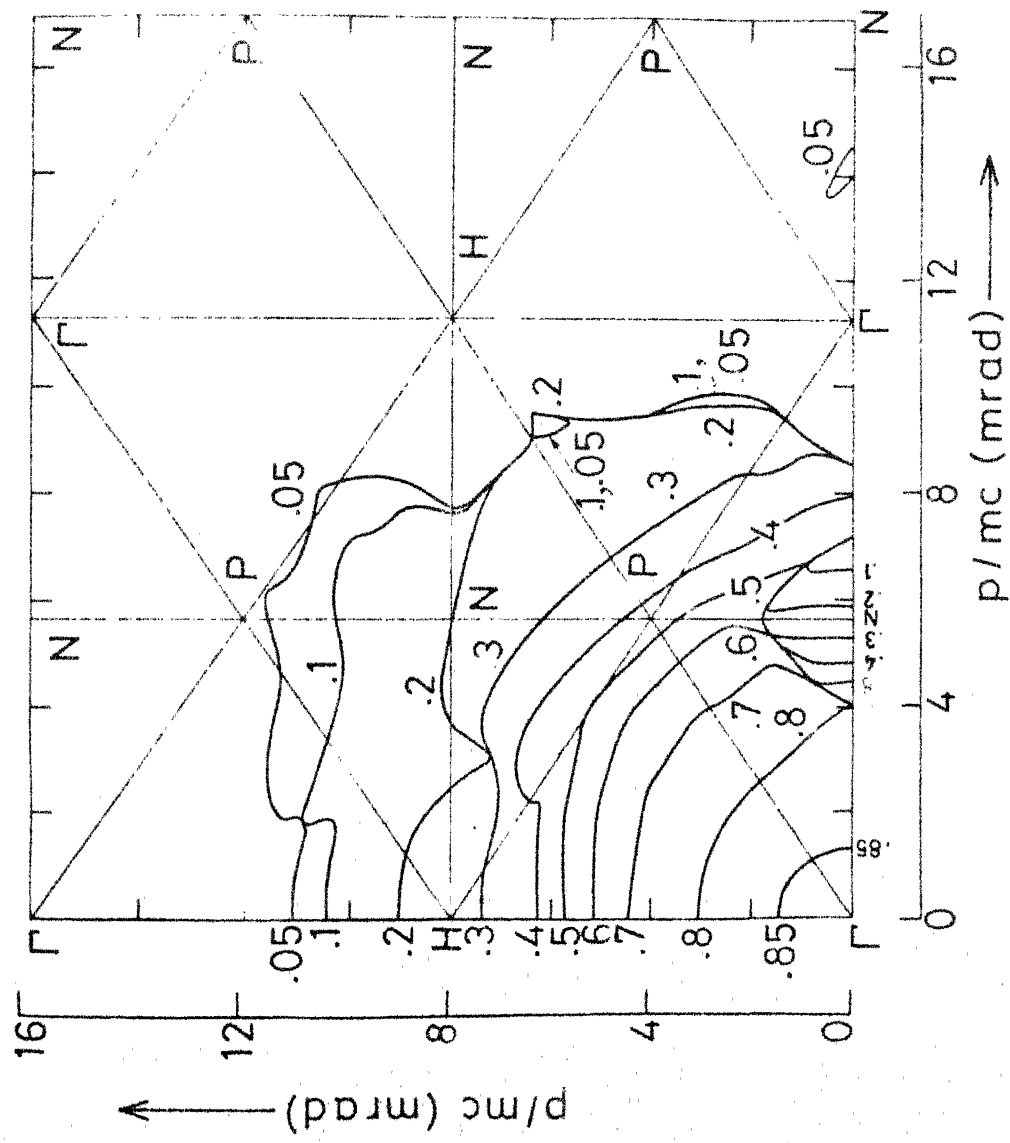
Fig. 4.12: The isodenses of the $\nabla^2 D$, $\rho_b(\vec{r})$, due to the band electrons in the (110) plane of K.
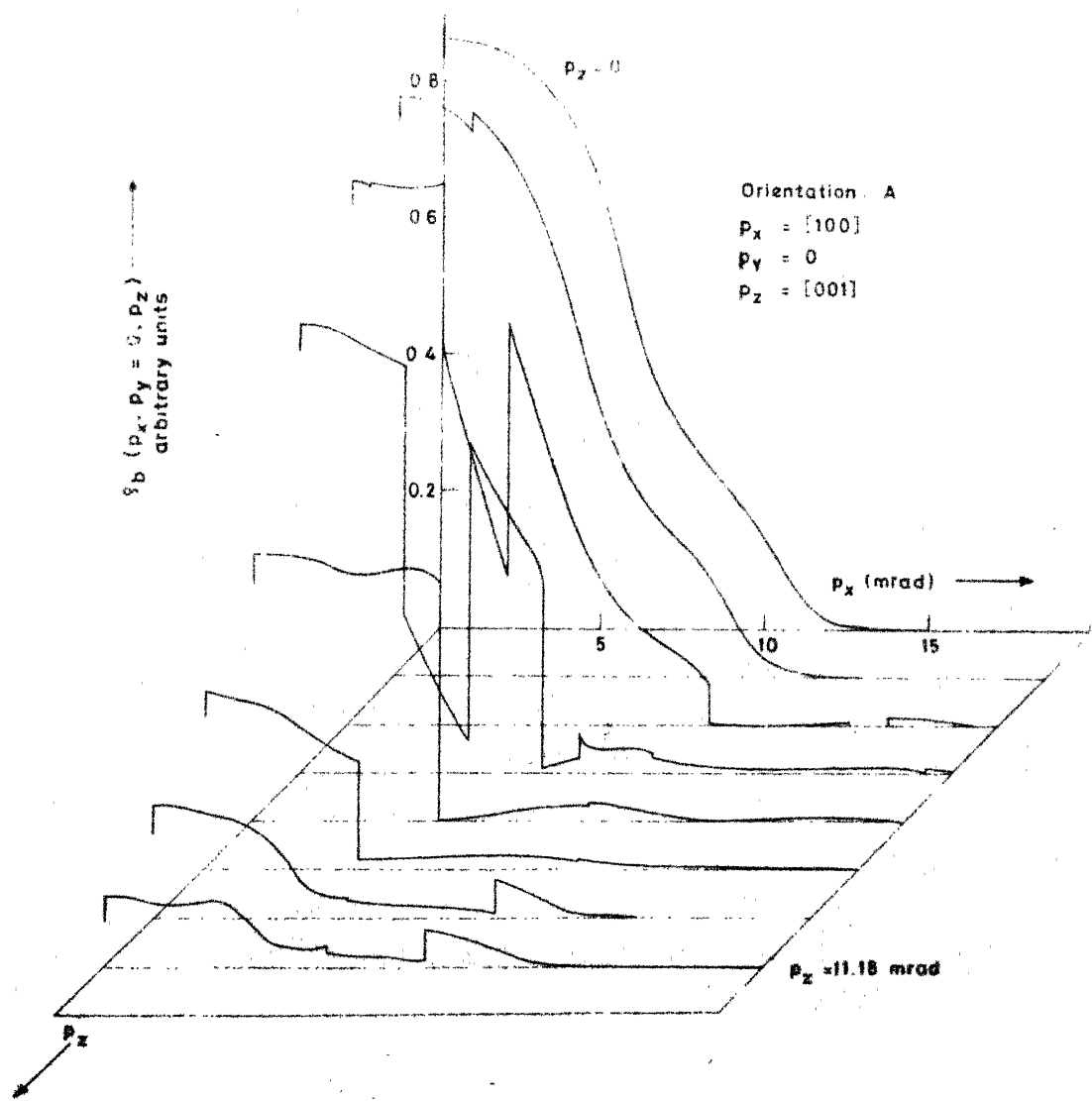
Fig. 4.13: Two-photon momentum density $\rho_b(p_x, p_y = 0, p_z)$ vs p_x in the (010) plane for V for different values of p_z mentioned in the text.
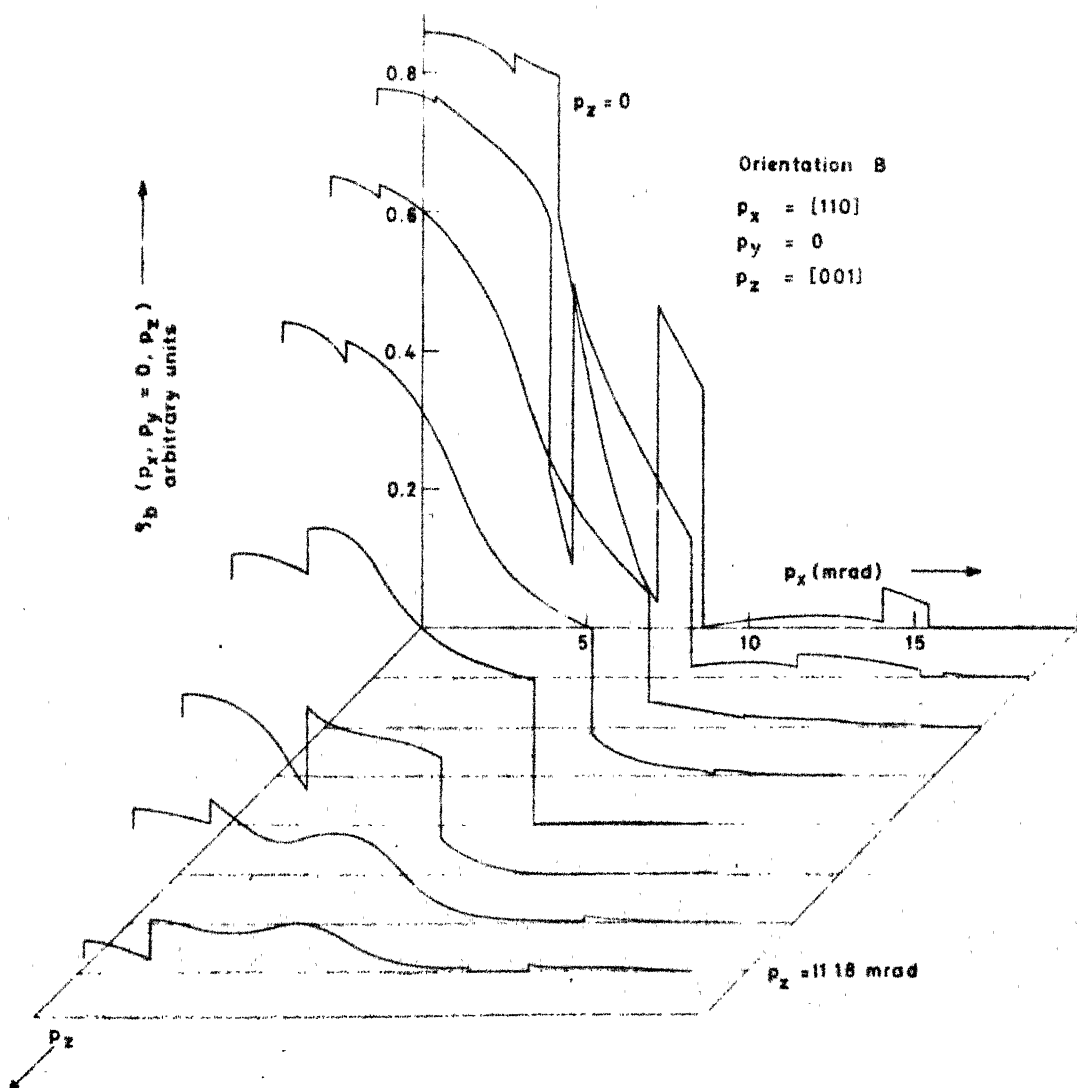
Fig. 4.14: Two-photon momentum density $\rho_b(p_x, p_y = 0, p_z$ vs p_x in the (1̄10) plane for V for different values of p_z mentioned in the text.

for Compton scattering [20]. This behaviour is to be expected because of the effect of the positron wavefunction on the TPMD.

In order to calculate the 2D-ACPAR curves we had to compute the line integral (Eq. 1.8) of the TPMD, $\rho_b(\vec{p})$ in the (010) and ($\bar{1}$10) planes along lines parallel to the p_x-axis for a given orientation $\{p_x, p_y, p_z\}$. In order to provide a better intepretation of the calculated 2D-ACPAR curves we have plotted the contours (hereinafter called as isodenses) of the TPMD, $\rho_b(\vec{p})$, in the two planes (010) and (110) (Figs. 4.11 and 4.12). These curves bring out the highly anisotropic nature of the TPMD in V arising out of the complex FS topology and the d-character of the electron wavefunctions at the FS. In particular the isodenses show a complicated nest-like structure around N and it arises out of the annular FS topology between the NCE and JGA (Fig. 4.5).

The anisotropic nature of the TPMD is also brought out by the plots in Figs.4.13 and 4.14 where the TPMD, $\rho_b(p_x, p_y = 0, p_z)$ vs p_x is plotted for different values of p_z (viz. p_z = 0.0, 1.60, 3.19, 4.79, 6.39, 7.98, 9.58 and 11.18 mrad) in the (010) and ($\bar{1}$10) planes respectively. These curves clearly show the effect of the FS discontinuties and $A_j(\vec{k}, \vec{p})^2$ on the TPMD.

4.6 Two-dimensional Angular Correlation

The results of the TPMD, $\rho_b(\vec{p})$, due to the band electrons in V calculated for about 1200 $\vec{p}$-points in the

Table 4.7. Crystal orientations {p_z,p_x} and momentum mesh
used for the calculation of $N(p_y,p_z)$ curves
i.e. 2D-ACPAR.

Orientation	p_z, p_x $p_y=0$	Plane	Mesh[*] p_z x p_x
A	[001], [100]	(010)	0.80x0.80
B	[001], [110]	($\bar{1}$10)	0.80x1.13
C	[$\bar{1}\bar{1}$2], [111]	($\bar{1}$10)	1.96x1.38
D	[$\bar{1}$10], [110]	(00$\bar{1}$)	1.13x1.13

[*]In units of mrad (i.e. mc x 10^{-3} = 0.137 a.u.).
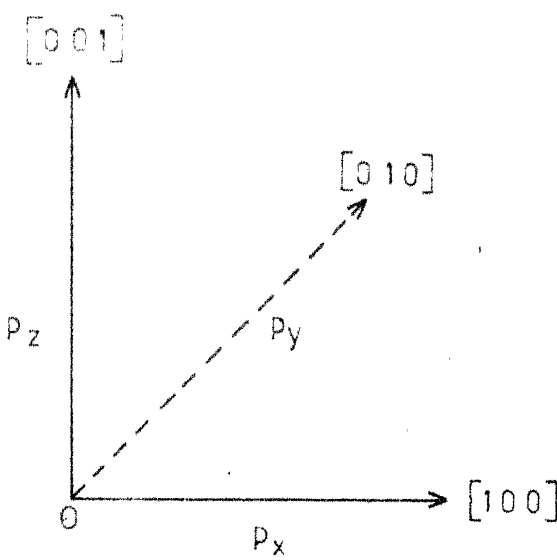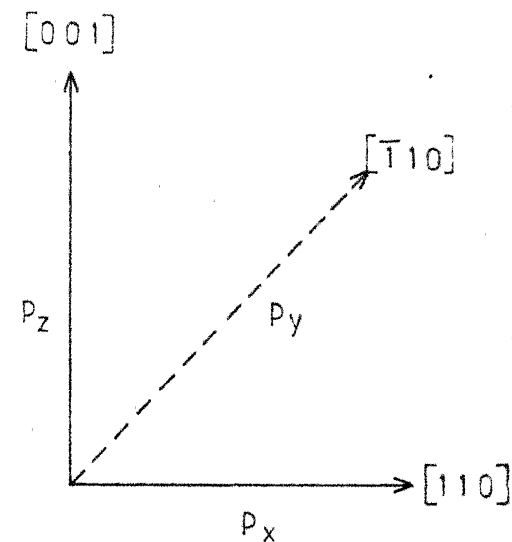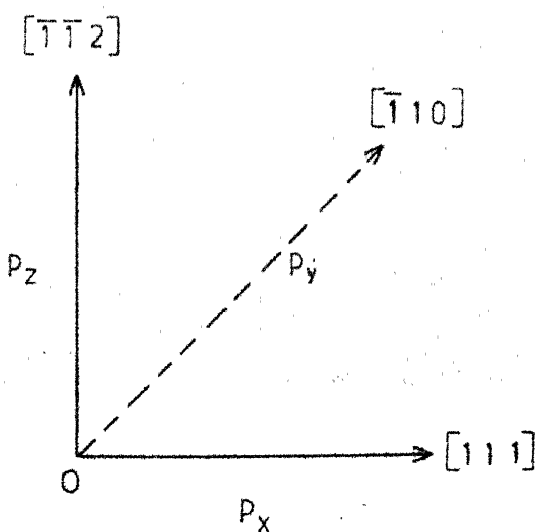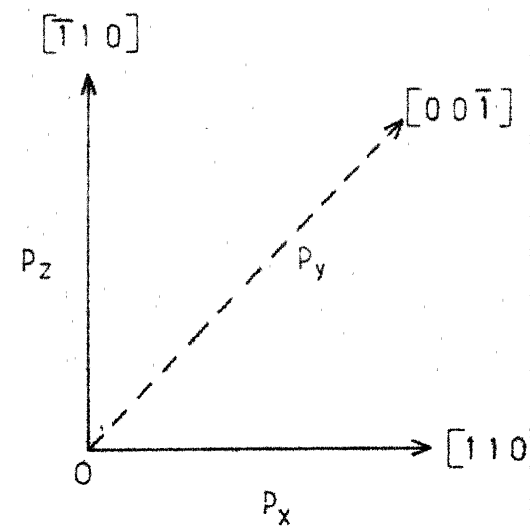
Fig. 4.15: Different orientations A, B, C and D given in Table 4.7.
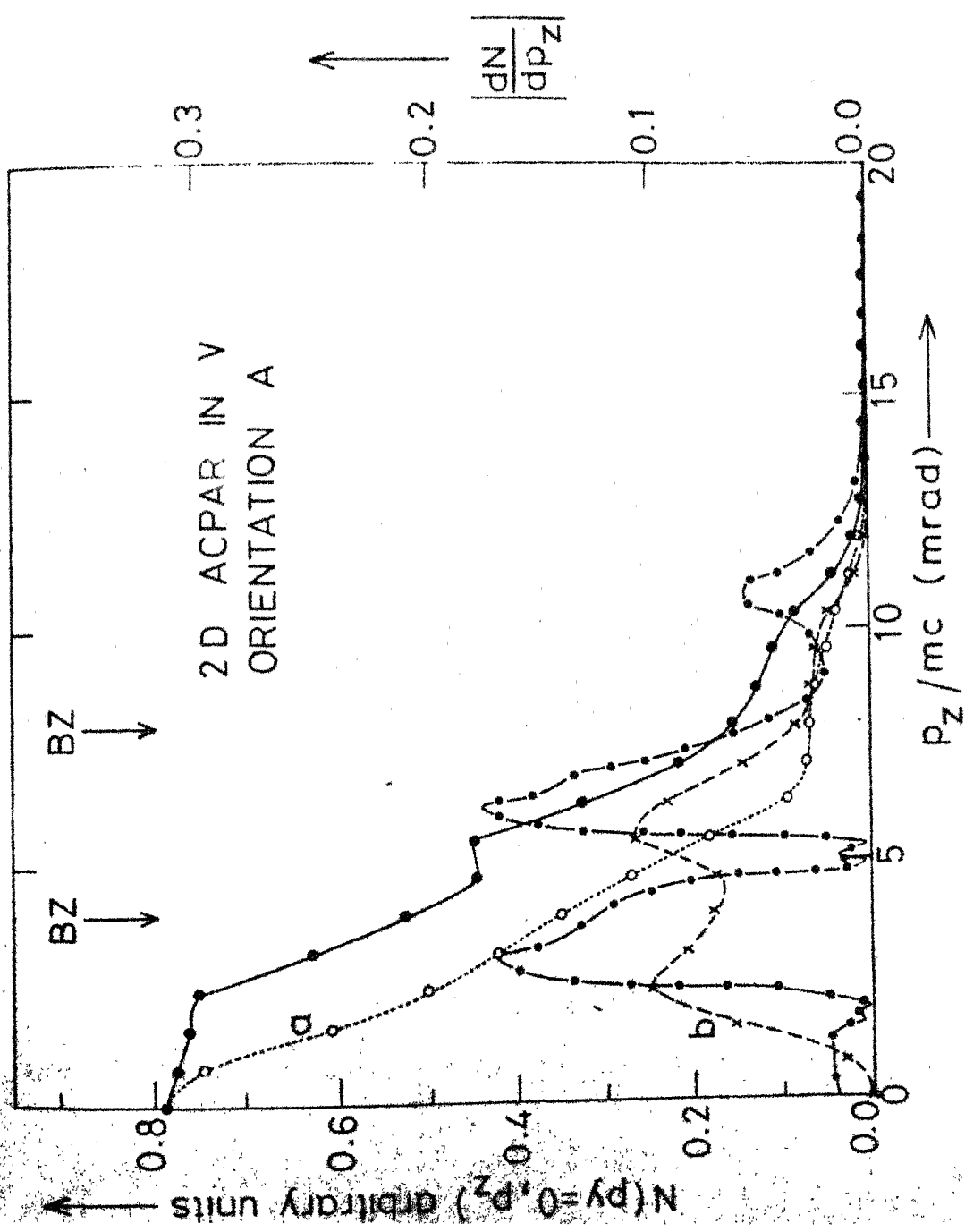
Fig. 4.16: The 2D-ACPAR curve $N(p_y = 0, p_z)$ (solid line) and its derivative $\left(\dfrac{dN}{dp_z}\right)$ for the orientation A: $\{p_z,p_x\} = \{[001], [100]\}$. The dotted curve marked 'a' represents the contribution by the lowest band while
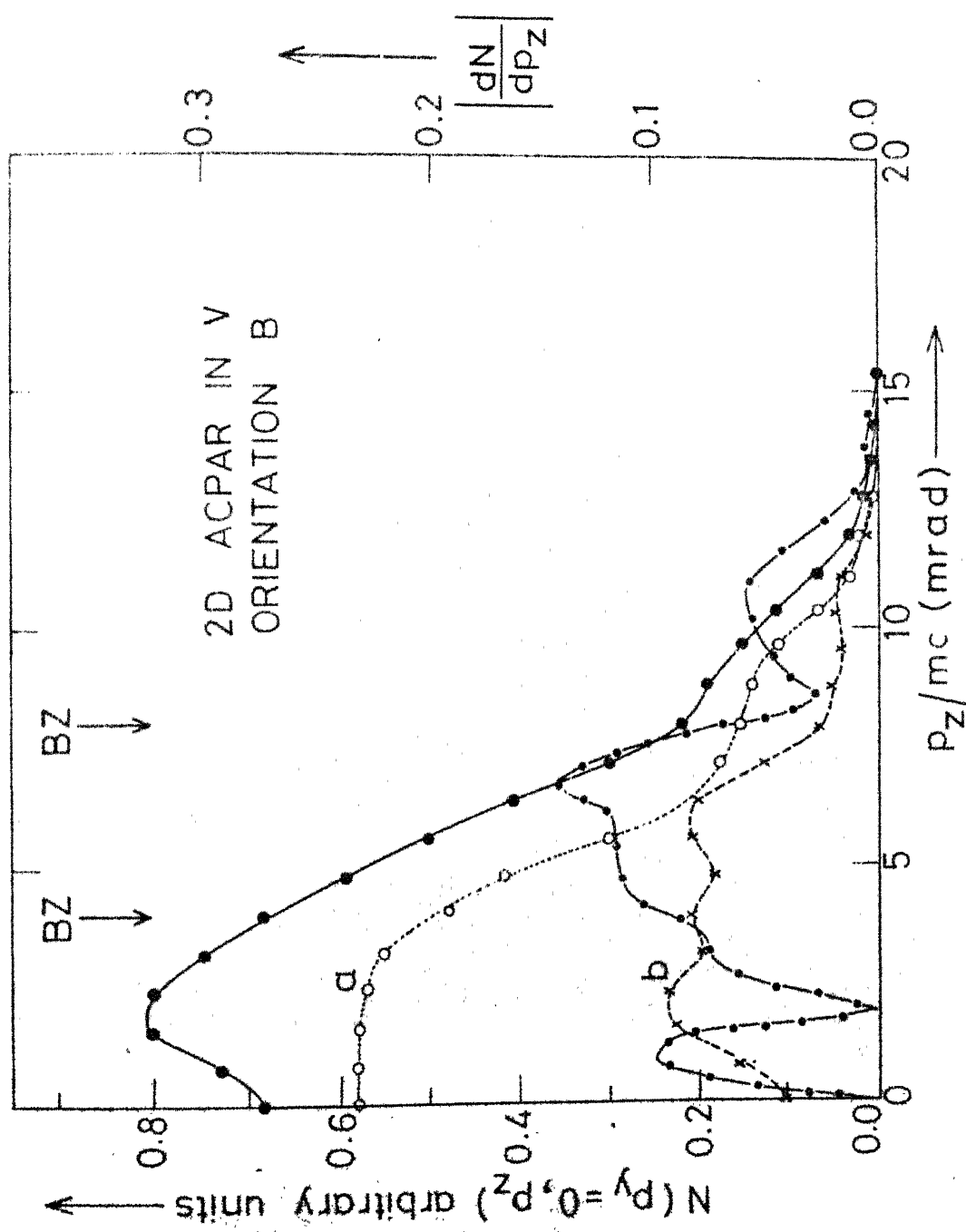
Fig. 4.17: Same as Fig. 4.16 but for orientation B: $\{p_x, p_y\} = \{[001], [110]\}$.

2D ACPAR IN V
ORIENTATION C

BZ

$\frac{dN}{dp_z}$

$p_z/mc\ (mrad)$

$N(p_y=0,p_z)$ arbitrary units
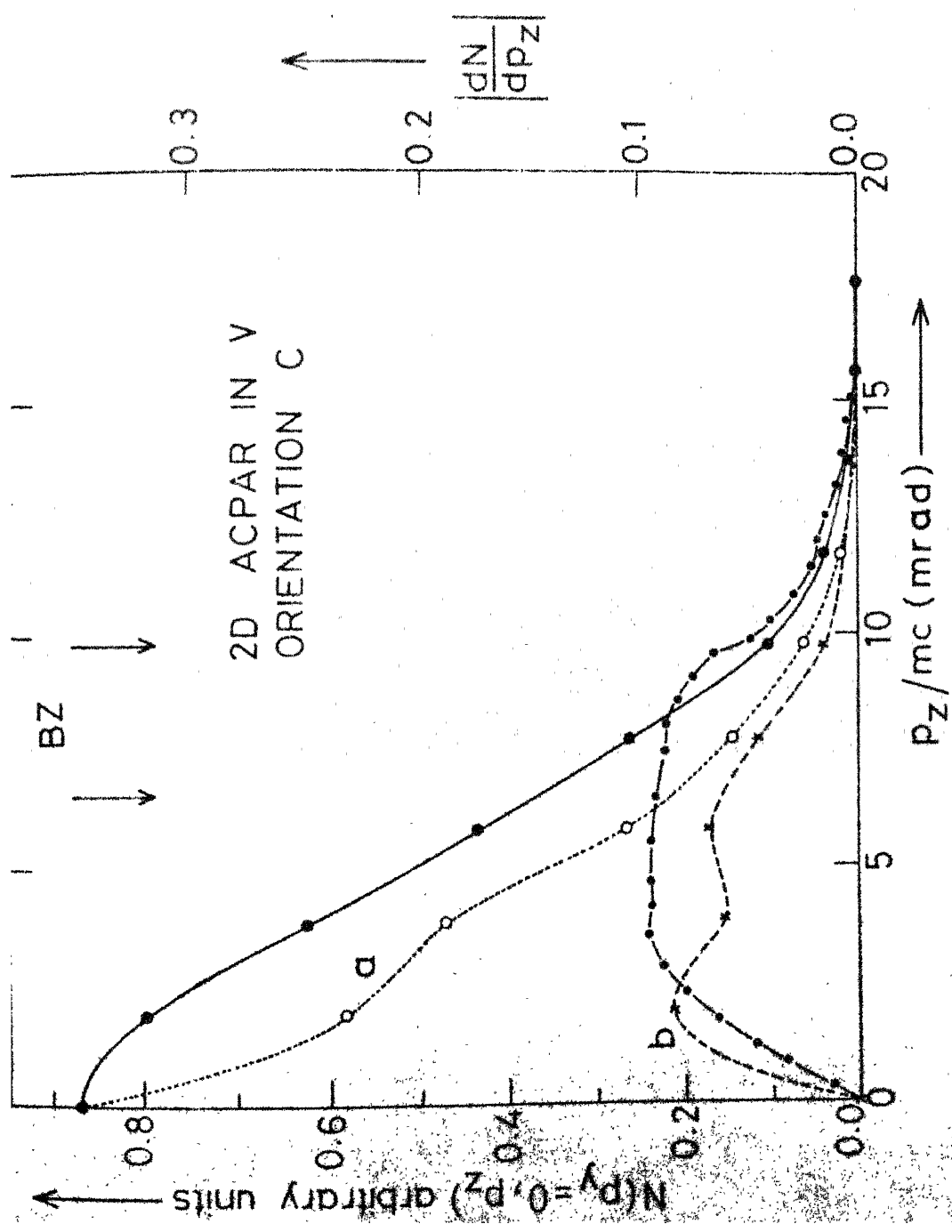
Fig. 4.18: Same as Fig. 4.16 but for orientation
C: $\{p_z, p_x\} = \{[\bar{1}\bar{1}2], [111]\}$.
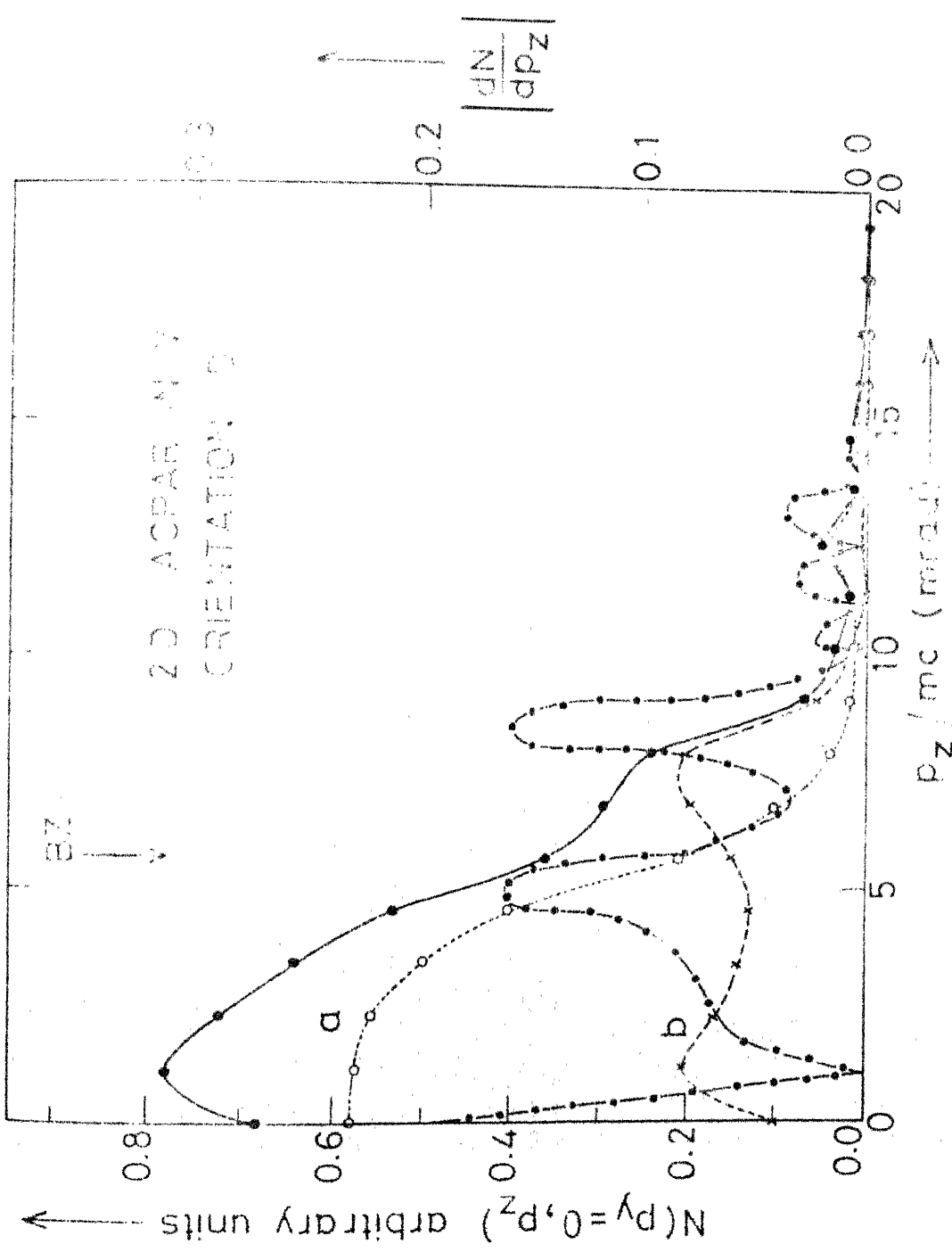
Fig. 4.19: Same as Fig. 4.1b but for orientation
[...], $p_y = (1\bar{1}0)$, $[11\bar{2}]$.

(010) and ($\bar{1}$10) planes on a rectangular momentum mesh (given in Table 4.7) were used to calculate the 2D-ACPAR curves from the following relation:

$$N(p_y,p_z) = \int \rho(p_x,p_y,p_z)\, dp_x \qquad\qquad (4.6)$$

The four crystal orientations used for such calculations are given in Table 4.7 and Fig. 4.15 while the calculated 2D-ACPAR curves are presented in Figs. 4.16 to 4.19. In these figures we have shown the derivatives of the $N(p_y,p_z)$ curve in order to bring out the structure in these $N(p_y,p_z)$ curves. The bandwise (the lowest band is labelled 'a' while the label 'b' refers to lowest second or third band, depending on whichever has (+) symmetry) contribution to the $N(p_y,p_z)$ curves is also shown. While understanding the nature of the $N(p_y,p_z)$ curves it has to be remembered that the contribution by a particular band to $N(p_y,p_z)$ is determined not only by the occupied nature of the band (i.e. FS topology) but also by the symmetry of the band (Sec. 4.5). In case of the general $\vec{p}$-point in the (010) and ($\bar{1}$10) planes $\rho_{b,j}(\vec{p}) = 0$ unless the jth band has positive (+) symmetry. In view of this restriction we have plotted the FS topology of V in the extended zone scheme (Figs.4.20 and 4.21) in the planes (010) and ($\bar{1}$10). The thick curves in Figs. 4.20 and 4.21 are drawn through points at which band 2 and band 3 (counted in order of ascending energy such that the Γ_1 conduction level is at the bottom of the first band) touch and exchange
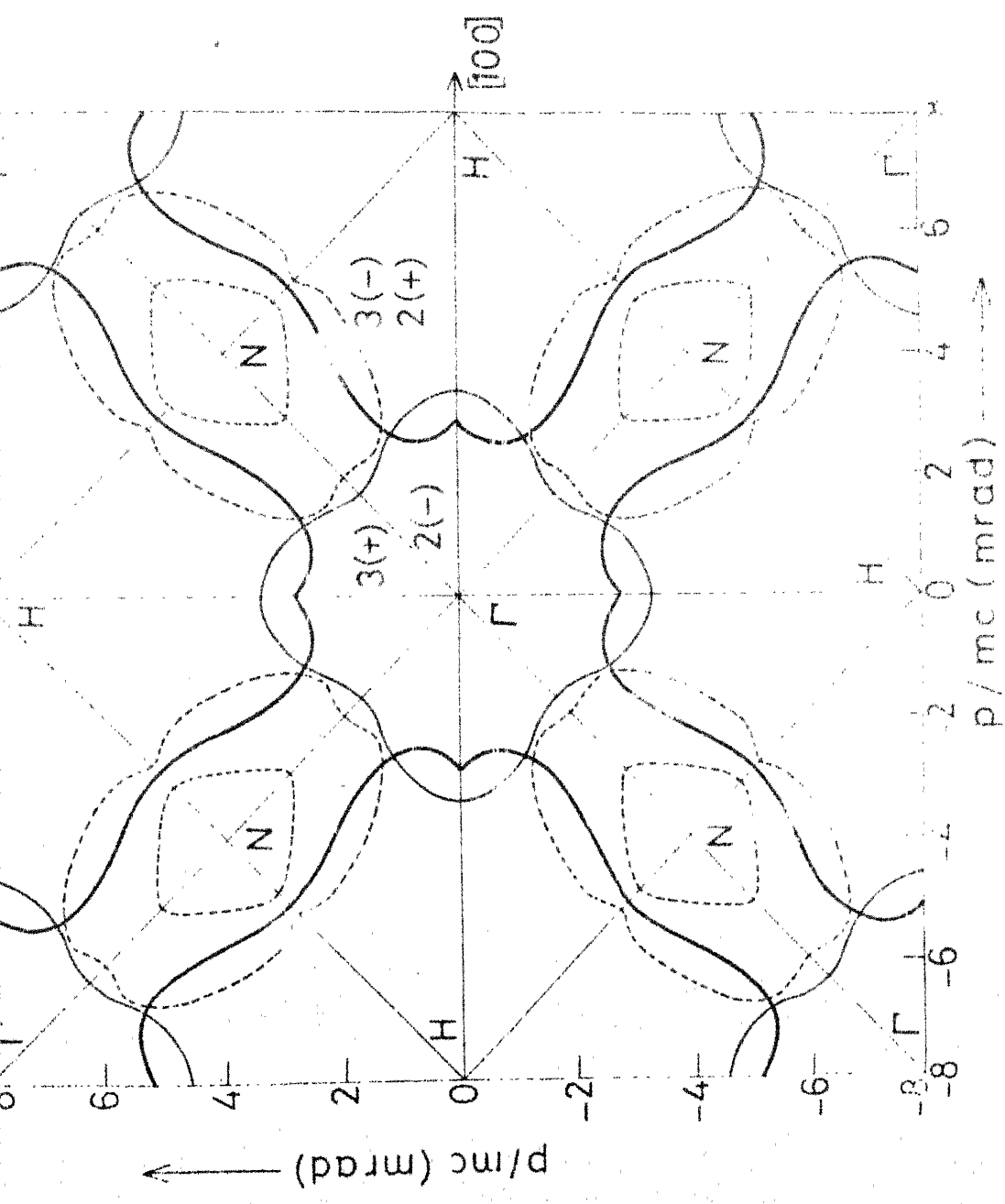
Fig. 4.20: Fermi surface (FS) of V in the (010) plane in the extended zone scheme. The thin continuous curve shows the FS due to the second band while the dashed curve shows the third band FS. The thick continuous curve marks those points at which bands 2 and 3 touch. The labels 3(+), etc., denote the (+) symmetry of the second band in the region (see text).
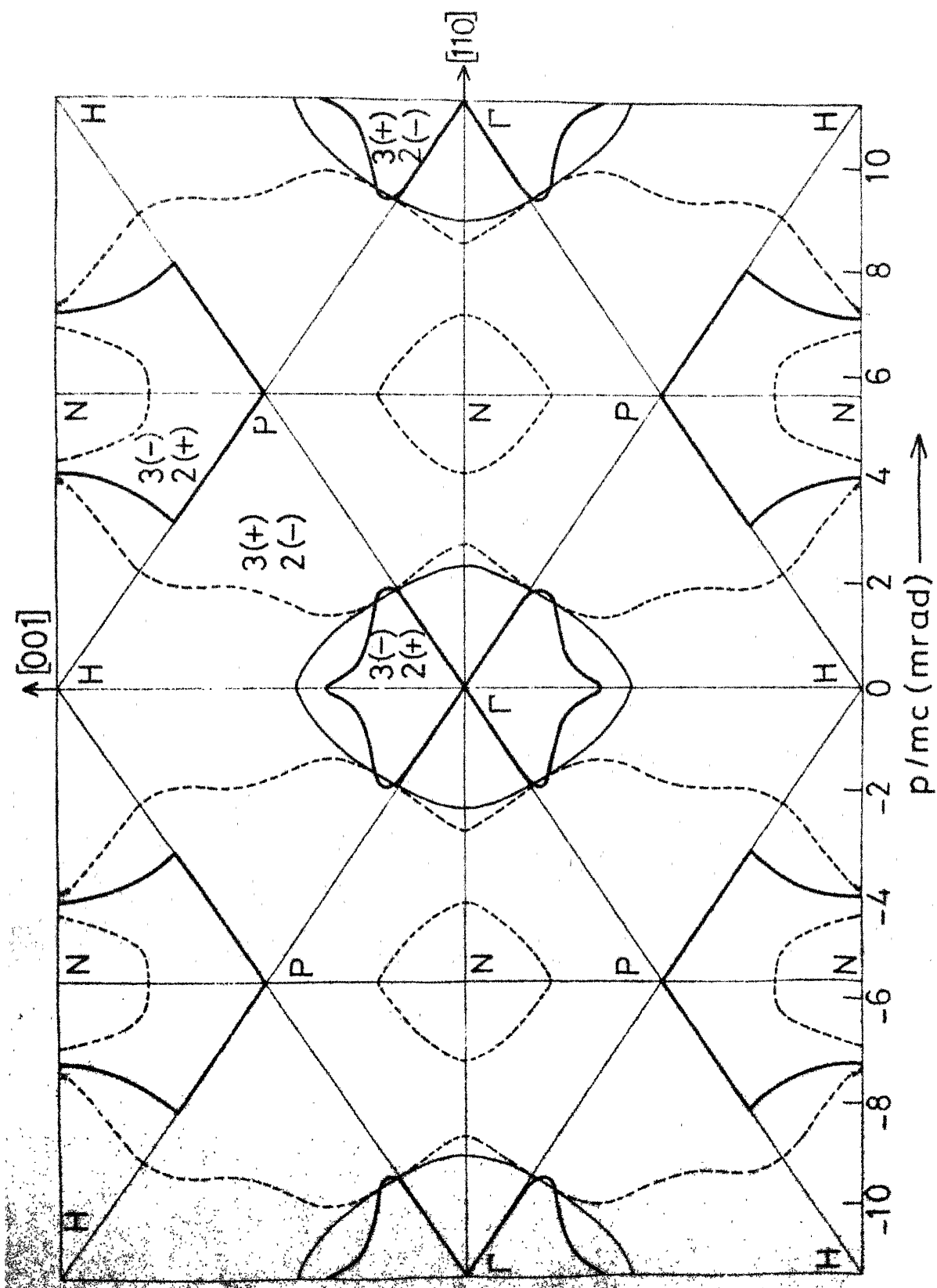
Fig. 4.21: Same as Fig . 4.20 but in the (Ī10) plane.

their positive (+) and negative (−) symmetry. The symbols
2(+), 2(−) etc. are used in Figs. 4.20 and 4.21 to indicate
the symmetries of the second and third band (since fourth
and higher bands being unoccupied do not contribute) in the
different regions of the (010) and ($\bar{1}$10) planes. It will be
useful to refer to the isodenses (Figs. 4.11 and 4.12) and
the FS topology (Figs. 4.20 and 4.21) while discussing the
nature of 2D-ACPAR curves (Figs. 4.16 to 4.19).

The $N(p_y, p_z)$ curve for the orientation A : $p_y = 0$,
$p_z = [001]$ and $p_x = [100]$ shows prominent structure in the
form of shoulders at $p_z \sim 2.4$ mrad and $p_z \sim 5.0$ mrad (Fig.
4.16). It is seen that the contribution to $N(p_y, p_z)$ by the
lowest (labelled 'a') band falls smoothly with p_z while that
due to the higher (second or third band, depending on the (+)
symmetry, labelled 'b') band shows two peaks which give rise to
the structure in the total $N(p_y, p_z)$ curve. When analysed in
terms of the TPMD curves (Fig. 4.13), the TPMD isodenses
(Fig. 4.11) and the FS topology (Fig. 4.20), the structure
at $p_z > 2.4$ mrad can be ascribed to the fall in $\rho_b(\vec{p})$ inside
the NCE (i.e. the line of integration, parallel to the p_x
axis, passes through N-centered ellipsoid). It may be
pointed out that for the low p_z-values there is no visible
effect of the dimensions (or boundaries) of the JGA on the
$N(p_y, p_z)$ curve because in this region the $\rho_b(\vec{p})$ due to the
third band is low (it varies as p^4 for the d-states at
small momenta). The shoulder in the $N(p_y, p_z)$ curve at

$p_z \sim 5.0$ mrad once again arises because the line of integration (parallel to the p_x-axis) has now moved out of the NCE. This behaviour also explains the two peaks in the partial contribution to the $N(p_y, p_z)$ curve by the band 'b'. The steady fall in the $N(p_y, p_z)$ curve after $p_z = 6.0$ mrad is due to the general momentum-dependent decrease in the $\rho_b(\vec{p})$ as well as due to the discontinuities arising from the boundaries of the JGA around $p_z = 5.6$ mrad, and $p_x = 6.4$ mrad. To summarise, therefore, the $N(p_y, p_z)$ curve for the orientation A shows effects due to the NCE while the effects of the JGA are masked out because at higher $(p_z > 2.5$ mrad) momenta the boundaries of the JGA lie in the $3(-)$ symmetry region.

The results of Fig. 4.17 show that the $N(p_y, p_z)$ curve for the orientation B : $p_y = 0$, $p_z = [001]$ and $p_x = [110]$ exhibits a concavity at $p_z \sim 2.0$ mrad. This concave structure is attributed to the NCE as well as the JGA and can be understood with the help of Figs. 4.12, 4.14 and 4.21. The position (i.e. the p_z-value at which the $N(p_y, p_z)$ is maximum) of the concavity is determined by the dimension of the NCE along NP. For example this position would move to a value of p_z smaller than 2.0 mrad if the semiaxis of the ellipsoid NCE (along NP) were smaller than the value obtained by us. The amount of concavity (i.e. $N_{max} - N(p_z = 0)$), on the other hand, is determined by the dimensions along ΓN of the JGA as well as of the NCE. The hump-like structure (Fig. 4.17) at $p_z \sim 8$-10 mrad arises from the lowest band

'a'. It may be pointed out that a concavity is also observed in the Compton profile [21] and the long-slit ACPAR curve [22] from single crystal V for p_z along the [100] direction and these results are explained in terms of the NCE and the JGA sheets of the FS. These experimental results involve, however, surface integration of $\rho_b(\vec{p})$ and hence cannot be directly compared with our results which involve a line integral (4.6).

In comparison to the orientations A and B, the $N(p_y, p_z)$ curve for the orientation C : $p_y = 0$, $p_z = [\bar{1}\bar{1}2]$ and $p_x = [111]$, shown in Fig. 4.18, is smooth and shows no structure. It is possible that some fine structure has been masked out by the relatively coarser (1.96 x 1.38 mrad^2) momentum grid used for orientation C in our calculation. Another possible reason for this smooth behaviour is that the $\rho_b(\vec{p})$ is not symmetric about the p_z-axis for this particular orientation C and any fine structure can get folded up while integrating $\rho_b(\vec{p})$ from $p_x = -\infty$ to $p_x = +\infty$.

The $N(p_y, p_z)$ curve for the orientation D : $p_y = 0$, $p_z = [\bar{1}10]$ and $p_x = [110]$ also show a concavity at $p_z \sim 1.0$ mrad (Fig. 4.19). This concavity arises out of the NCE as well as the JGA as seen from Fig. 4.11 and 4.20. The position of the concavity is determined by the dimension of the NCE along the NH direction while the amount of the concavity is determined by the dimensions along ΓN of both the JGA and the NCE. If the size of the NCE were to shrink along NH the

position of the concavity would move to $p_z < 1.0$ mrad. The
depression in the partial curve 'b' (Fig. 4.19) in the region
$p_z \sim 3.5-7.0$ mrad is caused by the NCE. As a result, the
curve (Fig. 4.19) for the total $N(p_y = 0, p_z)$ in the region
$p_z \sim 3.5-7.0$ falls off faster than in the case the NCE had
not existed.

As pointed out in Chapter 2 there is some controversy
about the dimensions of the NCE and JGA along the ΓN (or Σ)
direction. The model FS of V obtained by Mattheiss [23] as
well as the measurements by Parker and Halloran [15] indicate
a possibility that the NCE's are connected to the JGA's by
narrow necks along ΓN direction. For such necks to exist
the third band in V along the Σ direction should not cross
the Fermi level but lie above it. Our band structure result
(Fig. 4.3) as well as those of Papaconstantopoulos et al.[5]
and Wakoh and Yamashita [6] show the third band (Σ_1) dipping
below the Fermi level and thus preclude the existence of such
necks. We have simulated these necks by lowering the Fermi
energy below $E_F = 0.746$ Ry by about 0.016 Ry (so that the
third band is unoccupied) and have calculated the TPMD as
well as the 2D-ACPAR curves $N(p_y = 0, p_z)$ with $E_F = 0.730$ Ry
for all the four crystal orientations A, B, C and D (Table
4.7). The results of these calculations are shown in Fig.
4.22 where we have plotted

$$\Delta N = N'(p_y = 0, p_z) - N''(p_y = 0, p_z) \qquad (4.7)$$

(where N' $(p_y = 0, p_z)$ and N'' $(p_y = 0, -p_z)$ denote
the values without neck and with neck respectively)
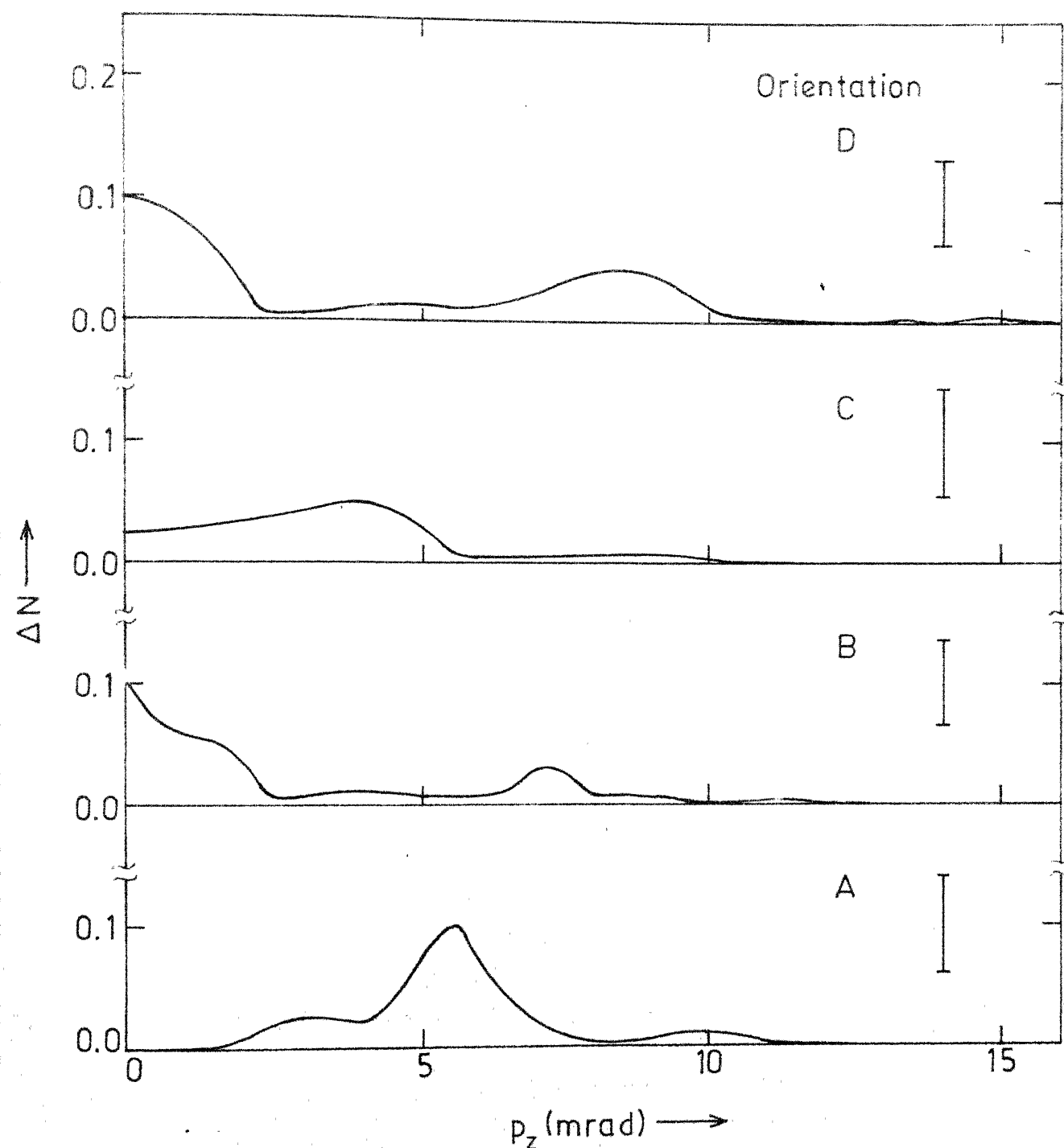
Fig. 4.22: Plot of the ΔN (eq. 4.7) curves to illustrate the effects of the PS neck on the 2D-ACPAR curves (see text).

for the four orientations. The vertical bars shown in Fig.
4.22 represent 10 % of the $N'(p_y = 0, p_z)$ values at $p_z = 0$
for that particular orientation and thus give an idea about
the relative magnitude of ΔN. It is observed from Fig. 4.22
that the presence or absence of the necks affect the 2D-ACPAR
curves for each orientation significantly. Combining the
results of Fig. 4.22 with those of Figs. 4.16-4.19 we see
that the 2D-ACPAR curve for the orientation A will not show
the structure at $p_z \sim 2.4$ mrad and $p_z \sim 5.0$ mrad if there are
necks connecting the NCE's to the JGA's. Presence of these
necks have no effect on the contribution to the 2D-ACPAR
curve by the lowest (+) band (curve 'a' in Fig. 4.16) but
it will affect the partial contribution (curve 'b' in Fig.
4.16) by the higher (+) band. The effect of necks is to
smooth out the curve 'b' as a result of which the shoulders
in the total $N(p_y, p_z)$ curve at $p_z \sim 5.0$ mrad will disappear.
For the crystal orientations B and D, the important effect
due to the presence of these necks would be that the concave
structure around $p_z = 0$ (Figs. 4.17 and 4.19) would deepen,
the difference being maximum (~ 15 %) at $p_z = 0$. The
shoulder-like structure for the orientation D at $p_z \sim 7-9$
mrad would be smoothened out if the necks are present. The
effects of the necks on the $N(p_y = 0, p_z)$ curve for the
orientation C, however, are not so sharp (Fig. 4.22).

We thus find that the measurement of the 2D-ACPAR
in V can throw light on the controversy of necks in the

FS of V. It must be remembered, however, that in practice, the 2D-ACPAR curves are measured with a finite momentum resolution (of the measuring instrument). For example the effective momentum resolution of the multiple (64) NaI-detector system being used at the Brandeis University [24] corresponds to a two-dimensional resolution with nearly Gaussian cross sections of 0.6 mrad x 1.65 mrad FWHM (full-width-at-half-maximum). Before comparing the calculated $N(p_y, p_z)$ curves with the experimental data it is, therefore, essential to fold the theoretical curves with the p_y- and p_z-resolution functions. The dimensions of the necks (connecting the NCE's to the JGA's) in V are expected to be very narrow, if they exist at all. For example, Alward et al. [11] estimate that the dimensions of such necks would be $\sim \frac{1}{25}(\frac{2\pi}{a})$ and would correspond to about 0.3 mrad for V. These numbers therefore suggest that determination of the necks by 2D-ACPAR method is not so easy or straightforward. Although we have discussed the case of V in the above discussion, these conclusions are equally applicable to Nb and Ta which have similar band structure and FS topology.

It is clear from the above discussion that the 2D-ACPAR curves for V are very sensitive to the FS topology. Our calculations (described above) are limited to the four crystal orientations (Table 4.7) all in the $p_y = 0$ plane. In view of the complicated FS of V one expects that 2D-ACPAR curves for V measured in the $p_y \neq 0$ plane (as well as for
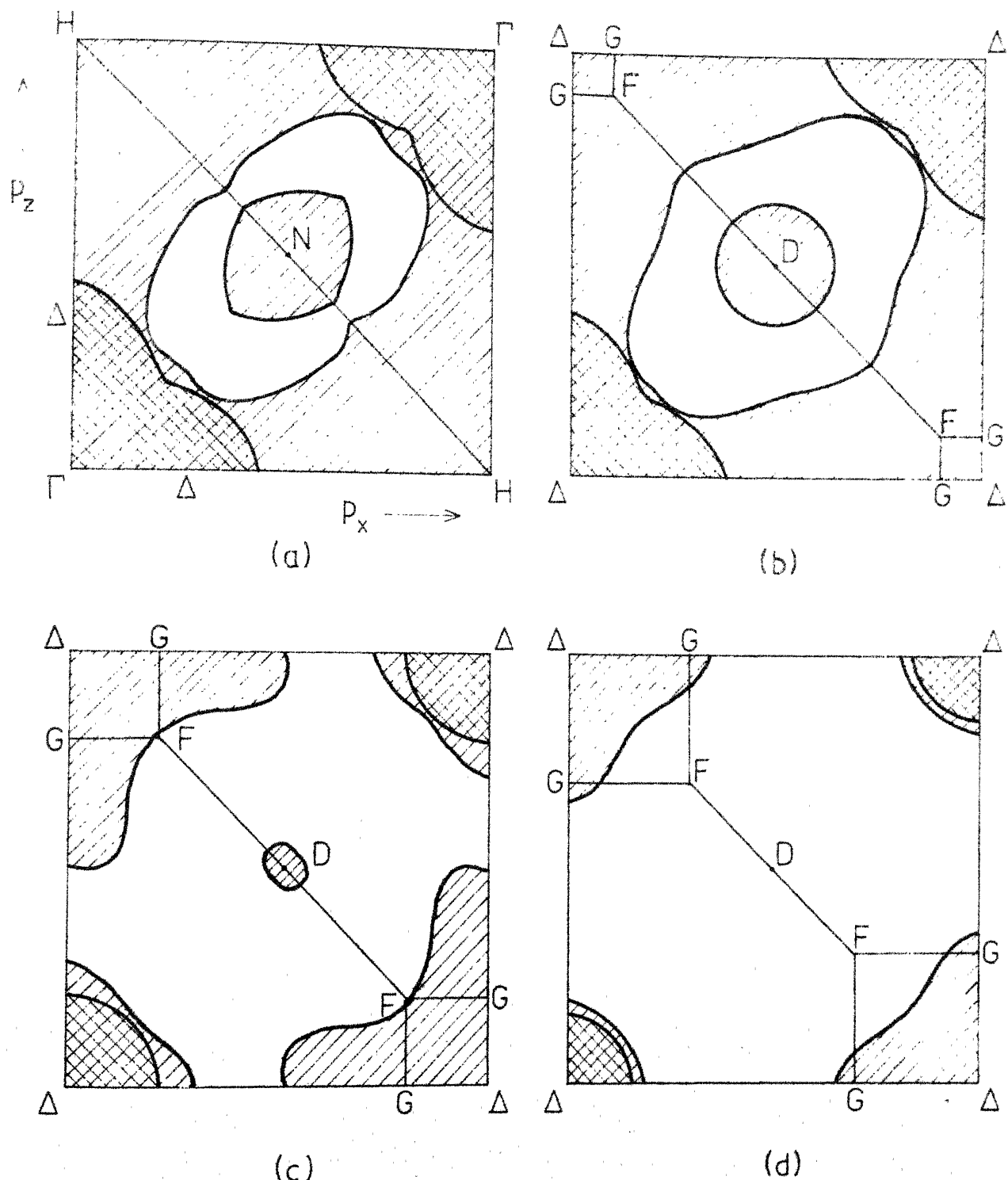
Fig. 4.23: Cross sections of the Fermi surface of V in different $(p_x\ p_z) = (010)$ planes. (a) Plane $p_y = 0$, (b) $p_y = 0.1\ \Gamma H$ (V : $\Gamma H = 7.98$ mrad), (c) $p_y = 0.2\ \Gamma H$ and (d) $p_y = 0.3\ \Gamma H$. The hatched area shows unoccupied region with [hatched] denoting the second band and [hatched] the third band Fermi surface sheet.

(a)

(b)

(c)

(d)
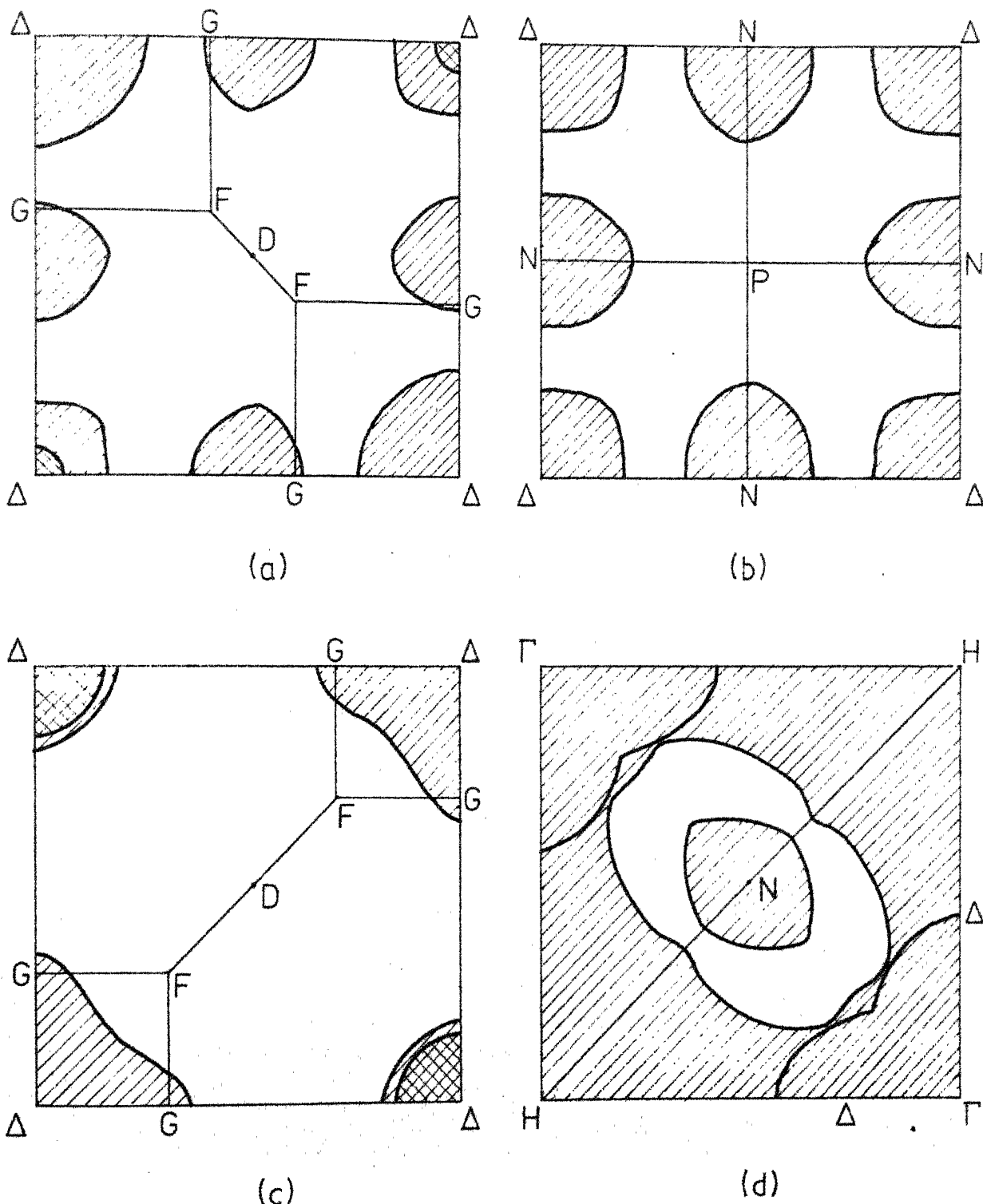
Fig. 4.24:   Same as Fig. 4.23 but for higher (010) planes.
(a) Plane $p_y = 0.4\,\Gamma H$, (b) $p_y = 0.5\,\Gamma H$, (c)
$p_y = 0.7\,\Gamma H$ and (d) $p_y = 1.0\,\Gamma H$.
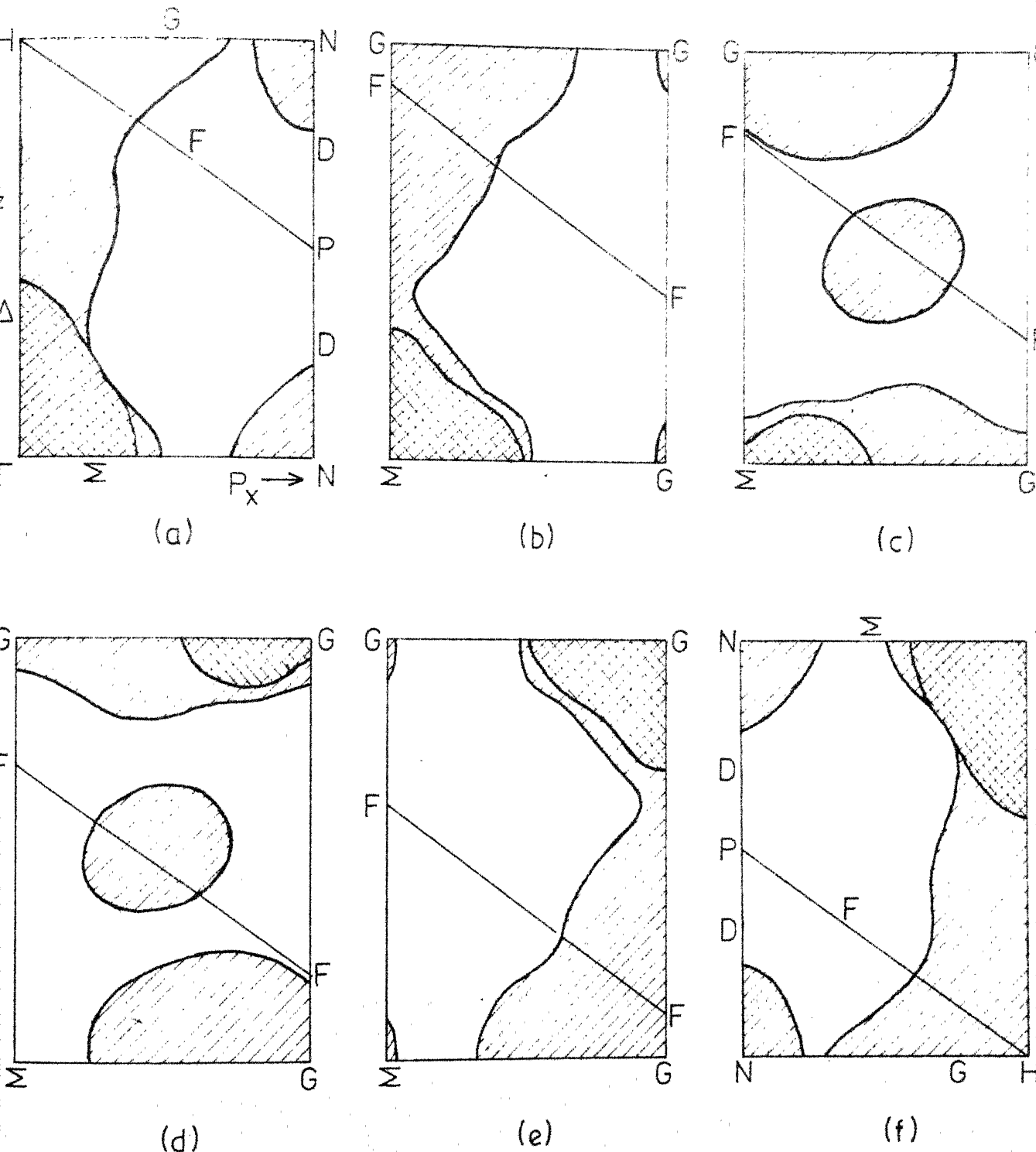
Fig. 4.25: Cross sections of the Fermi surface of V in different $(p_x\ p_z) = (\bar{1}10)$ planes. (a) Plane $p_y = 0$, (b) $p_y = \sqrt{2}\ \Gamma H/10$, (c) $p_y = 2\sqrt{2}\ \Gamma H/10$, (d) $p_y = 3\sqrt{2}\ \Gamma H/10$ (e) $p_y = 4\sqrt{2}\ \Gamma H/10$ and (f) $p_y = 5\sqrt{2}\ \Gamma H/10$. The notation for the hatched areas is same as in Fig.4.2

other crystal orientations) can reveal more detailed information about the FS topology of V. Although we could not calculate the TPMD and the 2D-ACPAR curves in the $p_y \neq 0$ planes because of the high cost of computer time involved, we have calculated the FS topology (from our band structure results) of V in $p_y \neq 0$ planes parallel to the (010) and ($\bar{1}$10) planes. These results are shown in Figs. 4.23-4.25. While using these results (Figs. 4.23-4.25) for guessing the behaviour of the 2D-ACPAR curves $N(p_y \neq 0, p_z)$ two important points should be remembered (i) Although the hole FS sheets do not contribute to the TPMD, their boundaries (or dimensions) cause discontinuities in the TPMD which affect the 2D-ACPAR curves and (ii) In a general plane $p_y \neq 0$, all the occupied bands may contribute to the TPMD provided that the (+)/(-) symmetry labels are not valid.

The FS cross sections shown in Figs. 4.23-4.25 emphasize the highly anisotropic nature of the FS of V. It is observed from Fig. 4.23 that the 2D-ACPAR curves $N(p_y \neq 0, p_z)$ are expected to change sharply while going from $p_y = 0.1$ ΓH (Fig. 4.23b) to $p_y = 0.2$ ΓH (Fig. 4.23c) and these changes would continue as p_y is increased (Fig. 4.24). Such changes in the structure of the $N(p_y \neq 0, p_z)$ curves can provide valuable information about the various dimensions of the different sheets of the FS. Similar argument holds for the results of Fig. 4.25. It may be pointed out that some of the p_y = constant sections not shown in Figs. 4.24 and

4.25 can be inferred from the symmetry considerations. We suggest that the measurements of the $N(p_y \neq 0, p_z)$ should be planned while designing a 2D-ACPAR measurement on V. Results of such experimental measurements, when completed, can be interpreted by using the results presented in Figs. 4.23 to 4.25.

4.7 Corrections for Core Annihilation and Enhancement

The results for the 2D-ACPAR curves presented in the previous section describe the annihilations with the band electrons alone. At present there are no experimental data of the 2D-ACPAR curves in V reported in the literature. For a possible comparison between the theory (present work) and experiment at a future date our raw theoretical data (Sec. 4.6) will have to be corrected. Apart from the correction for the finite angular resolution of the intrument (as discussed in Sec. 4.6) two other important corrections are necessary. Firstly one should include the contribution to the 2D-ACPAR curves by the annihilations with the core electrons. In order to facilitate such a correction we have calculated the core TPMD, $\rho_c(p)$, due to the $(1\underline{s})^2 (2\underline{s})^2 (2\underline{p})^6 (3\underline{s})^2 (3\underline{p})^6$ electrons by the following formula [25]

$$\rho_c(p) = 4\pi \sum_{n,\ell} (2\ell+1) \left| \int_o^{r_s} j_\ell(pr) R_+(r) P_{n\ell}(r) r^2 dr \right|^2$$

$$\ldots \ldots \quad (4.8)$$

where $j_\ell(pr)$ is the spherical Bessel function, $R_+(r)/r$ is the spherically averaged positron wavefunction and $P_{n\ell}(r)/r$'s are

Table 4.8. Two-photon momentum distribution (TPMD), $\rho_c(p)$, of V contributed by the core $[(1\underline{s})^2 \ (2\underline{s})^2 \ (2\underline{p})^6$ $(3\underline{s})^2 \ (3\underline{p})^6]$ electrons.

Sl. No.	p (mrad)	$\rho_c(p)$
1	0.00	0.0444
2	0.73	0.0447
3	1.46	0.0457
4	2.19	0.0472
5	2.92	0.0490
6	3.65	0.0509
7	4.38	0.0527
8	5.11	0.0542
9	5.84	0.0550
10	6.57	0.0550
11	7.30	0.0542
12	8.03	0.0524
13	3.76	0.0497
14	9.49	0.0462
15	10.22	0.0421
16	10.95	0.0375
17	11.68	0.0326
18	12.41	0.0277
19	13.14	0.0229
20	13.87	0.0184
21	14.60	0.0144

Table 4.8 (Continued)

Sl.No.	p (mrad)	$\rho_c(p)$
22	15.32	0.0109
23	16.05	0.0080
24	16.78	0.0057
25	17.51	0.0039
26	18.24	0.0025
27	18.97	0.0016
28	19.70	0.0010
29	20.43	0.0006
30	21.16	0.0004
31	21.89	0.0003
32	22.62	0.0002
33	23.35	0.0002
34	24.08	0.0002
35	24.81	0.0002
36	25.54	0.0002
37	26.27	0.0002
38	27.00	0.0001
39	27.73	0.0001
40	28.46	0.0001
41	29.19	0.0001

Table 4.9. Results for the 2D-ACPAR, $N(p_y = 0, p_z)$ curves for V due to the isotropic core electron TPMD (Table 4.7) $\rho_c(\rho)$.

Sl.No.	m (mrad)	$N(p = \sqrt{p_y^2 + p_z^2})$
1.	0.0	0.0924
2.	0.5	0.0908
3.	1.0	0.0911
4.	1.5	0.0911
5.	2.0	0.0910
6.	2.5	0.0908
7.	3.0	0.0906
8.	3.5	0.0901
9.	4.0	0.0894
10.	4.5	0.0884
11.	5.0	0.0870
12.	5.5	0.0853
13.	6.0	0.0832
14.	6.5	0.0807
15.	7.0	0.0778
16.	7.5	0.0745
17.	8.0	0.0708
18.	8.5	0.0667
19.	9.0	0.0624
20.	9.5	0.0579
21.	10.0	0.0532

Table 4.9 (Continued)

| Sl.No.	p (mrad)	$N(p = \sqrt{p_y^2+p_z^2})$
22.	10.5	0.0485
23.	11.0	0.0437
24.	11.5	0.0390
25.	12.0	0.0345
26.	12.5	0.0301
27.	13.0	0.0260
28.	13.5	0.0222
29.	14.0	0.0187
30.	14.5	0.0155
31.	15.0	0.0128
32.	15.5	0.0103
33.	16.0	0.0082
34.	16.5	0.0065
35.	17.0	0.0050
36.	17.5	0.0038
37.	18.0	0.0029
38.	18.5	0.0022
39.	19.0	0.0017
40.	19.5	0.0013
41.	20.0	0.0010
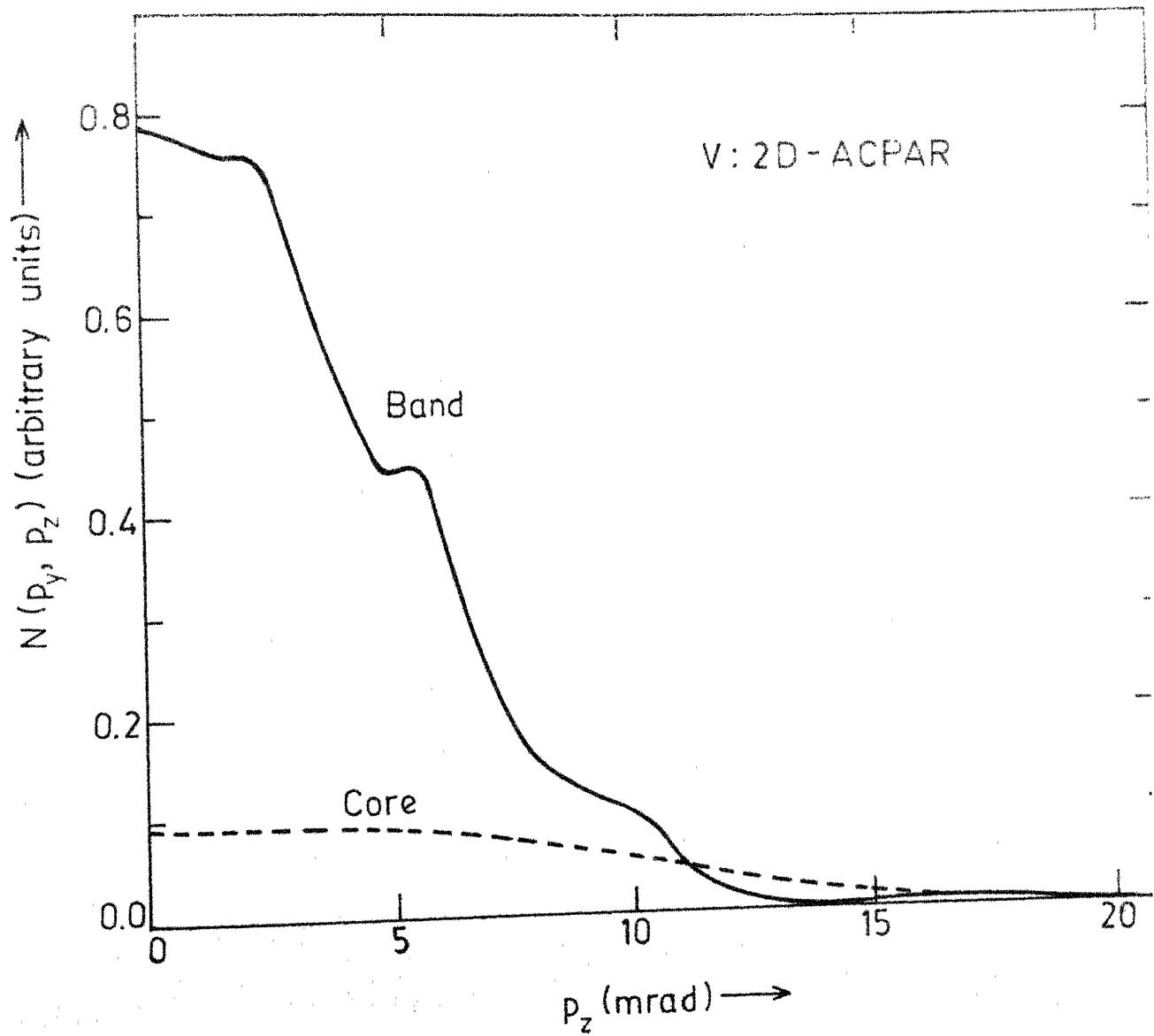
Fig. 4.26: The $N(p_y = 0, p_z)$ curve (dashed line) contributed by core $[(1s)^2 \ (2s)^2 \ (2p)^6 \ (3s)^2 \ (3p)^6]$ electrons in V. For the sake of comparison the contribution to $N(p_y = 0, p_z)$ by the band electrons for the orientation A is also shown(solid curve)

the free-atom orbital wavefunctions for V obtained following
Herman and Skillman [26]. These values of the core TPMD
(assumed isotropic) are given in Table 4.8 and it is about
5 % of the TPMD due to the band electrons at p = 0. The
contribution by the core electrons to the 2D-ACPAR curves is
given in Table 4.9 and is also shown in Fig. 4.26. It is
observed that the core electron contributions are about
12 % of the $N(p_y = 0, p_z)$ curve due to band electrons at
$p_z = 0$ for the orientation A.

It has been shown by Mader et al. [27] that in the
case of Al the calculated core distributions have to be
reduced by a factor of 2 with respect to the conduction
electrons for obtaining a satisfactory agreement between
theory and experiment. Such a core reduction factor has also
been used by Mijnarends and Singru [28] for Cu. The physical
argument in favour of the core reduction factor is that the
core electrons, being tightly bound, show a smaller polari-
zability in the presence of positron. The work of Mijnarends
and Singru [28] has shown that the choice of the core reduc-
tion factor depends on the type of enhancement correction
(discussed below) and goodness-of-fit between experiment
and theory.

The second important correction arises because of
the many-body effects. As pointed out in Sec. 3.5 the
TPMD $\rho_b(\vec{p})$, calculated for the conduction electrons within
the independent particle approximation can be multiplied by

4.8 Calculation of the 2D-ACPAR Curves by Using Modified Wigner-Seitz Model

In the case of Al, Mader et al. [27] have calculated the 2D-ACPAR curves using a simpler modified Wigner-Seitz (MWS) model first suggested by Berko and Plaskett [25]. In this MWS model a free-electron sphere is centered on each reciprocal lattice site $\vec{K}_i$ in the momentum space. The TPMD is then assumed to be constant within such a sphere and this value is taken to be $W(\vec{K}_i)$ such that

$$W(\vec{K}_i) \;=\; \sum_{j=1}^{occ} |A_{\vec{K}_i,j}|^2 \qquad (4.11)$$

where $A_{\vec{K}_i,j}$ depends on reciprocal lattice vector $\vec{K}_i$ and band index j and it is equal to $A_j(\vec{k}=0, \vec{p}=\vec{K}_i)$ because $\vec{p}=\vec{k}+\vec{K}_i$. The weights, $W(\vec{K}_i)$, for each sphere, were calculated from the results of full band structure calculations described earlier in this Chapter. The geometry of the momentum space with the various Wigner-Seitz spheres (radii 5.92 mrad for V) centered at the different $\vec{K}_i$ points for the BCC V are shown in Fig. 4.27. For those $\vec{p}$-values which lie within the common volume of more than one sphere the weights $W(\vec{K}_i)$ have been added. The contribution from the $(3\underline{d})^3$ core electrons was taken into account by calculations similar to those described in Sec. 4.7. The 2D-ACPAR curves, $N(p_y,p_z)$ calculated by the above procedure (MWS model) are shown in Figs. 4.28 and 4.29. These results show that although the MWS model calculation is close to the full band structure
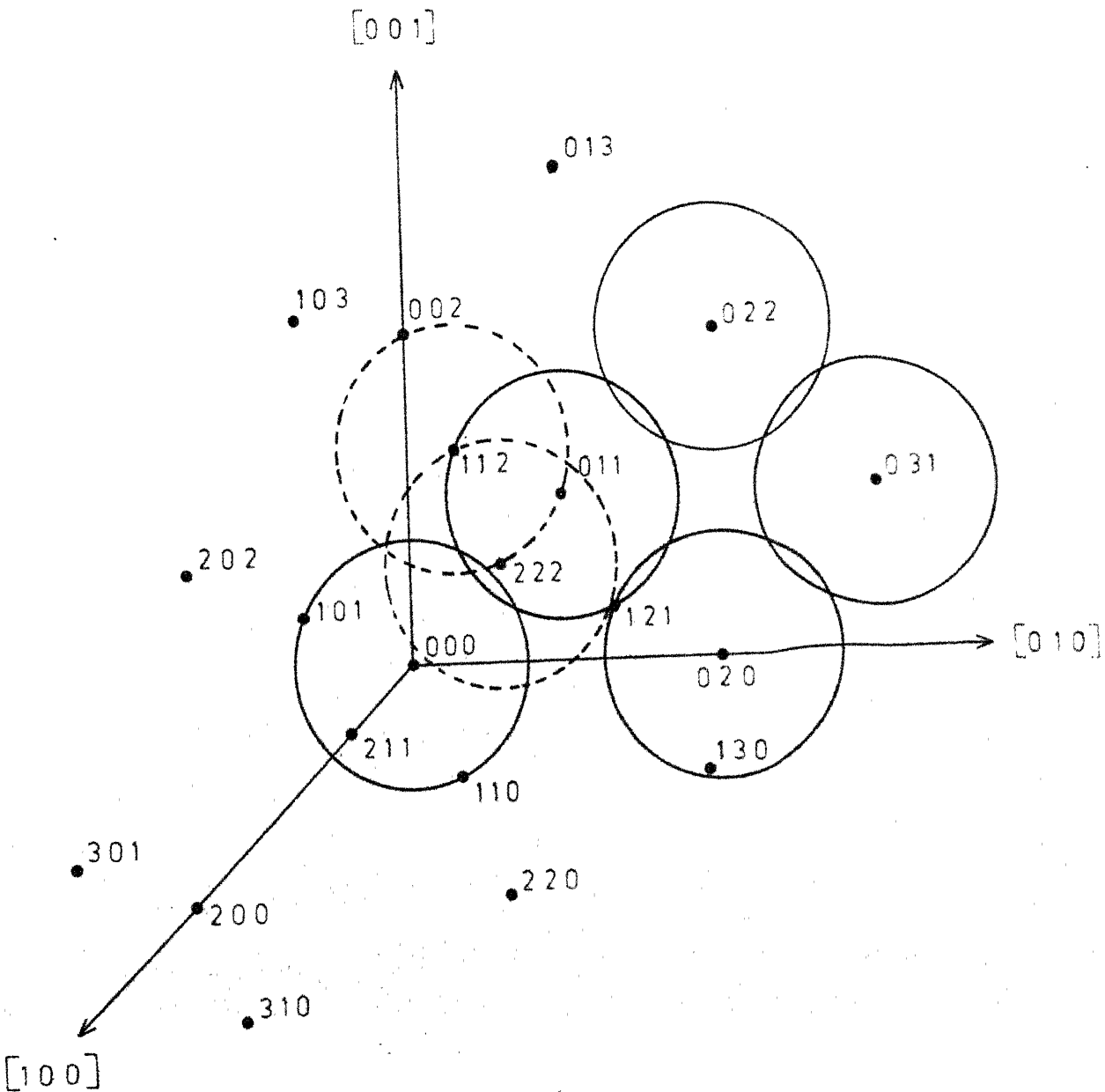
Fig. 4.27: The geometry of the momentum space showing some
points in V (BCC). Some of the Wigner-Seitz
spheres centered at some selected K_i points are
shown by their cross section by (or projection of)
the (100) plane.
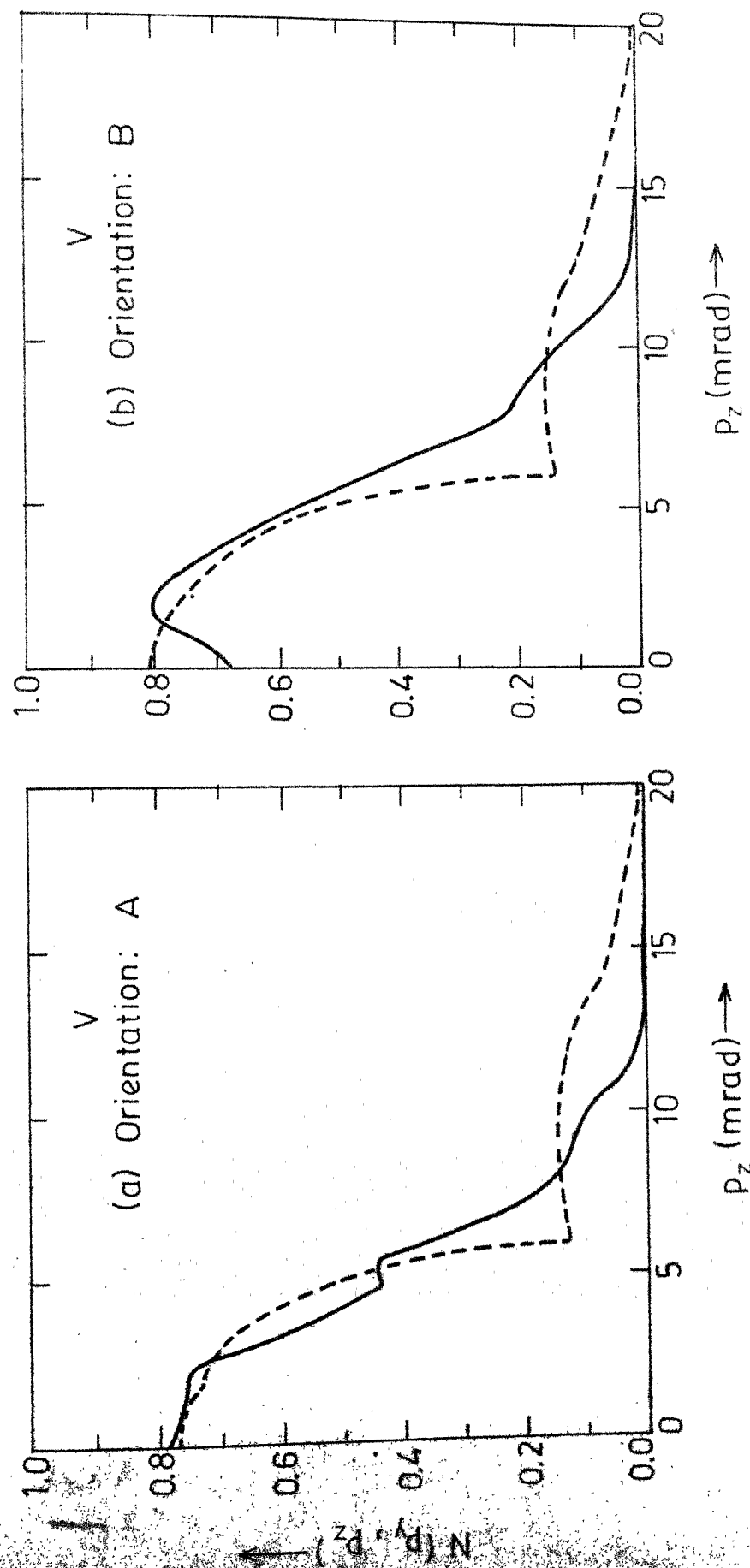
Fig. 4.28: Comparison of the 2D-ACPAR curves calculated by the full band structure calculation (solid line) and HWS model (dashed line). (a) Orientation A and (b) orientation B (Table 4.7).
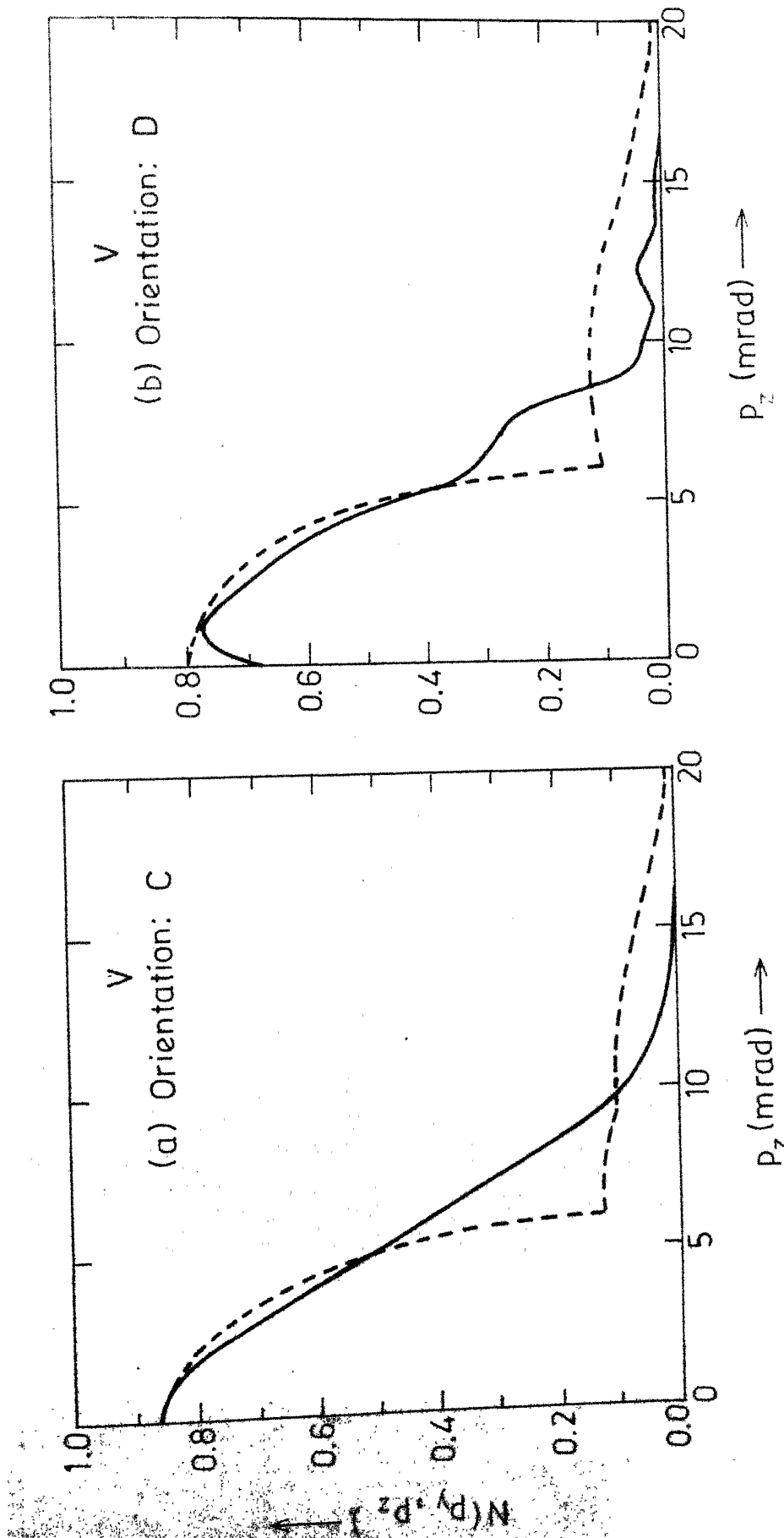
Fig. 4.29: Same as Fig. 4.28. (a) Orientation C and (b) orientation D (Table 4.7).

calculations for Al [27], it differs significantly from the full band structure calculation for V. This behaviour is expected because the FS of V is non-spherical and highly anisotropic. The high momentum components in the MWS curve are higher because of the absence of the hybridization effects which are taken into account by a full band structure calculation in a natural manner. The results of Figs. 4.28 and 4.29 illustrate the inadequacy of the MWS model to predict the fine-structure in the 2D-ACPAR curves and thus emphasize the need to perform full band structure calculation for a transition metal like V.

4.9 Summary

To summarize, the results presented in this Chapter for the TPMD and the 2D-ACPAR curves underline the importance of the effects of band structure and FS topology in the case of V. The discussion of these results point out the limitations of the orientations A, B, C and D for studying certain parts of the FS sheets. The FS cross sections in the $p_y \neq 0$ planes suggest that measurements of $N(p_y \neq 0, p_z)$ curves are necessary to determine different dimensions of the FS. Our results indicate how the possible existence of the necks (connecting the NCE and the JGA) can be confirmed by the 2D-ACPAR measurements. The present theoretical calculation provide a basis for comparing future experimental results with theory. Various corrections required before

our theoretical results can be compared with experiment are also discussed. A comparison of our full band structure calculations with a simpler modified Wigner-Seitz model calculation is made and it shows that full band structure calculations are essential. It is suggested that a comprehensive measurement of the 2D-ACPAR curves for the single crystals of V be undertaken by experimental groups.

REFERENCES

1. P.E. Mijnarends, ''Construction of a Muffin-Tin Potential for Metallic Vanadium'', Report RCN-76-010, Reactor Centrum Nederland, Petten (N.H.) The Netherlands, 1976 (Unpublished).

2. H. Kaga, Phys. Lett. $\underline{37}$A, 373 (1971).

3. J. Hubbard, J. Phys. C$\underline{2}$, 1222 (1969).

4. R.M. Singru (Private Communication).

5. D.A. Papaconstantopoulos, J.R. Anderson and J. W. McCaffrey, Phys. Rev. B$\underline{5}$, 1214 (1972).

6. S. Wakoh and J. Yamashita, J. Phys. Soc. Jpn. $\underline{35}$, 1394 (1973).

7. L.F. Mattheiss, Phys. Rev. $\underline{134}$, A970 (1964).

8. J.R. Anderson, J.W. McCaffrey and D.A. Papaconstantopoulos, Solid State Commun. $\underline{7}$, 1439 (1969).

9. M. Yasui, E. Hayashi and M.J. Shimizu, J. Phys. Soc. Jpn. $\underline{29}$, 1446 (1970).

10. T.M. Hattox, J.B. Conklin, Jr., J.C. Slater and S.B. Trickey, J. Phys. Chem. Solids $\underline{34}$, 1627 (1972).

11. J.F. Alward, C.Y. Fong and C. Guha Sridhar, Phys. Rev. $\underline{18}$, 5438 (1978).

12. D.W. Eastman, Solid State Commun. $\underline{7}$, 1967 (1969).

13. D.W.J. Fisher, J. Appl. Phys. $\underline{40}$, 4151 (1969).

14. L.L. Boyer, D.A. Papaconstantopoulos and B.M. Klein, Phys. Rev. B$\underline{15}$, 3685 (1977).

15. R.D. Parker and M.M. Halloran, Phys. Rev. B$\underline{9}$, 4130 (1974).

16. A.G. Gould, R.N. West and B.G. Hogg, Can. J. Phys. $\underline{50}$, 2294 (1972).

17. D.D. Betts, A.B. Bhatia and M. Wyman, Phys. Rev. $\underline{104}$, 37 (1956).

18. P.E. Mijnarends, Physica $\underline{63}$, 235 (1973).

19. R. Harthoorn and P.E. Mijnarends, J. Phys. F8, 1147 (1978).

20. Krishna Gandhi K.R., Ph.D. Thesis, Indian Institute of Technology Kanpur, India (Unpublished) 1978.

21. S. Wakoh and J. Yamashita, J. Phys. Soc. Jpn. 35, 1406 (1973).

22. N. Shiotani, T. Okada, T. Mizoguchi and H. Sekizawa, J. Phys. Soc. Jpn. 38, 423 (1975).

23. L.F. Mattheiss, Phys. Rev. 139, A1893 (1965).

24. S. Berko in Positron Annihilation Proceedings of the Fifth International Conference on Positron Annihilation, Lake Yamanaka, Japan, 8-11 April 1979, ed. R.R. Hasiguti and K. Fujiwara, The Japan Institute of Metals, Sendai Japan (1979), p. 65.

25. S. Berko and J.S. Plaskett, Phys. Rev. 112, 1877 (1958).

26. F. Herman and S. Skillman, Atomic Structure Calculations, Prentice-Hall, Englewood Cliffs, N.J. (1963).

27. J. Mader, S. Berko, H. Krakauer and A. Bansil, Phys. Rev. Lett. 37, 1232 (1976).

28. P.E. Mijnarends and R.M. Singru, Phys. Rev. B19, 6038 (1979).

29. S. Kahana, Phys. Rev. 129, 1622 (1963); J.P. Carbotte and S. Kahana, Phys. Rev. 139, A213 (1965); J.P. Carbottle, Phys. Rev. 155, 197 (1967).

Chapter 5

RESULTS FOR THE 2D-ACPAR IN VANADIUM DEUTERIDE $VD_{0.72}$

5.1 Introduction

Recently the metal-hydrogen systems have become an
interesting subject for theoretical and experimental research
because of their technological applications as well as
because of the fundamental nature of the problem [1].
Different theoretical and experimental techniques are being
used to determine the electronic structure and other physical
properties of the metal-hydrogen systems. When hydrogen is
dissolved in metals it is found to occupy interstitial sites
in the host lattice with an accompanying expansion in the
volume. The metal-hydrogen system, therefore, shows changes
in the electronic structure of the host metal which can
arise from the influence of the hydrogen as well as from the
structural changes in the metal lattice. Although the
experimental techniques involving the measurement of density
of states or magnetic properties have been in vogue over
the past many years [2], recent introduction of experimental
techniques like Compton scattering [3,4] and positron annihi-
lation [5] (which determine momentum distributions) have
provided new probes to examine different theories.

Historically, there have been two main theoretical
models which have been used to describe the electronic
structure of metal hydrides [2]. The first model, called

''anionic model'' arose out of the similarity in the proper-
ties of alkali hydrides (e.g. LiH and NaH) and the alkali
halides (e.g. LiF, NaCl) both of which are characterised by
the valence state of H^-. The main assumption in the 'anionic'
model is that in a metal hydride hydrogen accepts an electron
from the host metal and the metal behaves like M^+ and
hydrogen like H^-. The behaviour of the transition metal
hydride, on the other hand, suggests that in a metal hydride
(e.g. VH) hydrogen donates its electron to the host metal
(without changing the band structure of the host metal) and
assumes a 'protonic' character. This has given rise to a
'protonic' model and according to it VH system should be
similar to a substitutional alloy V-Cr following a rigid band
approximation. Almost all of the earlier experimental data
were being interpreted in terms of either the 'anionic' or
'protonic' model. The ab initio band structure calculations
of the electronic structure of the metal-hydrogen systems
carried out in the last decade have, however, shown that the
electronic states in a metal hydride are much different from
those predicted by the 'anionic' or 'protonic' model. A
review of these band structure methods is given by
Switendick [2]. The results of the APW calculations in
the transition metal hydrides show that in going from a
metal to metal hydride there is little effect on the
electron states having predominantly d-character while
states having s-like character shift to lower energies,

changing the band structure considerably.

It is known that vanadium can absorb large amount of
hydrogen (or deuterium) which goes to the interstitial sites
of the bcc host lattice. The electronic structure of the
V-H and V-D system has been studied experimentally using
techniques like electronic specific heat [6], magnetic
susceptibility [7], nuclear magnetic resonance [8] etc. and
the results were analysed in terms of the protonic rigid
band model. Measurements by Fukai et al. [9] using soft
X-ray emission spectroscopy indicated that addition of
hydrogen (or deuterium) causes changes in the d bands of
vanadium and formation of bonding states involving H(D)-1s
and V-3d orbitals. These experimental results along with
the theoretical calculations by Switendick [2] have shown
that the electron states having s-like character at the H
(or D) site are modified and the density of states for VH_x
(or VD_x) is different from that predicted by the 'protonic'
model.

Recently the electronic structure of vanadium
hydrides and deuterides has been investigated by employing
Compton scattering [3,4] and positron annihilation techniques
[5]. The idea in these studies is to study the electron
wavefunction through their momentum distributions. Lässer
and Lengeler [3] have measured the Compton profiles of
vanadium and palladium hydrides and have shown that the
'anionic' or 'protonic' model is not successful in explaining

their results. The band structure calculations which incorporate metal-hydrogen bonding states (created below the Fermi level by the introduction of hydrogen in the host lattice) however give a better agreement with the experimental results. Measurement of the directional Compton profiles from the single crystals of V and $VD_{0.68}$ by Itoh et al. [4] have also shown that a fraction of the electrons from deuterium goes in filling up the hole states of V while the remaining electrons form bonding states between V and D.

Recently Hasegawa et al. [5] have carried out long-slit ACPAR measurements on the single crystal of vanadium-deuterium alloys $VD_{0.002}$, $VD_{0.02}$ and $VD_{0.68}$. These authors observed prominent changes in the long-slit ACPAR curves of pure V and $VD_{0.68}$ for the [100], [110] and [111] directions. The characteristic finestructure in the long-slit or 1D-ACPAR curves for the pure single crystal of V (arising out of the complicated FS topology) was found to be absent in $VD_{0.68}$. The changes in the observed long-slit ACPAR curves can be attributed to a gradual filling of the ''hole'' bands of V with the dissolution of deuterium.

The results of VD_x by Compton scattering [3,4] as well as by ACPAR studies [5] establish the fact that the momentum distribution in V is altered by the addition of deuterium. One should therefore expect that a 2D-ACPAR study of VD_x (or VH_x) system should provide us with a greater wealth of information about the band structure, FS topology and

momentum distributions in vanadium deuterides (hydrides).
With this aim in mind we have calculated the 2D-ACPAR curves
in $VD_{0.72}$ and compared these with the results for pure V.
The method followed in our calculation is outlined in the
next section.

5.2 Method of Calculation

The phase diagram of the V-D system is less complica-
ted than that for the V-H system (Figs. 5.1 and 5.2). The
α-phase of the V-H system covers a limited composition range
at room temperature. For VD_x the α-phase reappears at room
temperature for $x > 0.65$. The studies of positron annihila-
tion in the VH_x system by Mantl and Singru [10] have shown that
there is trapping of positrons by lattice defects which
affects the positron parameters across the phase boundaries.
In order to study the 2D-ACPAR curves without the complica-
tions of positron trapping one should study the VD_x system
rather than the VH_x system so that even at room temperature
the α-phase continues as long as $x > 0.65$. We have, therefore,
chosen the system $VD_{0.72}$ for which the 2D-ACPAR curves are
calculated.

Perhaps the best way to calculate the TPMD in
$VD_{0.72}$ would be to make an ab initio calculation employing
an ATA method [11] or the CPA-KKR method [12] to obtain the
electron wavefunctions. The problem of finding the positron
wavefunction becomes more complicated because the affinities
of positron for V and D have to be known. The e^+-impurity
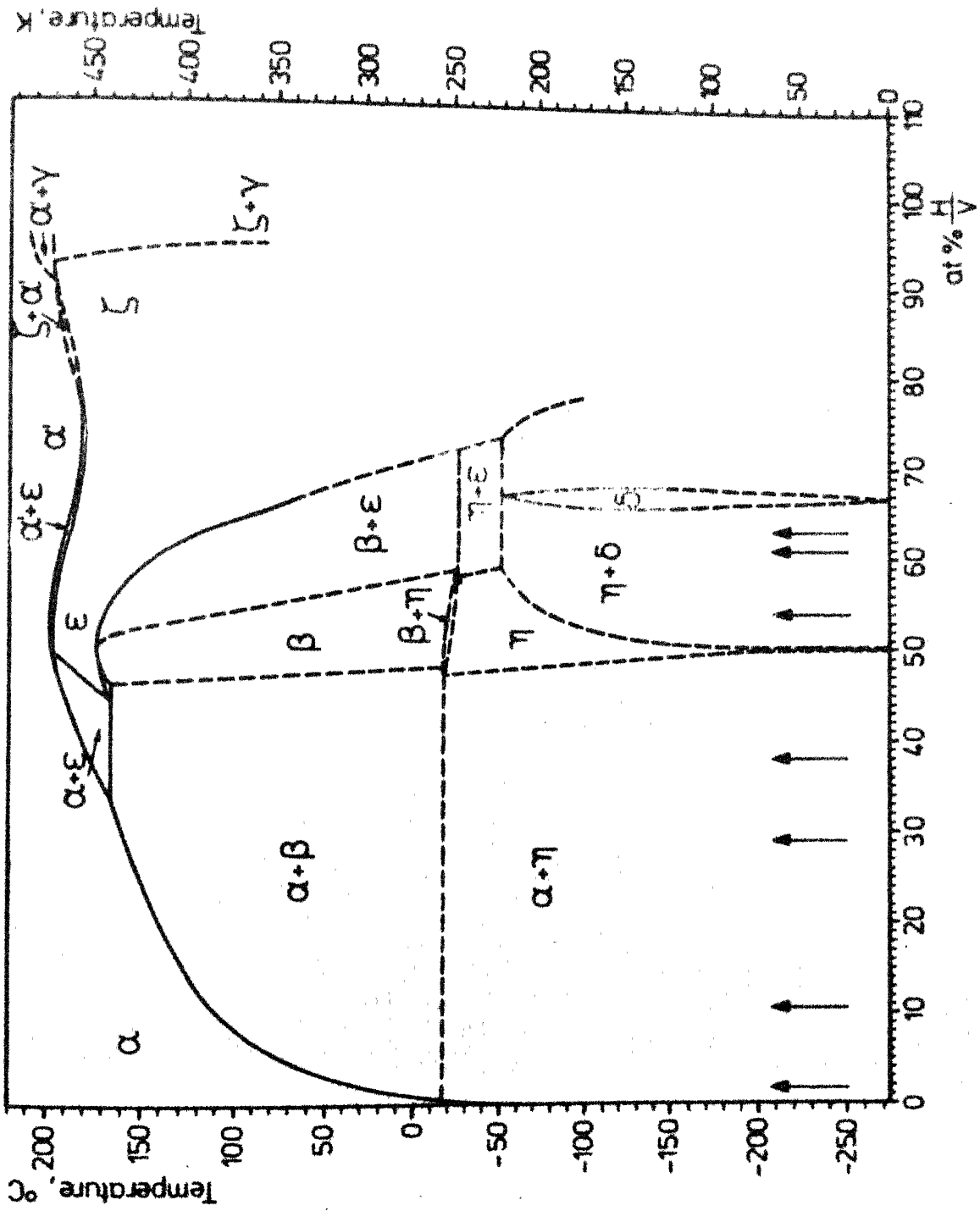
Fig. 5.1: The phase diagram for the V-H system [1].
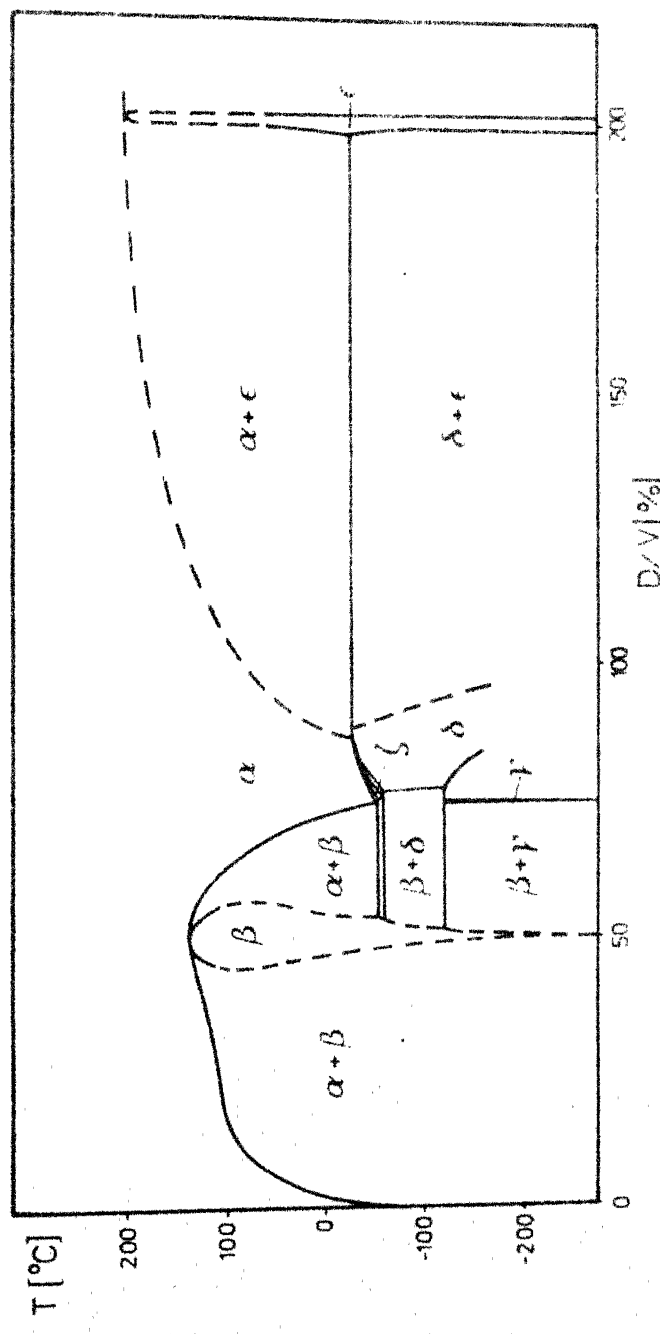
Fig. 5.2: The phase diagram for the V-D system [11].

scattering effects may also be important. Thus the exact determination of the TPMD in $VD_{0.72}$ by such ab initio method would pose serious difficulties. We have therefore avoided this approach and have used an approximate method based on protonic rigid band model outlined below. It is realised that our method is naïve and is open to objections. Nevertheless it provides a first stage of our understanding of the TPMD and 2D-ACPAR curves in the VD_x system. We believe that our present calculations can be useful to design a 2D-ACPAR experiment in the VD_x system.

The method of our calculation is the one used for Cu-Zn alloy earlier [13] and is outlined below. The basic assumption underlying our calculations has been taken from the work of Kanhere and Singru [14] who studied the theoretical electron momentum distribution in a series of 3d transition metals (V, Cr, Fe, Ni and Cu). Their results indicated that the partial contribution to the EMD by the jth band, that is the $\rho_{b,j}(\vec{p})$ curves along a particular $<hk\ell>$ direction do not change much in going from a metal to its next higher neighbour having the same crystal structure (i.e. in going from V to Cr). The total EMD, which is obtained by a sum over the occupied bands

$$\rho_b(\vec{p}) = \sum_{j=1}^{occ} \rho_{b,j}(\vec{p}) \qquad (5.1)$$

however shows major changes due to the change in the Fermi energy (E_F). Using this idea and assuming the 'protonic' model

and a rigid band approximation we proceeded by the following steps for the calculation of the TPMD and the 2D-ACPAR curves in the $VD_{0.72}$ system.

i)   Following the protonic model it was assumed that the deuterium in $VD_{0.72}$ donates all its electrons to the conduction band of vanadium.

ii) Assuming the rigid band model, the Fermi energy (E_F') in $VD_{0.72}$ was calculated from the density of states, $n(E)dE$, and Fermi energy (E_F) in pure V by using the relations

$$5.0 \quad = \int_{-\infty}^{E_F} n(E) \, dE \qquad\qquad (5.2)$$

$$5.72 = \int_{-\infty}^{E_F'} n(E) \, dE \qquad\qquad (5.3)$$

In other words the density of states, $n(E)dE$, was held rigid in going from V to $VD_{0.72}$. The value of E_F' determined by us was 0.800 Ry.

iii) Following Kanhere and Singru [14] the partial TPMD $\rho_{b,j}(\vec{p})$ was considered rigid in going from V to $VD_{0.72}$. The total TPMD $\rho_b(\vec{p})$ for $VD_{0.72}$ was determined at the 1200 $\vec{p}$-points by summing eq. (5.3) upto the new $E_F' = 0.800$ Ry.   The 2D-ACPAR curves were next calculated for the four orientations (Table 4.7) as before (Chapter 4).

iv)   In our method of calculation there is no difference
between a hydride and deuteride and our results could
be equally applicable to $VH_{0.72}$. We have quoted our
results as for $VD_{0.72}$ because experimentally $VD_{0.72}$
is more suited for measurements.

5.3   Results and Discussions

The results of our calculations for $VD_{0.72}$ are shown
in Fig. 5.3 and 5.4. The theoretical 2D-ACPAR curves for
$VD_{0.72}$ are compared with those for pure V through the
difference curves

$$\Delta N = N_{VD_{0.72}} (p_y, p_z) - N_V (p_y, p_z) \qquad (5.4)$$

in Fig. 5.5 where the vertical bars indicate the magnitude
of 0.1 N_V ($p_y = 0$, $p_z = 0$). It was pointed out earlier in
Sec. 5.1 that the Compton scattering [3,4] as   well as the
long-slit ACPAR data [5] from single crystal specimens of
VD_x have shown that the curves from VD_x are less anisotropic
as compared to those from pure V. These authors found that
the behaviour of VD_x was closer to Cr than to V thus sugges-
ting that the electrons of deuterium fill the hole states
of V. The FS topology of the $VD_{0.72}$ calculated in the
framework of the rigid band approximation and the 'protonic'
model is shown in Fig. 5.6 and it shows how the hole surfaces
of V are shrunk by the donation of electrons from deuterium.
It is seen from Fig. 5.6 that the second band is now fully

$VD_{0.72}$

(b) Orientation: B

p_z (mrad) $\longrightarrow$

1.0   0.8   0.6   0.4   0.2   0.0

$VD_{0.72}$

(a) Orientation: A

p_z (mrad) $\longrightarrow$

1.0   0.8   0.6   0.4   0.2   0.0
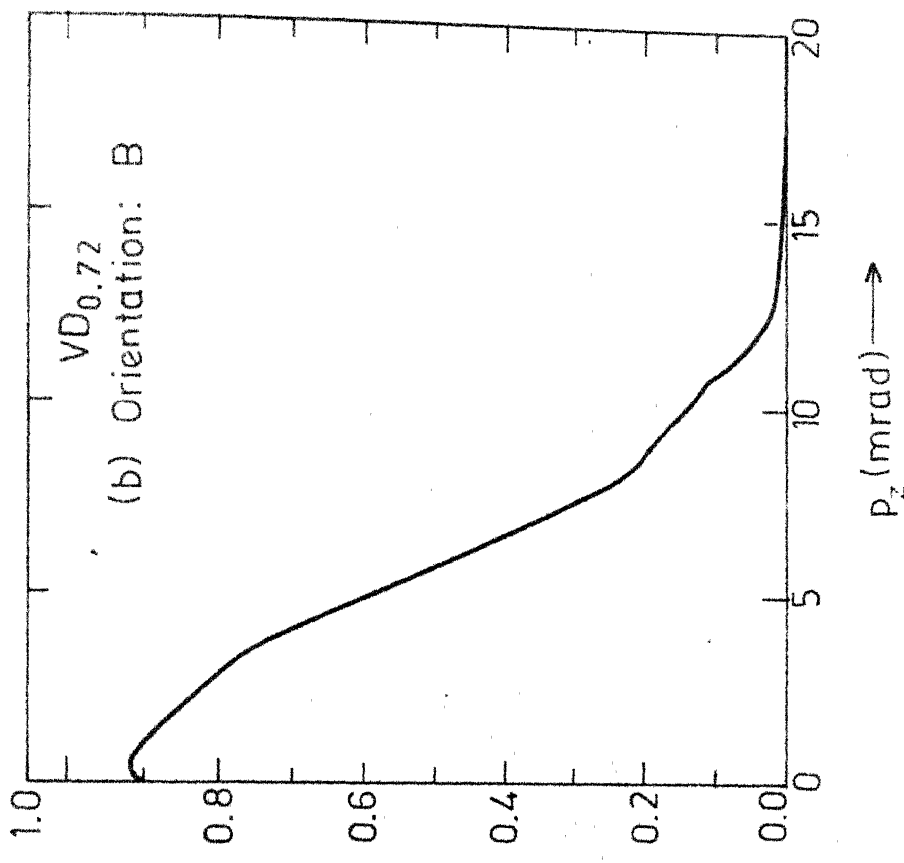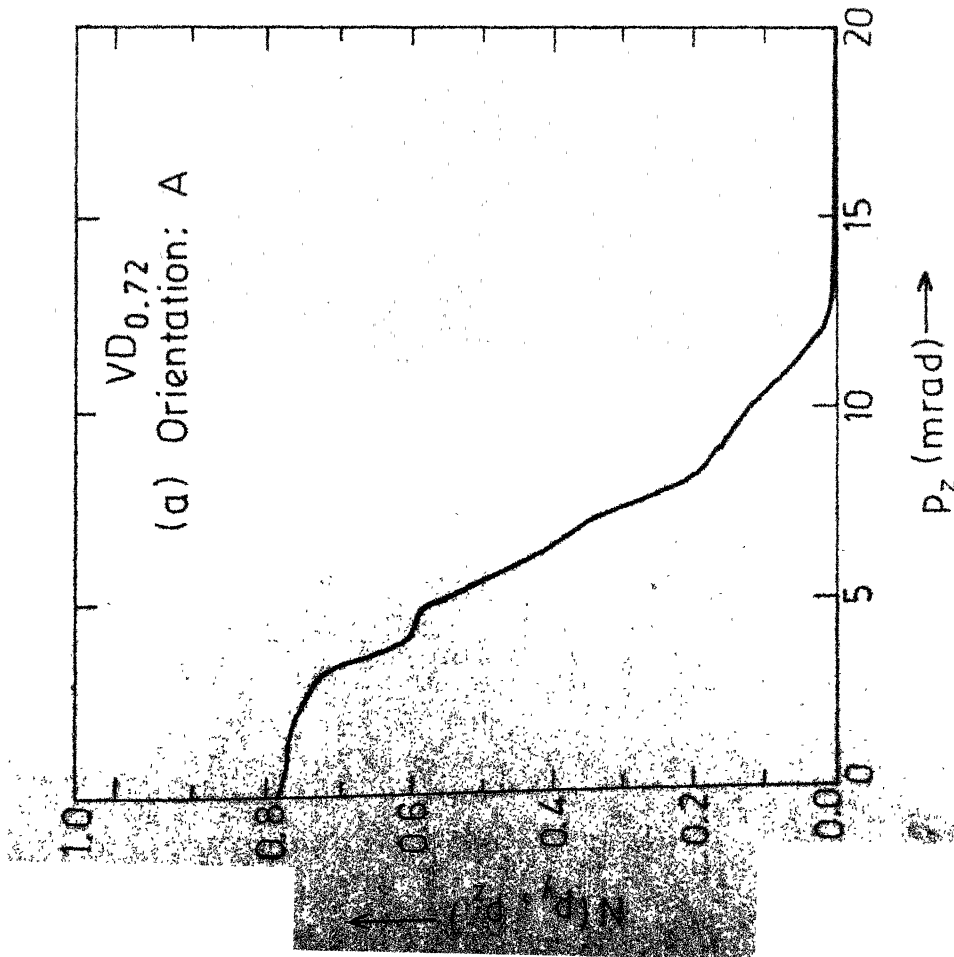
Fig. 5.3: 2D-ACPAR curves, $N(p_y = 0, p_z)$ for $VD_{0.72}$ for orientations
(a) A : $\{p_z, p_{xy} = \{[001], [130]\}$ and (b) B : $\{p_z, p_x = \{[001], [110]\}$.
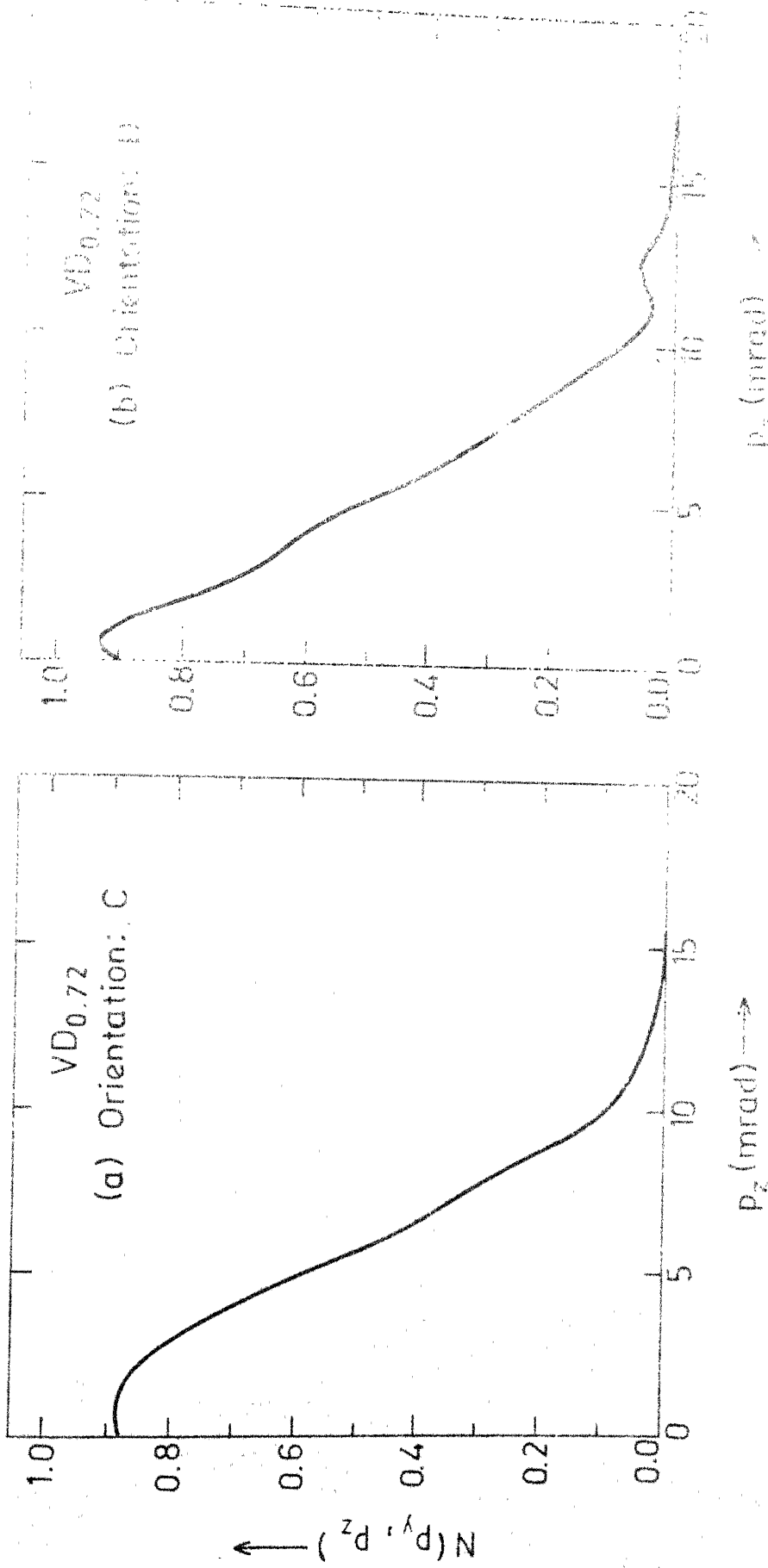
Fig. 5.4: The range of force as a function of p_z and p_y.
(a) Orientation C; (b) Orientation ...
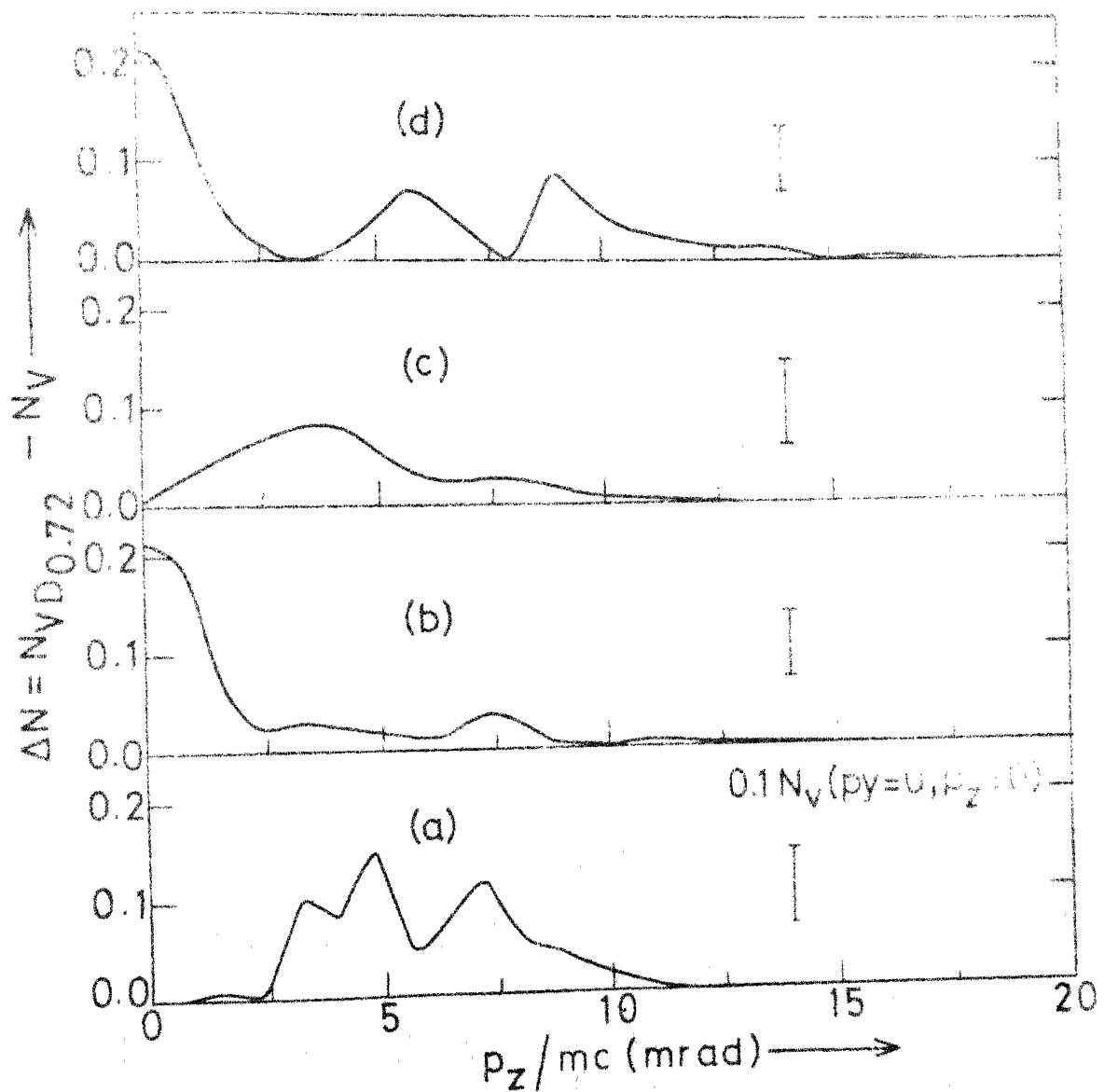
Fig. 5.5: The difference curves ΔN (eq. 5.4) between the 2D-ACPAR curves for $VD_{0.72}$ and V for the orientations (a) A, (b) B, (c) C and (d) D. The scale of ΔN is same as that for $N(p_y=0, p_z)$ in Figs. 4.16-4.19.

occupied, while third and fourth bands are partially occupied. This filling out of the second and third band must cause changes in the TPMD contributed by the second and third bands with resulting changes in the 2D-ACPAR curves.

Although the general nature of the $N(p_y = 0, p_z)$ curve for the orientation A for $VD_{0.72}$ is similar to that for pure V, the difference curve, ΔN, shows significant structure in the momentum range $p_z \sim 2.5-10.0$ mrad. This structure can be understood with the help of Fig. 5.6. For the orientation B, the concavity in the low momentum region of the $N(p_y = 0, p_z)$ found for pure V is absent in $VD_{0.72}$. Although the $(+)/(-)$ symmetry of the bands is not shown in Fig. 5.6, the considerations of the FS topology suggest that the concavity should disappear in $VD_{0.72}$ because the N-centered ellipsoids (NCE) have shrunk in size. This point was discussed in Sec. 4.6. Similar considerations when applied to the orientation D explain the disappearance of the concavity in $VD_{0.72}$. In any case the difference curves ΔN (Fig. 5.5) show significant structure which should be measurable.

In order to examine the possible nature of the 2D-ACPAR curves in the $p_y \neq 0$ planes of $VD_{0.72}$ we have calculated the FS topology in $(p_x\ p_z)$ planes parallel to the (010) and ($\bar{1}$10) planes. These results for $VD_{0.72}$, shown in Figs. 5.7 - 5.9, can be compared with similar results for pure V shown in Figs. 4.23 - 4.25. Comparison of these two sets of figures reveal that the behaviour of the ΔN
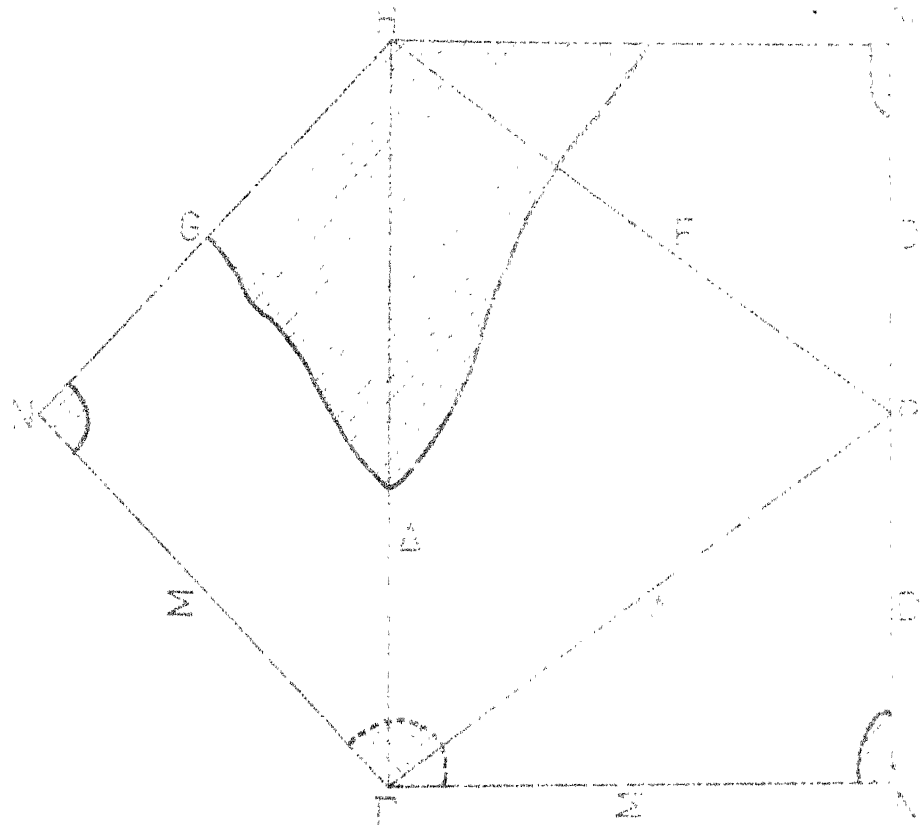
Fig. 5.6: The cross section of the Fermi surface in
VₓCₒ₇₂ by the (100) and (111) planes. The
hatched area (///) denotes the third zone
unoccupied and (•••) denotes the fourth zone
occupied 4d sheet.
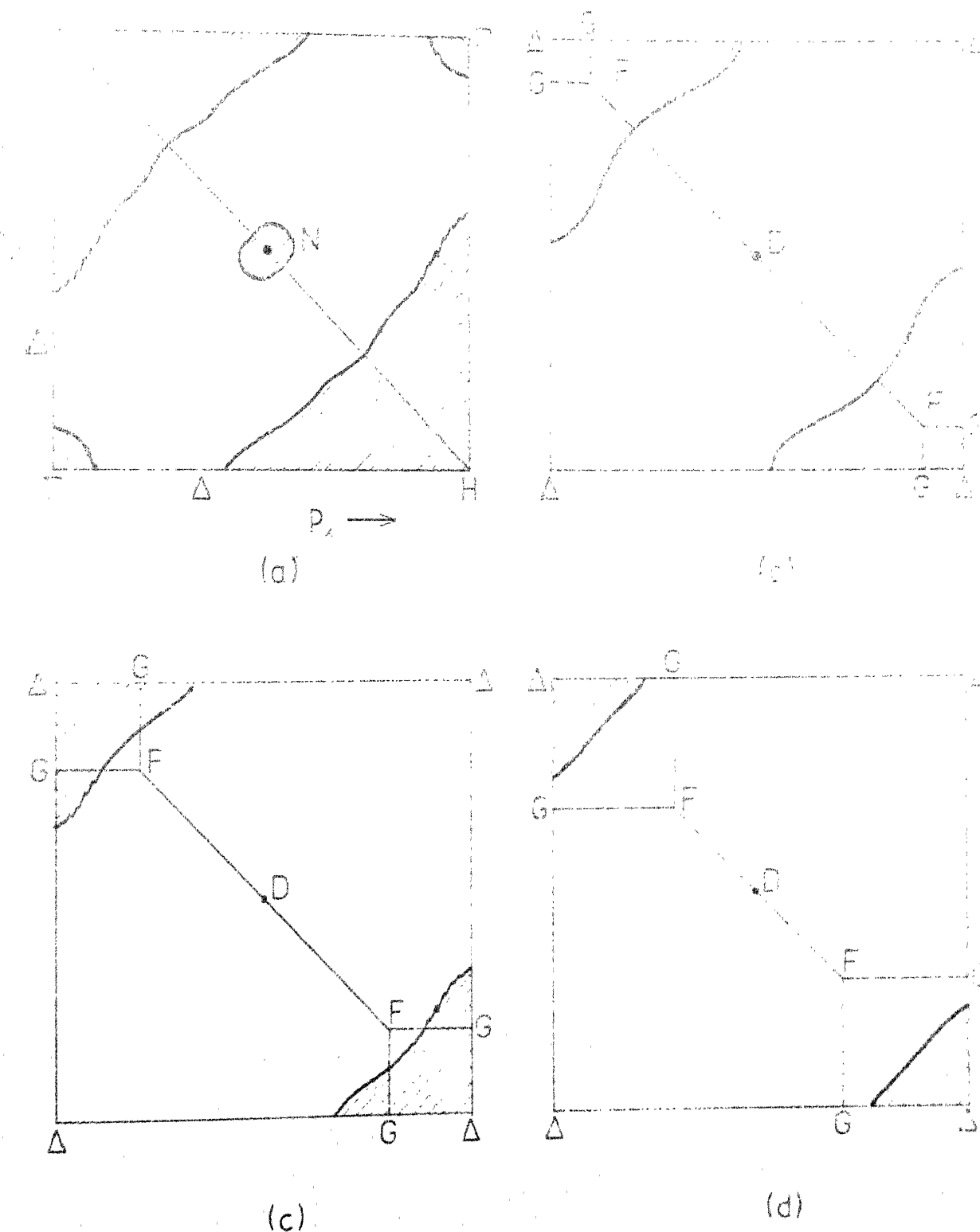
Fig. 5.7: Cross sections of the Fermi surface of $VO_{0.75}$ in different (p_x, p_z) - (010) planes. (a) $p_y = 0$, (b) $p_y = 0.1 \Gamma H$ ($\Gamma H = 7.96$ nrad), (c) $p_y = 0.2 \Gamma H$ and (d) $p_y = 0.3 \Gamma H$. The hatched area ▨ denotes the third band unoccupied and ▨ denotes forth band occupied Fermi surface sheet.
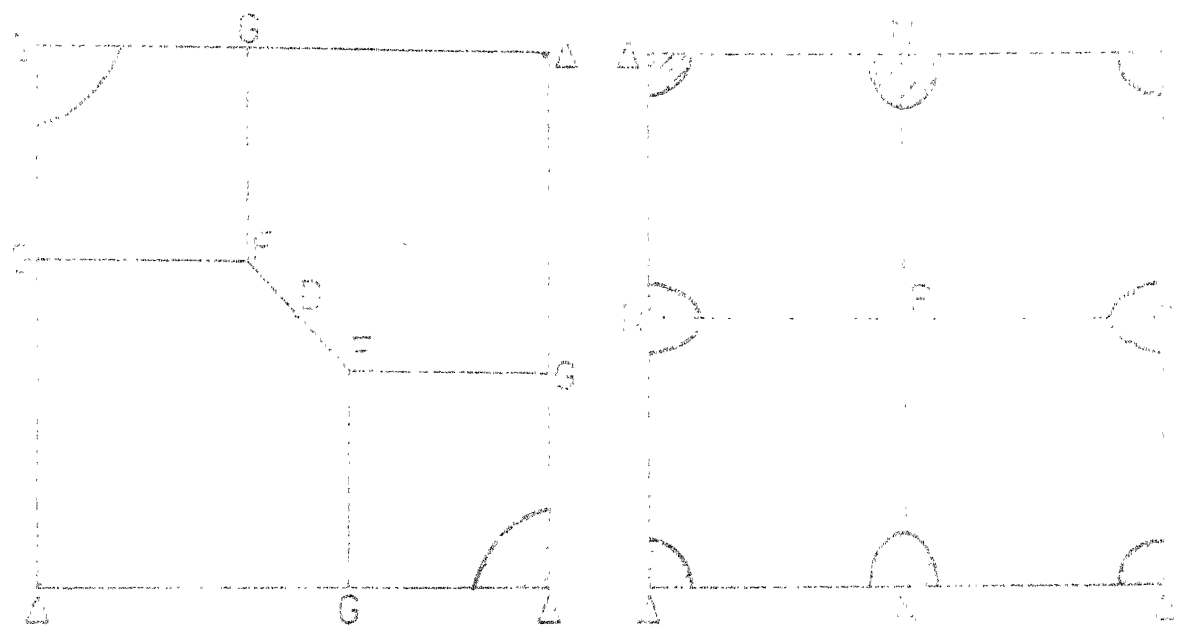
(a)

(b)
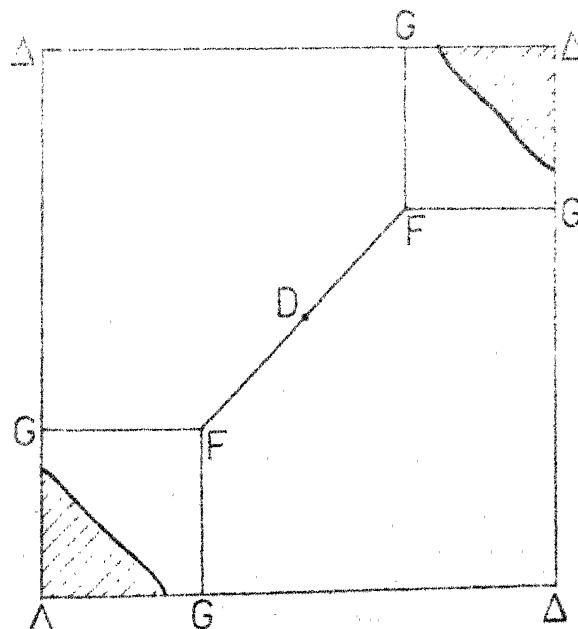
(c)
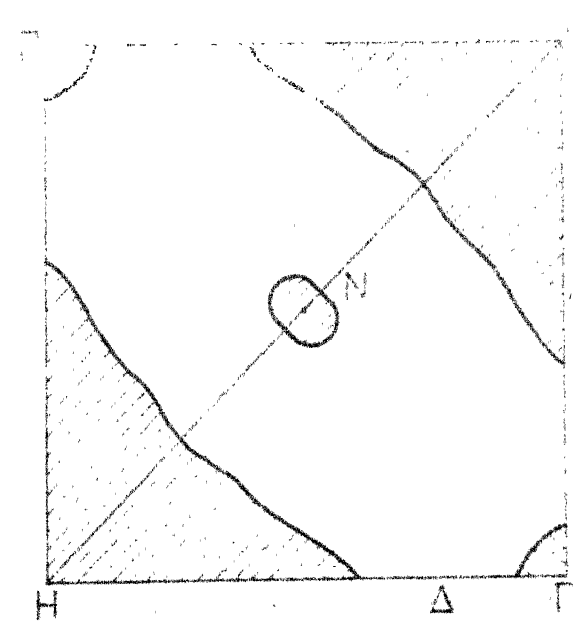
(d)

Fig. 5.8: Same as Fig. 5.7 but for the higher (010) planes. (a) Plane $p_y = 0.4\,\Gamma H$, (b) $p_y = 0.5\,\Gamma H$, (c) $p_y = 0.7\,\Gamma H$ and (d) $p_y = 1.0\,\Gamma H$.
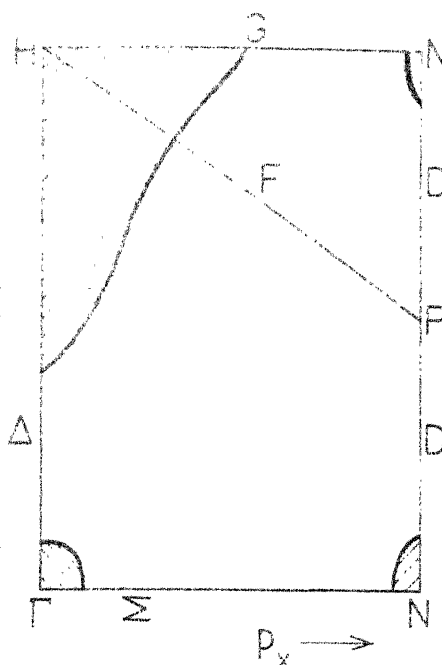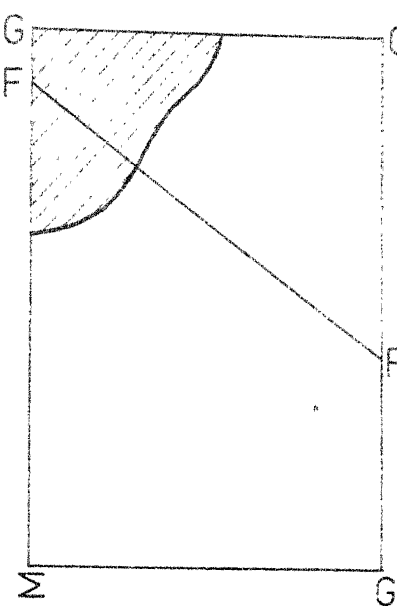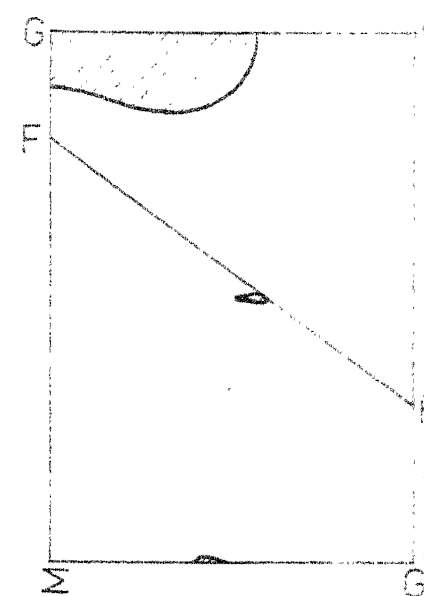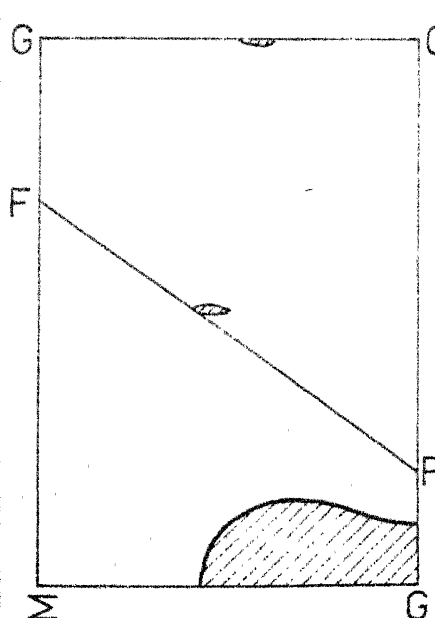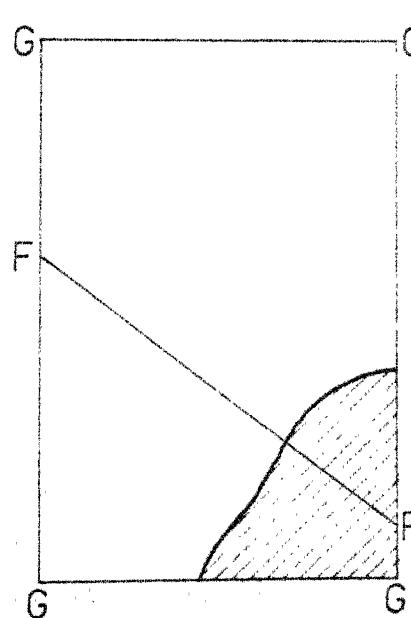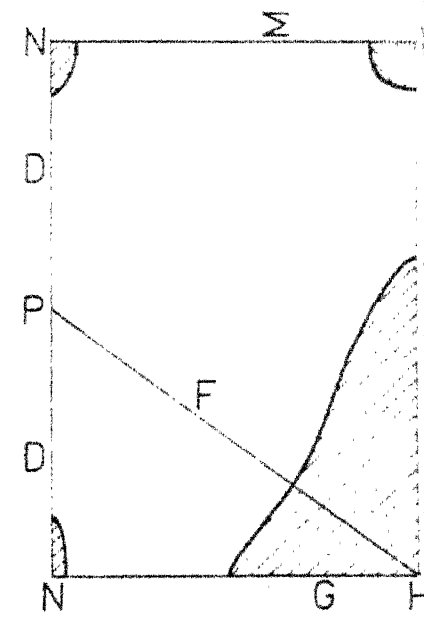
Fig. 5.9: Cross section of the Fermi surface of $VD_{0.72}$ in different $(p_x\ p_z) = (\bar{1}10)$ planes. (a) Plane $p_y = 0$, (b) $p_y = \sqrt{2}\ \Gamma H/10$, (c) $p_y = 2\sqrt{2}\ \Gamma H/10$, (d) $p_y = 3\sqrt{2}\ \Gamma H/10$, (e) $p_y = 4\sqrt{2}\ \Gamma H/10$ and (f) $p_y = 5\sqrt{2}\ \Gamma H/10$. The notation for the hatched areas is same as in Fig. 5.7.

curves (eq. 5.4) can show more drastic changes in going from V to $VD_{0.72}$ when the 2D-ACPAR measurements are made in the $p_y \neq 0$ plane. It is now known from the ab initio calculation of the band structure of transition metal hydrides [2] that the rigid band approximation and protonic model are too simplistic in their approach. However until such ab initio calculations of the TPMD are made, the present results of our simple calculation can provide a first step of understanding the dependence of the 2D-ACPAR curves in $VD_{0.72}$ on the band structure and FS effects. Recently calculations of the momentum distribution of electrons in concentrated random alloys $Cu_{1-x} Ni_x$ [15] and $Ag_{0.2} Pd_{0.8}$ [16] have been reported. However these calculations refer to the case of Compton scattering because they do not take the positron effects into account. These effects would consist of the positron wavefunction (which is not constant), positron affinity for the atoms A and B (which may be different), the enhancement and core reduction corrections. Taking all these effects into account for calculating a realistic 2D-ACPAR curve in VD_x will take more effort. Till such time that such calculations are made, the results of the present work may be used to analyse experimental results.

5.4 Summary

The results presented in this Chapter have shown that the 2D-ACPAR curves show measurable changes in going

from pure V to VD_x. These changes are closely related to the

changes occuring in the band structure and FS of V after

introduction of deuterium (hydrogen). It is suggested that

measurements of 2D-ACPAR curves in V and VD_x (ensuring a

proper choice of the phase as discussed in Sec. 5.2) be

undertaken to examine the changes ΔN (eq. 5.4) in these

curves. In spite of the simplistic assumptions made in our

calculations for $VD_{0.72}$ our results can be useful to interpret

these experimental data when they become available.

REFERENCES

1. G. Alefeld and J. Völkl, ed. Hydrogen in Metal I and II, Springer-Verlag, Berlin-Heidelberg, 1978.

2. A.C. Switendick in Hydrogen in Metal I, ed. G. Alefeld and J. Völkl, Springer-Verlag, Berlin-Heidelberg, 1978, p. 101; A.C. Switendick in Hydrogen Energy, Part B, ed. T.N. Vezivoglu , Plenum Press, New York, 1975, p. 1029.

3. R. Lässer and B. Lengeler, Phys. Rev. B18, 637 (1978).

4. F. Itoh, T. Honda, H. Asano, M. Hirabayashi and K. Suzuki, J. Phys. Soc. Jpn. 49, 202 (1980).

5. M. Hasegawa, S. Koike, M. Hirabayashi, H. Asano and To. Suzuki, J. Phys. Soc. Jpn. 46, 481 (1979).

6. D. Rohy and R.M. Cotts, Phys. Rev. B1, 2484 (1970).

7. S. Aronson, J.J. Reilly and R.H. Wiswall, Jr., J. Less-Common. Met. 21, 439 (1970).

8. S. Kazama and Y. Fukai, Phys. Lett. 51A, 373 (1975); J. Phys. Soc. Jpn. 42, 119 (1977).

9. Y. Fukai, S. Kazama, K. Tanaka and M. Matsumoto, Solid St. Commun. 19, 507 (1976).

10. S. Mantl and R.M. Singru, Phys. Rev. B19, 1391 (1979).

11. P.E. Mijnarends and A. Bansil, Phys. Rev. B13, 2381 (1976); Phys. Rev. B19, 2912 (1979).

12. B.L. Gyorffy and G.M. Stocks in Electrons in Disordered Metals and at Metallic Surfaces. eds. P. Phariseau, B.L. Gyorffy and L. Scheire, Plenum Press, New York (1979), p. 89.

13. P.E. Mijnarends and R.M. Singru, Phys. Rev. B19, 6038 (1979).

14. D.G. Kanhere and R.M. Singru, J. Phys. F7, 2603 (1977).

15. P.E. Mijnarends and A. Bansil in Positron Annihilation Proceedings of the Fifth International Conference on Positron Annihilation, Lake Yamanaka, 8-11 April, 1979 eds. R.R. Hasiguti and K. Fujiwara, The Japan Institute of Metals, Sendai (1979), p. 657.

16. B.L. Gyorffy and G.M. Stocks, J. Phys. F10, L231 (1980).

VITAE

Ashok Kumar Singh was born in Babhanpura Village in Varanasi District, Uttar Pradesh, India on 1st September 1953. He obtained his B.Sc. and M.Sc. degree in Physics from the University of Allahabad, Allahabad. He joined the Ph.D. program in Physics at the Indian Institute of Technology, Kanpur in December 1976. He was a recipient of the National Scholarship from the Government of India from 1970 to 1974 and a bursary from the University of Allahabad from 1974 to 1976. At present he is a Research Scholar at I.I.T. Kanpur. Ashok Kumar Singh is a citizen of India.

PHY-1981-D-SIN-BAN